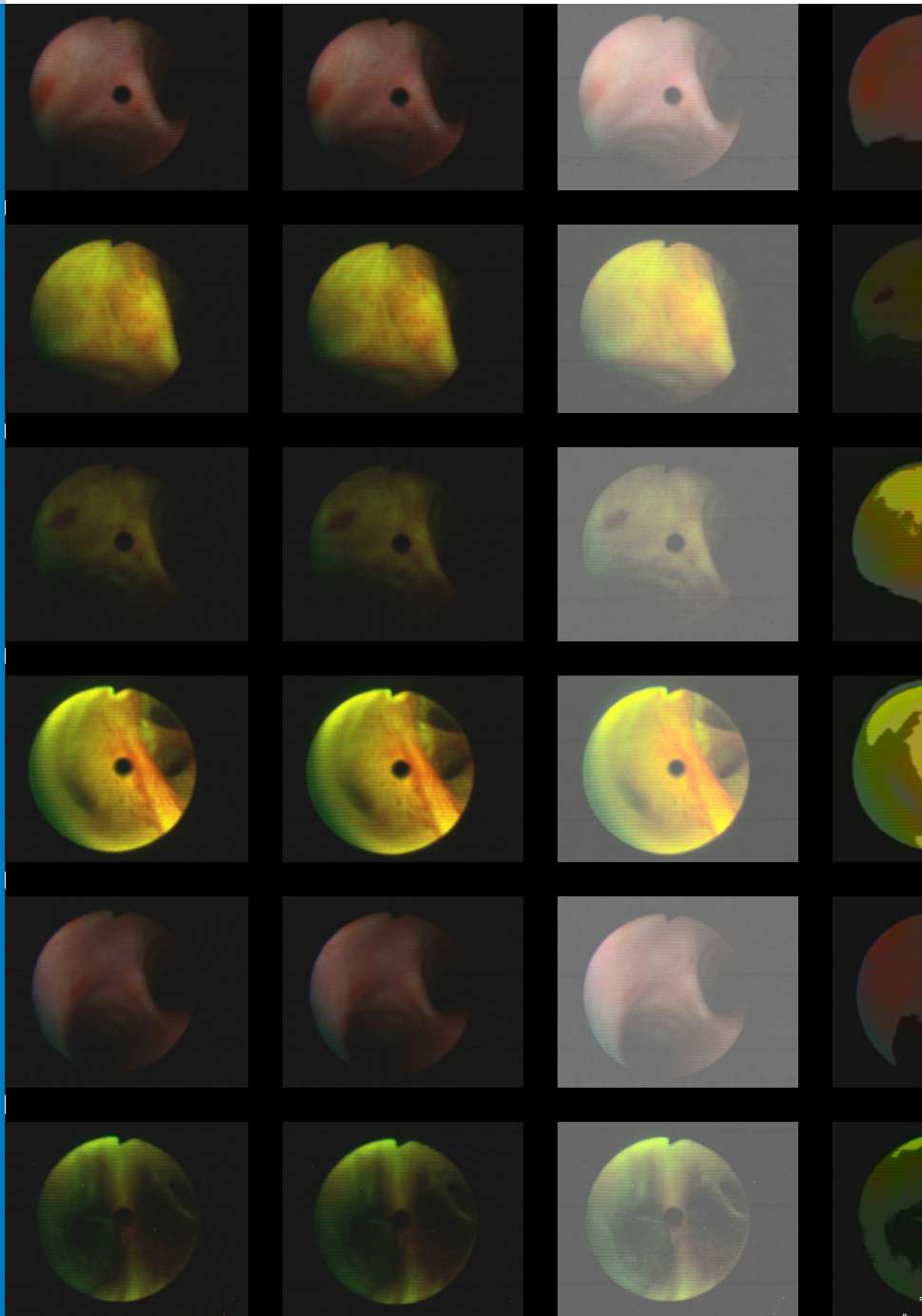




Strojniški vestnik

Journal of Mechanical Engineering

no. **12**
year **2017**
volume **63**



Strojniški vestnik – Journal of Mechanical Engineering (SV-JME)

Aim and Scope

The international journal publishes original and (mini)review articles covering the concepts of materials science, mechanics, kinematics, thermodynamics, energy and environment, mechatronics and robotics, fluid mechanics, tribology, cybernetics, industrial engineering and structural analysis.

The journal follows new trends and progress proven practice in the mechanical engineering and also in the closely related sciences as are electrical, civil and process engineering, medicine, microbiology, ecology, agriculture, transport systems, aviation, and others, thus creating a unique forum for interdisciplinary or multidisciplinary dialogue.

The international conferences selected papers are welcome for publishing as a special issue of SV-JME with invited co-editor(s).

Editor in Chief

Vincenc Butala

University of Ljubljana, Faculty of Mechanical Engineering, Slovenia

Technical Editor

Pika Škraba

University of Ljubljana, Faculty of Mechanical Engineering, Slovenia

Founding Editor

Bojan Kraut

University of Ljubljana, Faculty of Mechanical Engineering, Slovenia

Editorial Office

University of Ljubljana, Faculty of Mechanical Engineering
SV-JME, Aškerčeva 6, SI-1000 Ljubljana, Slovenia

Phone: 386 (0)1 4771 137

Fax: 386 (0)1 2518 567

info@sv-jme.eu, <http://www.sv-jme.eu>

Print: Papirografika Bori, printed in 300 copies

Founders and Publishers

University of Ljubljana, Faculty of Mechanical Engineering,
Slovenia

University of Maribor, Faculty of Mechanical Engineering,
Slovenia

Association of Mechanical Engineers of Slovenia
Chamber of Commerce and Industry of Slovenia,
Metal Processing Industry Association

President of Publishing Council

Branko Širok

University of Ljubljana, Faculty of Mechanical Engineering, Slovenia

Vice-President of Publishing Council

Jože Balič

University of Maribor, Faculty of Mechanical Engineering, Slovenia

International Editorial Board

Kamil Arslan, Karabuk University, Turkey

Hafiz Muhammad Ali, University of Engineering and Technology, Pakistan

Josep M. Bergada, Polytechnical University of Catalonia, Spain

Anton Bergant, Litostroj Power, Slovenia

Miha Boltežar, UL, Faculty of Mechanical Engineering, Slovenia

Franci Čuš, UM, Faculty of Mechanical Engineering, Slovenia

Anselmo Eduardo Diniz, State University of Campinas, Brazil

Igor Emri, UL, Faculty of Mechanical Engineering, Slovenia

Imre Felde, Obuda University, Faculty of Informatics, Hungary

Janez Grum, UL, Faculty of Mechanical Engineering, Slovenia

Imre Horvath, Delft University of Technology, The Netherlands

Aleš Hribernik, UM, Faculty of Mechanical Engineering, Slovenia

Soichi Ibaraki, Kyoto University, Department of Micro Eng., Japan

Julius Kaplunov, Brunel University, West London, UK

Iyas Khader, Fraunhofer Institute for Mechanics of Materials, Germany

Jernej Klemenc, UL, Faculty of Mechanical Engineering, Slovenia

Milan Kljajin, J.J. Strossmayer University of Osijek, Croatia

Peter Krajnik, Chalmers University of Technology, Sweden

Janez Kušar, UL, Faculty of Mechanical Engineering, Slovenia

Gorazd Lojen, UM, Faculty of Mechanical Engineering, Slovenia

Thomas Lübben, University of Bremen, Germany

Janez Možina, UL, Faculty of Mechanical Engineering, Slovenia

George K. Nikas, KADMOS Engineering, UK

José L. Ocaña, Technical University of Madrid, Spain

Miroslav Plančak, University of Novi Sad, Serbia

Vladimir Popović, University of Belgrade, Faculty of Mech. Eng., Serbia

Franci Pušavec, UL, Faculty of Mechanical Engineering, Slovenia

Bernd Sauer, University of Kaiserslautern, Germany

Rudolph J. Scavuzzo, University of Akron, USA

Arkady Voloshin, Lehigh University, Bethlehem, USA

General information

Strojniški vestnik – Journal of Mechanical Engineering is published in 11 issues per year (July and August is a double issue).

Institutional prices include print & online access: institutional subscription price and foreign subscription €100,00 (the price of a single issue is €10,00); general public subscription and student subscription €50,00 (the price of a single issue is €5,00). Prices are exclusive of tax. Delivery is included in the price. The recipient is responsible for paying any import duties or taxes. Legal title passes to the customer on dispatch by our distributor.

Single issues from current and recent volumes are available at the current single-issue price. To order the journal, please complete the form on our website. For submissions, subscriptions and all other information please visit: <http://en.sv-jme.eu/>.

You can advertise on the inner and outer side of the back cover of the journal. The authors of the published papers are invited to send photos or pictures with short explanation for cover content.

We would like to thank the reviewers who have taken part in the peer-review process.

The journal is subsidized by Slovenian Research Agency.



Cover: Bronchial tubes tissue images, obtained during bronchoscopy. Images were captured using two imaging modes. The first mode is using white light spectrum and the second mode is using blue light and observing autofluorescence tissue response. Due to different fluoroscopic properties of malignant and nonmalignant tissue, the autofluorescence method is used to discriminate malignant and nonmalignant tissue.

Image Courtesy:
University Medical Centre, Clinical Department of Pulmonary Diseases and Allergy, Slovenia

ISSN 0039-2480

© 2017 Strojniški vestnik - Journal of Mechanical Engineering. All rights reserved. SV-JME is indexed / abstracted in: SCI-Expanded, Compendex, Inspec, ProQuest-CSA, SCOPUS, TEMA. The list of the remaining bases, in which SV-JME is indexed, is available on the website.

Strojniški vestnik - Journal of Mechanical Engineering is available on <http://www.sv-jme.eu>, where you access also to papers' supplements, such as simulations, etc.

Contents

Strojniški vestnik - Journal of Mechanical Engineering
volume 63, (2017), number 12
Ljubljana, December 2017
ISSN 0039-2480

Published monthly

Papers

Tomaž Finkšt, Jurij Franc Tasič, Marjeta Zorman Terčelj, Marko Meža: A Classification of Malignancy in Suspicious Lesions Using Autofluorescence Bronchoscopy	685
Vytautas Ostaševičius, Vytautas Jūrėnas, Andrius Vilkauskas, Gytautas Balevičius, Andrius Senkus, Eglė Jotautienė: A Novel Excitation Approach to Ultrasonically-Assisted Cylindrical Grinding	696
Damian Janicki: Fabrication of High Chromium White Iron Surface Layers on Ductile Cast Iron Substrate by Laser Surface Alloying	705
Jiangping Mei, Jiawei Zang, Yabin Ding, Shenglong Xie, Xu Zhang: Rapid and Automatic Zero-Offset Calibration of a 2-DOF Parallel Robot Based on a New Measuring Mechanism	715
Marko Švaco, Bojan Šekoranja, Filip Šuligoj, Josip Vidaković, Bojan Jerbić, Darko Chudy: A Novel Robotic Neuronavigation System: RONNA G3	725
Ningning Wang, Xueyi Li, Kun Wang, Qingliang Zeng, Xiao Shen: A Novel Axial Modification and Simulation Analysis of Involute Spur Gear	736
Metod Čuk, Franc Kosel, Nenad Zrnić, Boris Jerman: Analysis of Continuous Sandwich Panels with Profiled Faces	746

Classification of Malignancy in Suspicious Lesions Using Autofluorescence Bronchoscopy

Tomaž Finkšt¹ – Jurij Franc Tasič² – Marjeta Zorman Terčelj³ – Marko Meža^{2,*}

¹ University of Ljubljana, Faculty of Mechanical Engineering, Slovenia

² University of Ljubljana, Faculty of Electrical Engineering, Slovenia

³ University Medical Centre, Clinical Department of Pulmonary Diseases and Allergy, Slovenia

This paper presents a novel approach to the classification of bronchial tissue as either malignant or precancerous based on autofluorescence bronchoscopy (AFB) images. The study consisted of 44 images, of which 22 were confirmed as malignant and 22 as nonmalignant precancerous cases. Our approach starts with the detection of a region of interest (ROI). This is followed by an analysis of semi-normal intensity distributions in gray-scale images of red and green components of the previously identified ROI. Based on the results of this analysis, features are computed, which are then used to build an image-classification model. This model classifies the tissue images into malignant/nonmalignant classes. We utilized several classification algorithms, i.e., naive Bayes, K-nearest-neighbor (K-NN), and support vector machine (SVM) with dot kernel. The criteria used when testing their performance were accuracy, sensitivity, specificity, and the area under the curve. Wilcoxon's signed-rank test was used to confirm the accuracy of the classification method. The proposed method was compared to a similar approach reported by Buoutris et al., who analyzed the texture features in a gray-level co-occurrence matrix (GLCM). Using the best-performing classification algorithm (SVM with dot kernel), the accuracy of the proposed approach (95.8 %) was better than that reported by Bountris et al. (92.1 %).

Keywords: image segmentation, edge detection, autofluorescence bronchoscopy, machine learning

Highlights

- A new procedure for the classification of bronchoscopic images into malignant and precancerous cases is presented.
- Wilcoxon's signed-rank test confirmed the efficiency of the new classification procedure.
- The small number of image features (< 10) used in the classification means that the computing-power requirements are small enough for the implementation of the algorithm in an embedded system.
- As machine learning is an essential component of the new procedure, the method can be easily adapted to image characterization in other technical fields.

0 INTRODUCTION

Lung cancer is a malignant disease of the bronchial tubes. The progress of the disease is usually rapid in cases of symptomatic small-cell and non-small-cell lung carcinomas. Early detection of the malignant and precancerous lesions is mandatory for a successful treatment. Autofluorescence bronchoscopy (AFB) is used for the detection of degenerated tissue on the inner surfaces of the bronchial tubes [1]. In cases of a positive AFB finding, a laboratory analysis of a tissue sample is used to confirm or reject the result.

AFB was developed from white-light bronchoscopy (WLB), which was used as a diagnostic tool. In contrast to WLB, AFB utilizes blue light (wavelengths of 380 nm to 460 nm) [2] to [4]. Precancerous (early-stage) lesions are differentiated from healthy bronchial tissue based on the differences between the fluorescent light that is reflected. In the subsequent pathophysiological examination, dysplastic lesions, metaplastic lesions, and carcinomas in situ are characterized by more layers of cells, with diameters ranging from micrometers

to millimeters. They are differentiated from healthy tissue in a pathological examination by the formation of veins under the basal membrane [1] and different concentrations of fluorophores. AFB utilizes the difference in the fluoroscopic properties of malignant and nonmalignant tissues to detect malignancy, making it a superior diagnostic procedure to WLB. In AFB, a healthy mucus membrane emits more green than red light, and unhealthy tissue emits more red than green. Only a little blue light is reflected, either from the healthy or unhealthy tissue. Different implementations of stimuli and sensors can add their particularities to the general picture of fluorescent bronchoscopy.

Many clinical studies have confirmed the utility of AFB in the detection of cellular changes in early-stage lung cancer, with noninvasive neoplastic lesions, small lesions, preneoplastic lesions, and neoplastic changes in tissue detected using state-of-the-art AFB diagnostic systems. Although such detection is possible using WLB, its performance is not as good as that of AFB [2], [5] to [7]. In addition to its utilization of changes in fluorescence in the detection of

*Corr. Author's Address: University of Ljubljana, Faculty of Electrical Engineering, Tržaška cesta 25, 1000 Ljubljana, Slovenia, marko.meza@fe.uni-lj.si

precancerous cells, the superior performance of AFB is attributed to its utilization of algorithms in image characterization. A number of studies showed that AFB significantly outperformed WLB in the detection of preneoplastic and early neoplastic lesions [2], [3] and [8].

However, AFB suffers from a lack of specificity when compared to WLB, with larger numbers of false positives (FPs). According to some studies, the incidence of FPs was as high as 30 % [2], [6], [8] to [10]. Inflammation and other non-life-threatening conditions, which result in changes in cell fluorescence, contribute to the high FP rate in AFB. Thus, to confirm the AFB findings, a biopsy is needed. Biopsies are time consuming and costly and can be distressing for the patient [2] and [10]. Thus far, none of the commercial AFB diagnostic systems (e.g., AFB system LIFE[®], Karl Storz[®], D-light[®], Pentax SAFE 3000[®], and DAFE[®]) have managed to resolve the FP problem.

AFB is designed to produce images in the Red Green Blue (RGB) color space. However, the fluorescent emissions contain only the R and G component. Thus, the image has to be transformed into a grey-scale image, where one of the two colors is represented by the minimum intensity and the other color is represented by the maximum intensity [11].

Although a number of studies have described the use of advanced technologies in diagnosis and treatment [12] to [14], only a few studies have focused on improving the specificity of AFB [15] to [17]. In one study of the spectra of autofluorescent light, the authors added endoscopic optical spectroscopy to AFB to improve its specificity [17]. Bard et al. [15] reported a real-time analysis of the autofluorescent spectrum while manipulating the tissue. The procedure was prone to tissue bleeding. Zeng et al. [16] and Terčelj et al. [17] used experimental apparatuses consisting of an AFB machine and a laboratory spectrometer in noncontact tissue examinations. However, modifications to AFB machines add to their complexity, and as a result, operators need to develop additional skills. Furthermore, the examination times are longer because the patient has to remain intubated, and this should be restricted to the shortest possible duration. Goujon et al. [18] and Qu et al. [19] described the use of follow-up, off-line analyses of spectral images in AFB to reduce the FP results. Other authors reported numerical manipulations of the red and green emissions, combined with different methods for thresholding the images into true positive and FP groups [18] and [20]. They reported a reliability of 79 % using these methods. They also reported that

the addition of the results of WLB slightly improved the findings. In other AFB studies, Bountris et al. [21] and [22] transformed the original color space (RGB) to a more suitable color model (hue saturation value (HSV)) for the purpose of tissue examinations. They reported that the resulting image textures, aided by neural networks, minimized the FP results. Using this approach, it was possible to distinguish between the malignant and the inflamed tissue in the processed images. Haritou et al. [23] developed a computer tool for the off-line classification of AFB images. They used the HSV color space and performed a texture analysis in which sets of characteristic features were defined, depending on the classification type of the image. The texture features they used were Laws' texture energy (TE) and first- and second-order statistics of the data in gray-level co-occurrence matrices (GLCMs). They combined these classification methods with feature-selection methods to develop a reliable and efficient classification method. The final result was a color texture vector consisting of 10 features, which was evaluated for irregularities (malignancy/disease) using a custom neural network. The off-line tool was developed for a procedure evaluation and suggestions for refinements by physicians.

In the present paper we describe the development of a method for the detection of suspicious lesions (regions of interest (ROI)) on AFB images and the classification of these areas into malignant/nonmalignant tissue. First, we created and evaluated the method for the detection of the ROI in comparison with a human expert (see Section 3.1). Next, we extracted a set of image features based on a classifier, which we used to classify the ROI into malignant/nonmalignant tissue. Subsequently, we evaluated the performance of the classifier by comparing its findings with ground-truth data, which were based on the findings (histological analysis) of a tissue biopsy. Finally, we compared the performance of our approach with that of the method developed by Bountris et al. [21] and [22].

1 METHODS

1.1 Data Acquisition

AFB images obtained from patients who attended the Department of Lung Disease and Allergy at the University Clinical Center in Ljubljana, Slovenia were included in the study. All the patients underwent WLB. In cases where malignancy was suspected, AFB (LIFE[®]) images were obtained. The LIFE[®] system consists of a light source, a light fiber, and a camera

with an optical coating. The camera was calibrated before each AFB examination. Using this system, a healthy mucous membrane appears green on the image, and malignant and premalignant lesions appear red or red-brown due to the different fluorescence properties of non-healthy tissue. In all suspicious cases, a biopsy was performed, and the samples were histologically analyzed. The biopsy site was based on the findings of the AFB examination (i.e., abnormal fluorescence properties of the tissue).

The following data were obtained: images and videos of AFB and WLB examinations of 50 patients, results of histological tissue analyses, and other non-relevant study data. No personal data were collected from the database. The study was approved by the Medical Ethics Committee in Slovenia.

The exclusion criteria were the absence of histological data and blurred images due to various causes (e.g., the presence of blood and mucus resulting from intubation, pinching the tissue while obtaining the biopsy sample, and excessive tissue pathology). The final study consisted of 44 images. A distinct area of suspicion and abnormal fluorescence was present in at least one area in each image. The results of the histological analysis of the biopsy tissue samples revealed 22 cases of malignant changes and 22 cases of inflammation (Table 1).

On the WLB images, medical experts marked the ROI (i.e., suspected area of malignancy).

Table 1. Image database

	Malignant tissue changes	Other irregularities
Number of images	22	22

1.2 Procedure for Machine-Supported AFB Reading

Developments in software design, embedded systems, and workstations have had dramatic influences on most aspects of modern life. AFB needs to exploit these modern technologies in diagnostic processes.

A machine-supported AFB system autonomously annotates suspicious areas on an image. An expert then interprets the image reading and makes a diagnosis. Machine support makes the work less stressful, decreases the likelihood of errors, and increases the productivity. Machine-supported AFB reading can be designed to work in real-time or off-line. The latter is easier to implement. A major benefit of machine-supported reading is that it improves the specificity of the AFB readings.

Fig. 1 depicts the steps involved in machine-supported AFB reading. The steps are briefly described in the following subsections.

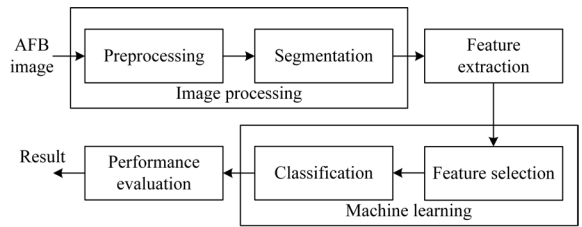


Fig. 1. Flowchart of AFB machine reading

1.2 Preprocessing of AFB Images

Preprocessing is carried out to standardize the image quality (parameters) and produce uniform images for further processing. During preprocessing, the color intensity, contrast, and image sharpness are modified. To improve the homogeneity of the pixel intensity, border-intensity enhancement, morphological closing, and Gaussian low-pass filtering (BCG) are employed [24].

1.2.1 BCG Method

Gaussian BCG low-pass filtering involves border intensity enhancement, morphological closing, and Gaussian low-pass filtering [24]. The border intensity enhances the contrast where the borders between different textures are detected. Morphological closing involves dilation, followed by erosion of the surfaces, based on a predefined set of rules with the purpose of image structuring on defined surfaces. As a result, the border lines between the surfaces are smoothed, small spots are integrated into the surfaces, and straits are withdrawn. Gaussian low-pass filtering reduces the contrast among the different surfaces of the image.

The background and defined objects (ROI) are processed separately using different settings. The background is processed for uniformity, and the ROI is processed for detail enhancement.

In the present study, the BCG parameters were: the projected size of the surface in morphological closing, projected surface size deviation σ , window size Ω , and targeted smoothness in the Gaussian core. Small changes in intensity were considered to denote the inhomogeneity. Consequently, the surfaces should not be small compared to the whole image.

Fig. 2 presents a flowchart of the AFB image-preprocessing steps.

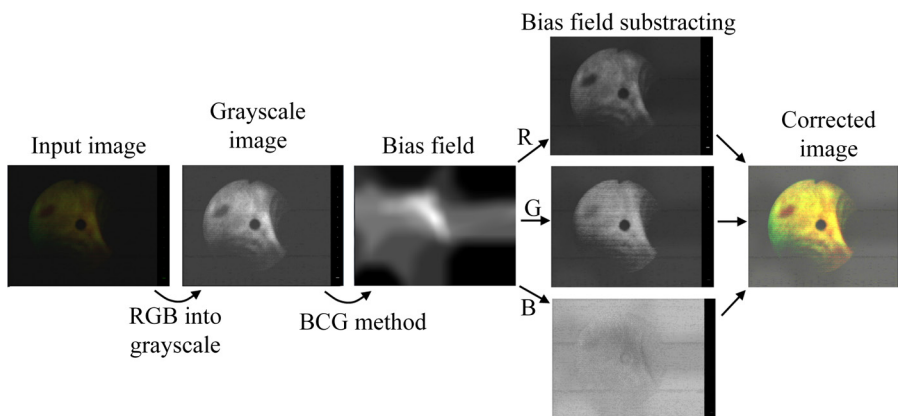


Fig. 2. Flowchart of preprocessing for an AFB image

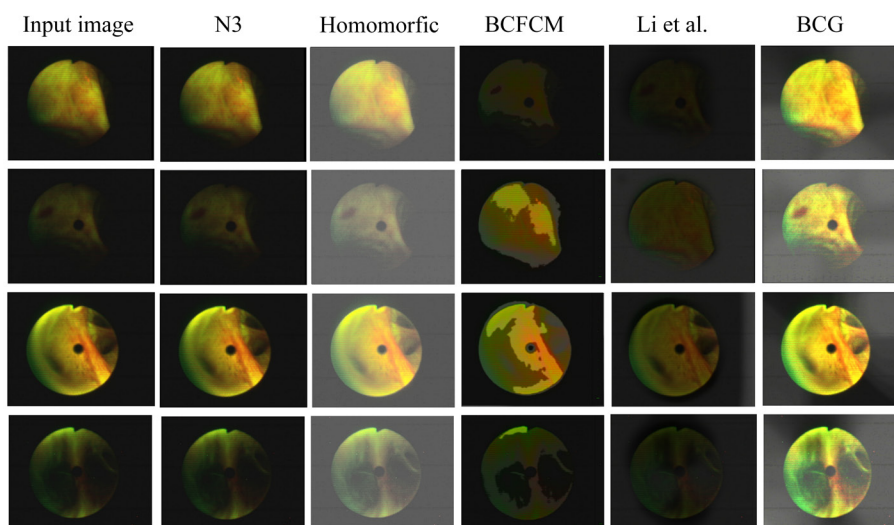


Fig. 3. Assessment of the different preprocessing steps for an AFB image

Following the preprocessing of the AFB image, suspicious areas were detected using the BCG method. Alternatives to the BCG method are the N3 method [25], homomorphic filtration [26], border closing fuzzy C-means [27] and the method of Li et al. [28]. The practical advantages of the BCG method include its computational efficiency, thereby increasing the speed of the operation, as well as its robustness to noise and a dynamic range of possible inputs. The method is particularly useful for processing database images produced in similar environments.

1.3 Image Segmentation and Definition of the ROI

The intensity of the fluorescence light in AFB is influenced by the excitation wavelength λ , the absorption, the scattering, and the distance [29] as well as the different fluorescence properties of malignant

and non-malignant tissue. The latter is used to discriminate malignant and non-malignant tissue.

During the imaging, the intensity of each image was calibrated for different distances. The definition of the ROI was based on the preprocessed AFB image. All non-healthy tissue was included in the ROI. Malignant changes, inflammation, bruises, and the excessive age degeneration of the tissue appeared similar on the image and needed to be investigated in detail. Once defined, the ROI was compared with the WLB image and the results of the physician's observation.

The R/G intensity ratio of the surface of the image was calculated, and the results were presented in a gray image, followed by filtering. The signal-to-noise (S/N) ratio was increased by lowering the noise while taking care to preserve the edges. Different filters were used: simple averaging, Gaussian filtering, and

anisotropic diffusion filtering, and the last of these yielded the best results.

1.3.1 Anisotropic Filtering

Anisotropic filtering for image processing was performed in accordance with the anisotropic diffusion method of Perona and Malik [30]. Using this method, a line (or curve) of filtering is first defined, which is then performed along this line. The filter is used to preserve the edges and smooth out the surfaces [31]. The process is iterative and semi-reversible. The differential equations used in anisotropic diffusion filtering have been described earlier [31].

The requirements are:

- causality: Iterations must not produce new (false) features;
 - at a minimum, edge sharpness and position must be preserved;
 - intra-region filtering is prohibited;
 - edges should ideally be enhanced.
- Filtering is described by Eq. (1):

$$\partial_t u = \text{div}(g(x, y, t)\nabla u) = g(x, y, t)\Delta u + \nabla g \nabla u, \quad (1)$$

where u is the intensity of the image element, and $g(x, y, t)$ is the diffusion coefficient (function of position and time). As filtering intensifies with the number of iterations, the diffusion coefficient g was small (0) on the edges and large (1) within the surfaces. The brightness gradient $|\nabla u(x, y, t)|$ was used for g modulation. The diffusion coefficient g was a non-negative, monotonously decreasing function of the intensity gradient ∇u , with the boundary condition $g(0)=1$. Shaping g changed the diffusion rate. When $g=1$, the diffusion became linear, and the properties of the image had no effect on the filtering.

To enhance the edges while smoothing out the surfaces, Eqs. (2) or (3) was used:

$$g(\nabla u) = e^{-\left(\frac{|\nabla u|}{\lambda}\right)^2}, \quad (2)$$

$$g(\nabla u) = \frac{1}{1 + \left(\frac{|\nabla u|}{\lambda}\right)^2}. \quad (3)$$

Eq. (2) was used to enhance the contrast intensity, and Eq. (3) was used to enhance the filtering on wide surfaces and modulate g [32].

The parameters were the number of iterations n and the spatial scaling factor λ of the gradient u . Noisy images require a larger λ , and iterations n wipe out the image details while preserving well-defined edges.

A numerically similar application, solving the Fourier law of heat flow, was speed optimized for implementation in an embedded system [33]. The author reported that this method was 110 times faster than the existing commercial solutions. The mathematics employed in the present study are similar to those used in the method described in [33]. Thus, verified guidelines for the speed optimization of filtering for real-time, machine-supported AFB diagnostics exist.

1.3.2 Canny Algorithm for Edge Detection

The Canny algorithm proceeds as follows. First, a Gaussian filter is used for moderate filtering of an AFB image [34]. Parameter σ (standard deviation of the Gaussian distribution) modulates the filtering intensity. The diffusion coefficient g is calculated by Eq. (4), and the angle of searching for an edge is calculated by Eq. (5).

$$g(x, y) = \sqrt{G_x^2 + G_y^2}, \quad (4)$$

$$\alpha(x, y) = \arctan \frac{G_y}{G_x}, \quad (5)$$

G_x and G_y are calculated using the Sobel, Prewitt or Roberts's operator. The edge points determined in Eq. (4) give rise to edges with the magnitude of the image gradient. The algorithm then tracks the top of these edges, and any pixels that are not on the top of the edge are set to zero to produce a thin line in the output. This is known as non-maximal suppression. The edge pixels are then thresholded by hysteresis thresholding, which is based on the use of two thresholds: $T1$ and $T2$, and $T1 > T2$. Edge pixels with values greater than $T2$ are considered strong edge pixels, and edge pixels with values between $T1$ and $T2$ are considered weak edge pixels. Values below $T1$ form surfaces.

A flowchart of the Canny algorithm is presented in Fig. 4. As shown in the figure, as the Gaussian filter lowered the noise level, the S/N ratio increased. The horizontal (x axes) and vertical (y axes) gradients of the image element intensities were calculated. The gradient magnitude was calculated using Eq. (4). Local maxima were found. All the other gradients were set to 0.

The threshold filter separates the edge pixels from the background. The inbuilt hysteresis in the filter allows for a distinction between the edges and the background. Pixels with intensities below the

lower threshold form the background, and those with intensities above the upper threshold form edges. Pixels in-between these thresholds represent edges if they have edge-neighbors; otherwise, they form the background.

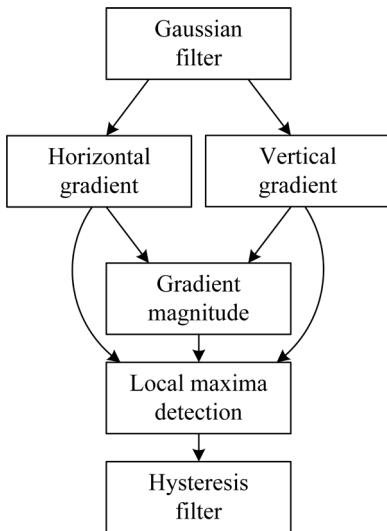


Fig. 4. Flowchart of AFB image preprocessing

1.4 Feature Extraction

The surface-classification method of Bountris et al. [21] and [22] was used. This method is based on a feature study. Ideally, only a few features with lots of content are identified. The presence of multiple features increases the noise level, which interferes with the efficiency of the surface classification. Excessive image preprocessing prior to the feature search can potentially result in the depletion of TE. To preserve TE, we repeated the feature search using a combination of 25 Laws' image filters [21] and first- and second-order statistics. Each ROI was mapped from the RGB to the HSV color space. Component H was used in the analysis. The combination of 25 Laws' image filters and the results of the ROI mapping yielded 25 TE images. Seven first-order statistics were calculated for each image, resulting in 175 TE features. The calculation of GLCM ($d=1$, $\theta=45^\circ$), and 22 first-order statistics produced an additional 550 TE features. Each ROI was characterized by 725 TE features, which were ordered into feature vectors. The dimension of each feature vector was impractically high. Information-rich features are mandatory for differentiating between the malignant and FP areas. Therefore, we employed principal component analysis (PCA) to generate a reduced number of information-rich features.

1.5 Feature Reduction

PCA was performed to reduce the data into smaller numbers of information-enriched features [35] and [36]. These features (inputs to the method) were then mapped into a space with fewer dimensions. The data variance in lower-dimensional space needs to be high to guarantee a high correlation between the image properties and the corresponding image feature. Thus, PCA was performed to transform the correlated (linearly dependent) features into uncorrelated (linearly independent) features. The resulting features were orthogonal and formed the base of the feature space.

The features were ranked according to their information relevance, with features having higher variance considered more important in the image. The most important features were used in the image analysis, and the least important features were considered noise [35]. PCA was also applied to the feature vectors. A subset of the resulting features was then used to build a machine-learning model for the classification of the samples into malignant and nonmalignant cases. In the iterative PCA, which was run using different settings, we selected the setting that resulted in the best classification models.

1.6 Image Classification

The bronchial images were classified using a combination of machine learning and calculation and the classification of information-rich features, all of which were implemented using computationally efficient algorithms. The following supervised-learning classification algorithms were tested in the creation of the classification models: naive Bayes classifier, K-nearest-neighbor (K-NN), and support vector machines with dot-kernel-type classifier (SVM). The dot kernel used was defined by $k(x, y) = x \times y$ [37].

1.7 Assessment

To assess the performance of the classification model, we computed an accuracy sensitivity and specificity measure and then compared the results with those of other studies [21] and [22]. As the number of images was small, we applied the procedure of uniform sampling, with exchange (bootstrap) [38] to assess the efficiency of the machine learning.

2 PROPOSED NOVEL METHOD FOR FEATURE EXTRACTION

The method for extracting the texture features draws on the work of Bountris et al. [21] and [22]. These texture features and an image histogram were used to produce the FOS. The histogram (HSV space) graphically showed the distribution of the color intensity and provided direction on additional information that was needed to improve the image reading.

In our approach, we created features by plotting the red (R) and green (G) channel histogram of a ROI in one graph. A fixed area within a ROI was chosen and analyzed in all cases. Both the R and G histograms of the ROI showed bell-type distributions. Fig. 5 presents an example of a histogram where the *x* axis shows the channel intensity (0 to 255, 8-bit resolution) and the *y* axis shows the number of corresponding intensity pixels within the ROI. The histograms of both channels were then approximated using the Gaussian-approximation function. The function (see Eq. 6) for each channel was defined by the values of the mean μ , the standard deviation of σ , and the peak value M . The computed Gaussian approximation of the red and green channels of the selected image is also shown in Fig. 5. The histograms of all the images were similar. In all cases, although μ , σ , and M differed, a semi-normal distribution was always present.

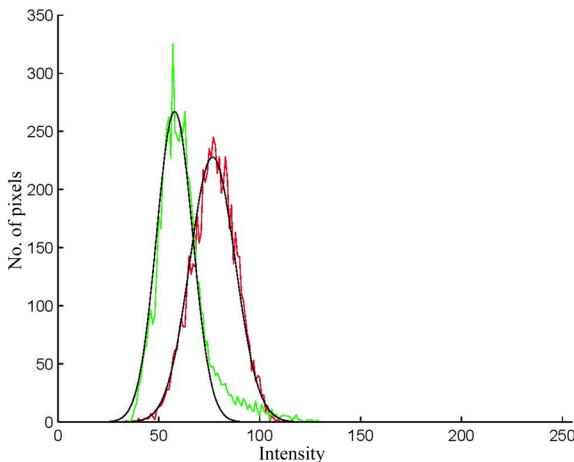


Fig. 5. Histogram of the R and G plane in an AFB image

Eq. (6) is the scaled Gaussian function that was used to model the R and G histograms in Fig. 5.

$$y(x, M, \mu, \sigma^2) = \frac{M}{\sqrt{2\sigma^2\pi}} e^{-\frac{(x-\mu)^2}{2\sigma^2}} \quad (6)$$

The parameters of the Gaussian functions (μ , σ , and M) and the cross-section of the two curves then served as features for the machine-learning model. Fig. 6 shows a flowchart of the feature extraction.

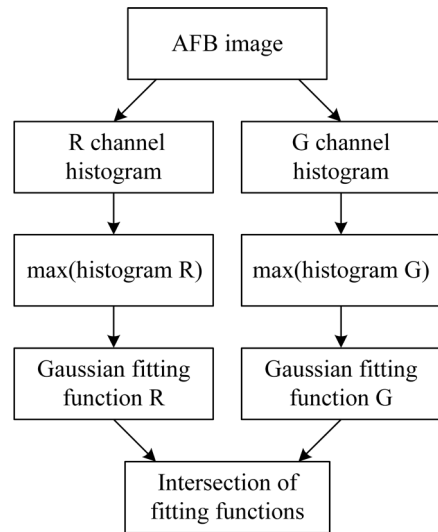


Fig. 6. Feature extraction

In total, seven features were extracted from each sample. The extracted features were then used to build classification models for the discrimination of the malignant and nonmalignant cases. Next, we tested the performance of the classification models containing the extracted features using naive Bayes, K-NN, and SVM with dot kernel machine-learning algorithms. As a performance parameter, we observed the accuracy measure.

3 RESULTS

3.1 Detection of a Suspicious Area

In each WLB image, a medical expert first selected the ROI, marking what he/she considered a suspicious area (malignant tissue). The expert-marked ROI was then compared with the machine-defined ROI. When comparing the machine-defined ROI with the expert-defined ROI, the former was considered as ground truth. In the comparison, each pixel of the machine- and expert-defined ROI was compared.

False-positive errors (FPEs) and false-negative errors (FNEs) were recorded. The mean values and standard deviations of the FPEs and FNE during the image processing were calculated in the RGB and HSV color spaces (Table 2). It is clear that the image processing in the HSV color space produced slightly

better results than the image processing in the RGB space.

Table 2. Comparison of ROI detection methods

	FPE [%]		FNE [%]	
	Mean	Std.	Mean	Std.
RGB	11.1	2.4	11.0	3.7
HSV	8.7	2.5	8.4	2.7

3.2 Classification

We compared the classification method of Bountris et al. [21] and [22] with our proposed method. As we were not able to obtain data from the authors of the reported method, we evaluated both approaches based on our own data.

The dataset consisted of 44 images, in which a ROI was identified. Malignancy was confirmed in 22 of the images. Irregularities present in the other 22 images had raised a suspicion of malignancy. These were biopsied but found to be nonmalignant. We performed randomized, stratified subsampling of 15 samples from the malignant dataset and 15 samples from the nonmalignant dataset. These sample cases were then used for learning. The other 14 cases (seven from the malignant set and seven from the nonmalignant set) were used for testing (Table 3).

Table 3. Learning and evaluation of the image sets

	Malignant tissue	Other tissue irregularities
Learning set	15	15
Testing set	7	7
Sum of images	22	22

3.2.1 Generation of Texture Features Using the Method of Bountris et al. [21] and [22]

We repeated the feature-extraction method described by Bountris et al. [21] and [22]. Fig. 7 outlines the

process used to produce 25 TE images of the ROI from the initial image [23]. The ROI was first defined in the AFB image. The area of the ROI, from which a biopsy was taken, was the area for machine processing. The area was then transformed into HSV color space. The H component was used for the convolution with 25 Laws' masks. This resulted in 25 TE images. Twenty-nine texture statistics were then calculated from each image, resulting in 725 features per ROI.

Selection of texture features using the method of Bountris et al. [21] and [22]

PCA was applied to reduce the feature space. In our case, we reduced 725 features to 10 independent features. These features were then used for machine learning. Several machine-learning algorithms (naive Bayes, K-NN, and SVM with dot kernel) were tested. The SVM with the dot kernel produced the best classification results. The results obtained were similar to those reported by Bountris et al. [21] and [22], who reported an accuracy of 91.2 % in their dataset. Therefore, we believe that we have managed to repeat their method accurately.

Proposed Method for Feature-Set Generation

We used the same learning/test dataset to evaluate the proposed method of feature extraction. We extracted a total of seven features from each ROI. The extracted features were Gaussian fitted parameters of both the red and green channels and the intersection points of both fitting curves. For a description of the feature-extraction method, please see Section 2. Naive Bayes, K-NN, and SVM with dot-kernel machine-learning algorithms were tested and used in the creation of the model.

3.3 Classification Results

The classification results obtained using the proposed method were evaluated by comparing them with the results obtained using the methods of Bountris

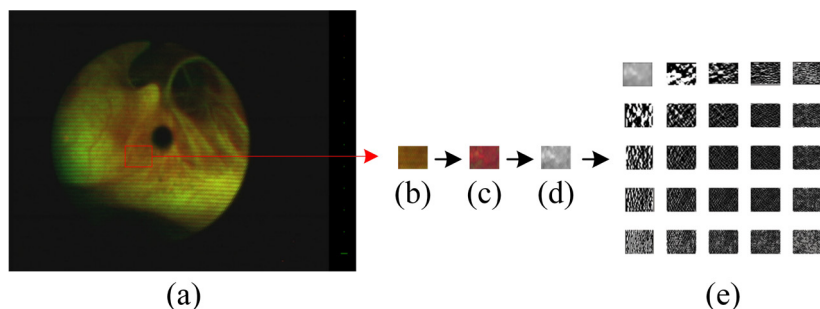


Fig. 7. Process of texture-feature selection

et al. [21] and [22]. The results of both methods are presented in Table 4.

Table 4. Comparison of both methods

	Method of Bountris et al. [21] and [22]	Proposed method
Classifier	Accuracy [%]	Accuracy [%]
K-NN	90.7	90.9
Naive Bayes	90.4	91.5
SVM with dot kernel	92.1	95.8
Average accuracy	91.1	92.7

Accuracy was considered as the most important parameter in the assessment of both methods. Other parameters that were assessed are presented in Table 5. The naive Bayes classifier was used to obtain the data in Table 5. The proposed approach yielded better results, with substantially less computing time than the method proposed by Bountris et al. [21] and [22].

Table 5. Comparison of other measures in the assessment of the methods (according to the naive Bayes classifier)

NB	Bountris et al. method [21] and [22]	Proposed method
Sensitivity [%]	81.82	95.45
Specificity [%]	90.91	86.36
Accuracy [%]	93.33	88.33
Recall [%]	83.33	95.00
AUC	0.883	0.958

Wilcoxon's signed-rank test was used to compare the performance of both methods. To validate the null hypothesis that both methods would produce similar results, using a statistical confidence level of $\alpha = 0.05$. The results of Wilcoxon's signed-rank test are shown in Table 6.

Table 6. Results of Wilcoxon's signed-rank test of both methods

	Accuracy	Recall	AUC
p	0.0112	0.0052	0.00063323

4 DISCUSSION AND CONCLUSION

We implemented and successfully tested a novel approach to the detection and classification of malignant tissue in AFB images. Using the proposed approach, we were able to successfully discriminate malignant and nonmalignant tissue in AFB images in borderline cases.

In the proposed approach, a suspicious area on an image was identified using the BCG method. Suspicious areas detected by an expert were then compared with those identified using the proposed algorithm. The algorithm produced usable results. It detected the ROI, performing slightly better when used in the HSV color space.

From each suspicious area (ROI), a tissue biopsy sample was obtained. This tissue sample was sent for histological analysis, and the results were used as ground truth when determining whether a tissue sample was malignant or nonmalignant. From the determined ROI and ground-truth data, a test/learn dataset was created for the classification of each ROI as malignant/nonmalignant.

We tested two approaches to tissue classification. We repeated the approach described by Bountris et al. [21] and [22] and compared it with our approach. The main difference between the two approaches was the different set of features that were extracted from the AFB images. The method of Bountris et al. [21] and [22] is based on texture features, whereas our approach is based on the difference in the fluoroscopic properties of malignant and nonmalignant tissue. We discriminated between the two types of tissue based on the red and green distributions in the histogram of the AFB image. We modeled the red and green channel histograms using a Gaussian fitting function and used the fitted parameters as features to discriminate between the two types of tissue.

Using the proposed approach, we obtained similar results to those reported by Bountris et al. [21] and [22]. Therefore, we believe that our implementation of their approach was accurate. The proposed approach yielded better accuracy than that reported by Bountris et al. [21] and [22]. They achieved an accuracy of 92.1 %. With our approach, using the SVM algorithm with the dot kernel, we achieved an accuracy of 95.8 %. In addition, our approach is computationally more efficient, as the number of features used for the modeling is small ($n = 7$). In contrast, a large number of features ($n = 725$) is used in the approach of Bountris et al. [21] and [22]. The relatively small number of features enabled us to create a classification model based on a relatively small sample set. Furthermore, over-fitting did not occur due to the small number of features compared to the number of samples.

We should stress that we tested other schemes in the validation of the models' performance (cross-fold validation). We omitted one scheme (data not reported). We achieved similar and consistent performance results with these tests.

The results of this study show that it is possible to partially automate the detection and classification of malignancy in suspicious areas during AFB examinations. However, the final interpretation of suspicious areas depends on the decision of an expert in the field.

6 REFERENCES

- [1] Wang, K.P., Mehta, A.C., Turner Jr, J.F. (eds.) (2011). *Flexible Bronchoscopy*. John Wiley & Sons, Chichester.
- [2] Wang, Y., Wang, Q., Feng, J., Wu, Q. (2013). Comparison of auto fluorescence imaging bronchoscopy and white light bronchoscopy for detection of lung cancers and precancerous lesions. *Patient Preference and Adherence*, vol. 7, p. 621-631, DOI:10.2147/PPA.S46749.
- [3] Liu, Z., Zhang, Y., Li, Y.P., Ma, J., Shi, F., Zhao, D.F., Li, J.M., Zhang, Y.Z. (2016). Clinical relevance of using autofluorescence bronchoscopy and white light bronchoscopy in different types of airway lesions. *Journal of Cancer Research and Therapeutics*, vol. 12, no. 1, p. 69-72, DOI:10.4103/0973-1482.147731.
- [4] van den Bergh, H. (2003). Early detection of lung cancer and the role of endoscopic fluorescence imaging. *Medical Laser Application*, vol. 18, no. 1, p. 20-26, DOI:10.1078/1615-1615-00083.
- [5] Bezel, P., Tischler, V., Robinson, C., Baumüller, S., Bode-Lesniewska, B., Kohler, M., Freitag, L., Franzen, D. (2016). Diagnostic value of bronchoalveolar lavage for diagnosis of suspected peripheral lung cancer. *Clinical Lung Cancer*, vol. 17, no. 5, p. e151-e156, DOI:10.1016/j.clcc.2015.12.012.
- [6] Edell, E., Lam, S., Pass, H., Miller, Y.E., Sutudja, T., Kennedy, T., Loewen, G. Keith, R.L. (2009). Detection and localization of intraepithelial neoplasia and invasive carcinoma using fluorescence-reflectance bronchoscopy: an international, multicenter clinical trial. *Journal of Thoracic Oncology*, vol. 4, no. 1, p. 49-54, DOI:10.1097/JTO.0b013e3181914506.
- [7] Häussinger, K., Becker, H., Stanzel, F., Kreuzer, A., Schmidt, B., Strausz, J., Cavaliere, S., Herth, F., Kohlhäufel, M., Müller, K.-M., Huber, R.-M., Pichlmeier, U., Bolliger, Ch.T. (2005). Autofluorescence bronchoscopy with white light bronchoscopy compared with white light bronchoscopy alone for the detection of precancerous lesions: a European randomised controlled multicentre trial. *Thorax*, vol. 60, no. 6, p. 496-503, DOI:10.1136/thx.2005.041475.
- [8] Moghissi, K., Dixon, K., Stringer, M.R. (2008). Current indications and future perspective of fluorescence bronchoscopy: a review study. *Photodiagnosis and Photodynamic Therapy*, vol. 5, no. 4, p. 238-246, DOI:10.1016/j.pdpdt.2009.01.008.
- [9] McGregor, H.C., Short, M.A., McWilliams, A., Shaipanich, T., Ionescu, D.N., Zhao, J., Wang, W., Chen, G., Lam, S. Zeng, H. (2016). Real-time endoscopic Raman spectroscopy for in vivo early lung cancer detection. *Journal of Biophotonics*, vol. 10, no. 1, p. 98-110, DOI:10.1002/jbio.201500204.
- [10] Leong, S., Shaipanich, T., Lam, S., Yasufuku, K. (2013). Diagnostic bronchoscopy—current and future perspectives. *Journal of Thoracic Disease*, vol. 5, no. 5, p. S498-S510, DOI:10.3978/j.issn.2072-1439.2013.09.08.
- [11] Lee, P., van den Berg, R.M., Lam, S., Gazdar, A.F., Grunberg, K., McWilliams, A., LeRiche, J., Postmus, P.E., Sutudja, T.G. (2009). Color fluorescence ratio for detection of bronchial dysplasia and carcinoma in situ. *Clinical Cancer Research*, vol. 15, no. 14, p. 4700-4705, DOI:10.1158/1078-0432.CCR-08-1644.
- [12] Cajal, C., Santolaria, J., Samper, D., Garrido, A. (2015). Simulation of laser triangulation sensors scanning for design and evaluation purposes. *International Journal of Simulation Modelling*, vol. 14, no. 2, p. 250-264, DOI:10.2507/IJSIMM14(2)6.296.
- [13] Jerbic, B., Nikolic, G., Chudy, D., Svaco, M., Sekoranja, B. (2015). Robotic application in neurosurgery using intelligent visual and haptic interaction. *International Journal of Simulation Modelling*, vol. 14, no. 1, p. 71-84, DOI:10.2507/IJSIMM14(1)7.290.
- [14] Martinović, M., Stoić, A., Kiš, D. (2008). Segmentation of the CT image using self-organizing neural networks. *Tehnički vjesnik – Technical Gazette*, vol. 15, no. 4. p. 23-28.
- [15] Bard, M.P., Amelink, A., Skurichina, M., Hegt, V.N., Duin, R.P., Sterenborg, H.J., Hoogsteden, H., Aerts, J.G. (2006). Optical spectroscopy for the classification of malignant lesions of the bronchial tree. *Chest*, vol. 129, no. 4, p. 995-1001, DOI:10.1378/chest.129.4.995.
- [16] Zeng, H., Petek, M., Tercelj Zorman, M., McWilliams, A., Palcic, B., Lam, S. (2004). Integrated endoscopy system for simultaneous imaging and spectroscopy for early lung cancer detection. *Optics Letters*, vol. 29, no. 6, p. 587-589, DOI:10.1364/OL.29.000587.
- [17] Tercelj, M., Zeng, H., Petek, M., Rott, T., Palcic, B. (2005). Acquisition of fluorescence and reflectance spectra during routine bronchoscopy examinations using the ClearVu Elite™ device: Pilot study. *Lung Cancer*, vol. 50, no. 1, p. 35-42, DOI:10.1016/j.lungcan.2005.05.028.
- [18] Goujon, D., Zellweger, M., Radu, A., Grosjean, P., Weber, B.-C., van den Bergh, H., Monnier, P., Wagnieres, G. (2003). In vivo autofluorescence imaging of early cancers in the human tracheobronchial tree with a spectrally optimized system. *Journal of Biomedical Optics*, vol. 8, no. 1, p. 17-25, DOI:10.1117/1.1528594.
- [19] Qu, J.Y., Chang, H., Xiong, S. (2002). Fluorescence spectral imaging for characterization of tissue based on multivariate statistical analysis. *JOSA A*, vol. 19, no. 9, p. 1823-1831, DOI:10.1364/JOSAA.19.001823.
- [20] Gabrecht, T., Radu, A., Zellweger, M., Lovisa, B., Goujon, D., Grosjean, P., van der Bergh, H., Monnier, P., Wagnières, G. (2007). Autofluorescence bronchoscopy: Clinical experience with an optimized system in head and neck cancer patients. *Medical Laser Application*, vol. 22, no. 3, p. 185-192, DOI:10.1016/j.mla.2007.09.003.
- [21] Bountris, P., Apostolou, A., Haritou, M., Passalidou, E., Koutsouris, D. (2009). Combined texture features for improved classification of suspicious areas in autofluorescence bronchoscopy. *9th International Conference on Information Technology and Applications in Biomedicine*, p. 1-4, DOI:10.1109/ITAB.2009.5394448.

- [22] Bountris, P., Haritou, M., Passalidou, E., Apostolou, N., Koutsouris, D. (2009). Detection and classification of suspicious areas in autofluorescence bronchoscopy. *World Congress on Medical Physics and Biomedical Engineering*, p. 1838-1841, DOI:10.1007/978-3-642-03882-2_488.
- [23] Haritou, M., Bountris, P., Passalidou, E., Koklonis, K., Koutsouris, D. (2014). An image analysis tool for the classification of lesions suspicious for malignancy in autofluorescence bronchoscopy. *Biomedical Spectroscopy and Imaging*, vol. 3, no. 2, p. 167-183, DOI:10.3233/BSI-140079.
- [24] Chambers, O., Milenkovic, J., Tasic, J.F. (2014). A pre-processing scheme for real-time registration of dynamic contrast-enhanced magnetic resonance images. *Journal of Real-Time Image Processing*, p. 1-10, DOI:10.1007/s11554-014-0468-0.
- [25] Sled, J.G., Zijdenbos, A.P., Evans, A.C. (1997). A comparison of retrospective intensity non-uniformity correction methods for MRI. *Biennial International Conference on Information Processing in Medical Imaging*, p. 459-464, DOI:10.1007/3-540-63046-5_43.
- [26] Brinkmann, B.H., Manduca, A., Robb, R.A. (1998). Optimized homomorphic unsharp masking for MR grayscale inhomogeneity correction. *IEEE Transactions on Medical Imaging*, vol. 17, no. 2, p. 161-171, DOI:10.1109/42.700729.
- [27] Ahmed, M.N., Yamany, S.M., Mohamed, N., Farag, A.A., Moriarty, T. (2002). A modified fuzzy c-means algorithm for bias field estimation and segmentation of MRI data. *IEEE Transactions on Medical Imaging*, vol. 21, no. 3, p. 193-199, DOI:10.1109/42.996338.
- [28] Li, C., Huang, R., Ding, Z., Gatenby, J.C., Metaxas, D.N., Gore, J.C. (2011). A level set method for image segmentation in the presence of intensity inhomogeneities with application to MRI. *IEEE Transactions on Image Processing*, vol. 20, no. 7, p. 2007-2016, DOI:10.1109/TIP.2011.2146190.
- [29] Fawzy, Y.S., Petek, M., Tercelj, M., Zeng, H. (2006). In vivo assessment and evaluation of lung tissue morphologic and physiological changes from non-contact endoscopic reflectance spectroscopy for improving lung cancer detection. *Journal of Biomedical Optics*, vol. 11, no. 4, p. 044003, DOI:10.1117/1.2337529.
- [30] Perona, P., Malik, J. (1990). Scale-space and edge detection using anisotropic diffusion. *IEEE Transactions on Pattern Analysis and Machine Intelligence*, vol. 12, no. 7, p. 629-639, DOI:10.1109/34.56205.
- [31] Weickert, J. (1998). *Anisotropic Diffusion in Image Processing*, p. 59-60. Teubner, Stuttgart.
- [32] Kovese, P.D. (2000). MATLAB and Octave functions for computer vision and image processing. from <http://www.csse.uwa.edu.au/~pk/Research/MatlabFns/#match>, accessed on 2016-05-25.
- [33] Jenko, M. (2015). Numerical cooking for pasteurized soft boiled eggs. *Strojniški vestnik - Journal of Mechanical Engineering*, vol. 61, no. 5, p. 319-329, DOI:10.5545/sv-jme.2014.2187.
- [34] Maini, R., & Aggarwal, H. (2009). Study and comparison of various image edge detection techniques. *International Journal of Image Processing*, vol. 3, no. 1, p. 1-11.
- [35] Theodoridis, S., Pikrakis, A., Koutroumbas, K., Cavouras, D. (2010). *Introduction to Pattern Recognition: A Matlab Approach*. Academic Press, Oxford.
- [36] Duda, R.O., Hart, P.E., Stork, D.G. (2012). *Pattern Classification*. John Wiley & Sons, New York.
- [37] Hofmann, M., Klinkenberg, R. (eds.). (2013). *RapidMiner: Data Mining Use Cases and Business Analytics Applications*. Chapman & Hall/CRC Data Mining and Knowledge Discovery Series. CRC Press, Boca Raton.
- [38] Molinaro, A.M., Simon, R., Pfeiffer, R.M. (2005). Prediction error estimation: a comparison of resampling methods. *Bioinformatics*, vol. 21, no. 15, p. 3301-3307, DOI:10.1093/bioinformatics/bti499.

A Novel Excitation Approach to Ultrasonically-Assisted Cylindrical Grinding

Vytautas Ostaševičius¹ – Vytautas Jūrėnas¹ – Andrius Vilkauskas¹ – Gytautas Balevičius^{1,*}
– Andrius Senkus² – Eglė Jotautienė²

¹ Kaunas University of Technology, Institute of Mechatronics, Lithuania

² Aleksandras Stulginskis University, Institute of Agricultural Engineering and Safety, Lithuania

Usage of ultrasound is prevalent in a wide range of industrial applications; it is employed in aiding the removal of hard-to-machine materials. In such cases, special care needs to be taken in designing an ultrasonic horn, as the geometrical make-up of this part that strongly influences the ultrasonic power output, frequency, and amplitude transferred to the area of effect. This article proposes a novel solution to the excitation of rotating interfaces: the excitation of the workpiece in cylindrical grinding. The approach focuses on the excitation of stationary centres, holding the workpiece, rather than the workpiece itself. The modelling and development procedures for a high-power actuator as well as experimental verifications to the validity and effectiveness of the approach are provided.

Keywords: ultrasonic horn, cylindrical grinding, finite element method, vibration assisted machining, external excitation, rotating interface excitation

Highlights

- A design for a robust approach to excitation of rotating parts is proposed.
- Appropriate dimensions of proposed actuator design are determined with FEM and parametric sweep.
- The effectiveness of the approach is observed through surface roughness improvements, from experimental runs.

0 INTRODUCTION

The rapid emergence and advancement of hybrid manufacturing processes (HMP) can be considered the industry's direct response to the growing need for technologies employing hard-to-machine-materials (ceramics, glass, etc.). As described in [1], HMP are controlled applications of simultaneously interacting machining mechanisms that are of high relevance to the process. The main goal of HMP is to achieve what Schuh et al. [2] refer to as the "1+1=3" synergy effect on the overall machining process. This effect implies not only the supplementation among the interacting machining mechanisms but also the robustness of the approach in relation to the application costs and constraints (modification of the existing machines, number of additional modules required etc.).

Vibration-assisted machining (VAM) methods are a highly researched and developed group of HMP. The basic principle of VAM employs a conventional machining process (drilling, turning, grinding, etc.) and supplements it with vibrational excitation of either the tool, the workpiece, or both. A sizeable amount of research has been conducted, covering different VAM processes. Graževičiūtė et al. [3] using a specifically designed cutting tool, supplemented with an ultrasonic actuator, observed improvements in the surface quality during turning. Ostaševičius et al. [4] developed a finite element

model of a vibrating milling tool and demonstrated that high-frequency vibrations superimposed onto the continuous movement of the tool lead to milling process stabilization with superior surface finish in comparison to conventional machining. Ultrasonically assisted dry grinding (UADG) has been employed by Tawakoli and Azarhoushang [5] to compensate for low material removal rates, poor surface quality, and other issues prevalent in the conventional dry grinding (CDG), due to lack of coolant. Ultrasonic vibration was found to be effective in aiding the grinding of difficult to cut materials (titanium, ceramics, etc.); researchers attributed it to the reduction of temperature and tool wear due to longitudinal vibration [6]. The use of vibration for grinding is more prevalent in grinding on a machine with a vertical grinding spindle [7], as longitudinal vibration is considered to provide the highest penetration power. However, it is possible to transform longitudinal vibrations into transverse modes for horizontal processes, such as turning or cylindrical grinding. In these processes, the workpiece would need to be excited in the transverse mode. Workpiece excitation holds great promise, as demonstrated by Liang et al. [8] in their ultrasonically assisted grinding of monocrystalline silicon.

The application of vibrational excitation to static parts (lathe tool, statically mounted workpiece, etc.) is rather straightforward. The modifications limit themselves to the mounting of an actuator to the said

part. The application to moving parts (rotating tools and workpieces), however, is more complex, as it requires additional modules to be put in place to drive and control the actuators situated on the moving part.

The authors of this paper propose a novel, robust alternative for rotating component excitation that has the potential to be applied to any process involving a rotating tool or workpiece. Instead of mounting the actuator on the rotating interface, it is to be mounted immediately outside it, either through a collar or bracket link, thus eliminating the need for additional modules. Such an approach, to the best of the authors' knowledge, has not previously been applied.

This article aims to develop and test a prototype of the proposed approach. The main challenge is the development of an actuator that possesses reasonable power requirements, yet remains able to transfer the vibration between the moving and static interfaces. Therefore, this article, firstly, concerns itself with the behaviour of the excitation target; modelling, development, and testing of the actuator follow immediately afterward.

Overall representation of the research flow, can be found in Fig. A1 (Appendix A).

1 DEVELOPMENT OF THE EXCITATION SET-UP

To maintain a sufficient level of control during the initial testing stages, a process with a relatively slowly rotating part had to be chosen. Such a part can be recognized as the workpiece in the cylindrical surface grinding process. When considering the specific set-up for the Supertec G32P-100NC grinding machine (Fig. 1), it can be seen that the actuator (1) can be mounted via a clamp collar (2) onto the sleeve of the tailstock (3); in the initial analysis stages, interaction between the workpiece (4) and tool (5) is ignored. Two workpieces (a uniform and a stepped shaft) are used in experiments.

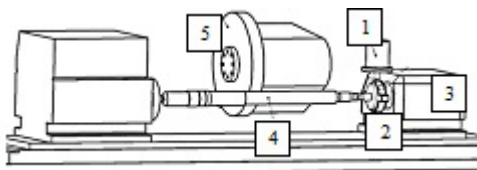


Fig. 1. Excitation set-up for Supertec G32P-100NC grinding machine: 1) actuator; 2) clamp collar; 3) tail stock; 4) workpiece; 5) tool

The studies concerning the workpiece behaviour are aimed at determining the most suitable excitation frequencies and required excitation force. These studies

are tackled first, since their results serve as inputs for further study and development of the actuator. The actuator development requires the derivation and adjustment of ultrasonic horn dimensions, to suit the operation to workpiece frequency. Upon completion of the design, the viability of the excitation approach is tested by determining the power requirements for producing expected workpiece excitation amplitudes.

1.1 Dynamic Behaviour of the Workpiece

Before studying the behaviour of the workpiece any further, a set of target conditions is set forth: 1. Since the tool approaches perpendicularly to the workpiece axis, the latter should vibrate in a transverse mode; 2. The frequency of excitation must not be lower than 15 kHz, as lower values would be too far from the ultrasonic threshold; 3. The target amplitude of excitation needs to be above 1 μm , as most encountered applications tend to employ amplitudes of such orders of magnitude. The first two conditions can be tackled by employing modal analysis.

If the law of motion of the excited end of the workpiece is to be considered known and defined by a nodal displacement vector \mathbf{U}_K , the block form of the equation of motion (EOM) of the workpiece is written as Eq. (1):

$$\begin{bmatrix} \mathbf{M}_{NN} & \mathbf{M}_{NK} \\ \mathbf{M}_{KN} & \mathbf{M}_{KK} \end{bmatrix} \begin{Bmatrix} \ddot{\mathbf{U}}_N \\ \ddot{\mathbf{U}}_K \end{Bmatrix} + \begin{bmatrix} \mathbf{K}_{NN} & \mathbf{K}_{NK} \\ \mathbf{K}_{KN} & \mathbf{K}_{KK} \end{bmatrix} \begin{Bmatrix} \mathbf{U}_N \\ \mathbf{U}_K \end{Bmatrix} = \begin{Bmatrix} \mathbf{0} \\ \mathbf{R} \end{Bmatrix}. \quad (1)$$

Here, N and K are indices representing nodes whose displacements are unknown (free nodes) and known (excited or constrained nodes), respectively. Hence, \mathbf{U}_N and \mathbf{U}_K are nodal displacement vectors for free and constrained vectors, respectively, while pair combinations of these indices relay the position of these nodes in respective property matrices \mathbf{M} (mass matrix) and \mathbf{K} (stiffness matrix). Additionally, \mathbf{R} is the vector of unknown reaction forces of nodes under excitation.

Modal analysis of an undamped oscillatory motion finds resonant frequencies by solving the following Eq. (2), where, ω is the angular frequency, while $\hat{\mathbf{U}}$ is the mode shapes vector.

$$(\mathbf{K} - \omega^2 \mathbf{M}) \hat{\mathbf{U}} = \{\mathbf{0}\}. \quad (2)$$

The modal analysis of the workpieces is performed employing the modal analysis module of ANSYS Workbench software. ANSYS Workbench suite uses Block Lanczos extraction method to obtain the vibration modes in prescribed frequency ranges.

Knowledge of appropriate frequencies of the workpieces allows application of a periodic forcing condition at the tailstock mount (Fig. 2). Transverse deformation amplitudes can be observed as a result, and the most suitable force value and frequency can be determined. In ANSYS Workbench, the harmonic response module can be used for this purpose.

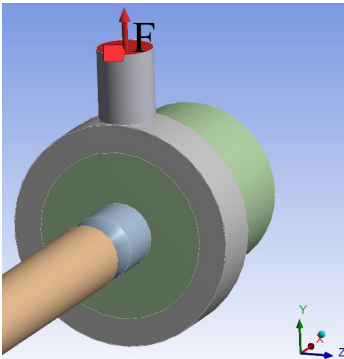


Fig. 2. Excitation force F application at the tailstock attachment

In the case of the two workpieces, both are constrained at the tailstock end and pre-stressed by the headstock. The mode search is performed between 15 kHz and 25 kHz; the resulting mode frequencies are then used to define the excitation of the workpiece at an arbitrary magnitude of 1 N.

The choice of the most suitable frequency has been simplified to fit the three criteria in descending order of importance: 1. neighbourhood of the frequency needs to be clear of other modes; 2. the average peak-to-peak, workpiece displacement value (an average of absolute values of oscillation amplitudes across the length of the workpiece) needs to be relatively high; 3. the mode frequency is in close proximity to similar mode frequencies in the other workpiece. To better illustrate the choice of the frequency, scatter plots are presented in Appendix B (Figs. B1 to 4). As a result, excitation frequencies at around 15.8 kHz have been chosen for both workpieces.

Carrying out a parametric sweep of the excitation force yields an average deformation amplitude of 1.5 μm at 2.1 N (Appendix C Figs. C1 and 2). Hence, the actuator will have to be able to be driven at 15.85 kHz and 15.794 kHz, and will need to produce a reaction force of 2.1 N at the fixture.

1.2 Development of the Ultrasonic Actuator

The initial design of the actuator is based on pre-existing dimensional and material requirements, as well as wavelength considerations. The actuator is to

be mounted on an M30 thread at the output end of the horn; thus, the variation of the output end diameter is limited (for safety, the wall thickness is chosen as 4 mm, resulting in minimum output end diameter of 38 mm). The piezoelectric stack consists of two piezo ceramic rings of dimensions 80 mm \times 30 mm \times 12 mm. This, in turn, defines the diameter of the input end of the horn and the backing mass to be 80 mm. For safe operation, the actuator is to be encased in a protective housing, which is mounted on an additionally formed flange, it is relatively light however and therefore will be neglected in further studies. To determine the lengths of the horn and the back mass, it is necessary to first define their materials.

A common guideline when choosing the material is to match the characteristic impedances of the piezo stack and front-back masses accordingly [9]:

$$z_c = \sqrt{z_f z_b}. \quad (3)$$

Here z_c , z_f , and z_b are characteristic impedances of centre stack, front mass and back mass respectively. After reviewing available material data and obtaining impedance values, a decision was made to manufacture the front mass from tool steel and back mass from an aluminium alloy. Bearing this in mind longitudinal dimensions of the actuator can be further considered.

The shape of the front mass is also an important factor in the transfer of ultrasonic energy to the output end of the actuator. Nad [10] and Nguyen and Wang [11] extensively researched the dynamic properties of different geometric shapes. However, since not much variation is allowed due to lateral dimension constraints, an exponential shape profile is considered, based on work by Al-Budairi [12].

The entire actuator is expected to oscillate at a half wave length; here, horn covers the first quarter of the wavelength, while the other quarter is in the centre stack and back mass. The wavelength for each material can be calculated using the following formula:

$$\lambda = \frac{c}{f}. \quad (4)$$

Here, c is the sound velocity in the medium, while f is the excitation frequency. The sound velocity can be determined accordingly:

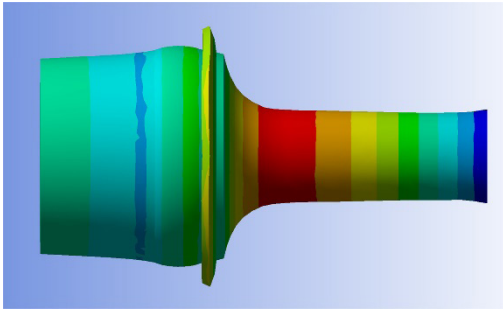
$$c = \sqrt{\frac{E}{\rho}}, \quad (5)$$

where E is Young's modulus, and ρ is the density of the material. Wavelength values can be found in Table 1.

Table 1. Material properties and physical dimensions

	Tool steel	PZT	Aluminium
Young's modulus [GPa]	170	73	78
Density [g cm ⁻³]	7.700	7.600	2.850
Sound velocity [m s ⁻¹]	4698.715	3099.236	5231.484
Wavelength [m]	0.297	0.196	0.330
Length [m]	0.074	0.025	0.041

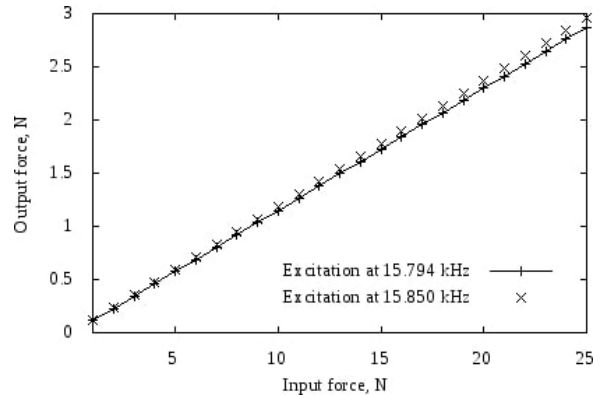
With all the data obtained, the derivation of front mass length is straight forward: one quarter of the wavelength for the tool steel. Since the value of the centre stack length was already known, it was determined to take up an eighth of its wavelength, making it possible to derive the back-mass value: an eighth of the wavelength for the aluminium alloy. These values were used in the initial design for modal analysis (Fig. 3). Here, a longitudinal mode was expected to occur at 15.794 kHz. However, mode search at 15 kHz to 25 kHz yielded frequency values 2 kHz above this value. A parametric sweep of the horn length was conducted and a longitudinal mode was observed at 15.939 kHz when the horn length was 111 mm.


Fig. 3. Longitudinal mode of the initial actuator design

The newly designed actuator was tested in a harmonic response study; here, both planar faces of the piezo stack were assigned arbitrary forces of the opposite sign, to simulate excitation from the piezo-stack. The force at the output end of the horn was measured, allowing the performance of a parametric sweep to determine the required input force, to produce 2.1 N at 15.794 kHz and 15.850 kHz on the output end, as required for excitation of the uniform cylinder and stepped shaft to 1.5 μm , respectively. The required input force was determined to be 19 N and 20 N for 15.794 kHz and 15.850 kHz cases respectively (Fig. 4).

Knowing the required force and velocity of vibration, allows determining the power requirements:

$$P = Fv \cos \varphi. \quad (6)$$


Fig. 4. Input-output force dependency for actuator at 15.794 kHz and 15.850 kHz

Here φ is considered to be the phase difference between the velocity and force. The obtained result shows the required power input of the transducer required to achieve force F during excitation. Since accelerations at the piezo-material to front-mass interface were determined to be 2070 mm/s² and 2000 mm/s² for 15.794 kHz and 15.850 kHz cases, respectively, peak velocities in both cases were found to be 20 mm/s. Assuming force and velocity to be in phase, Eq. (6) yields the following values:

$$P_{15.794} = Fv \cos \varphi = 19 \times 20 = 380 \text{ W},$$

$$P_{15.855} = Fv \cos \varphi = 20 \times 20 = 400 \text{ W}.$$

This demonstrates that the approach requires realistic power values and is theoretically feasible. Further investigations of the fully assembled system are necessary.

2 EXCITATION SYSTEM VERIFICATION

With working modes determined and the design of the actuator verified, a fully assembled system needs to be tested. Initial tests are performed using harmonic analysis in ANSYS workbench: here the displacement of the workpiece in the fully assembled system when the piezo stack is excited at the predetermined force and frequency is observed. Afterwards the excitation output is tested on a physical system. Lastly the effectiveness of the approach is tested by observing surface grinding results with and without operation of the actuator.

2.1 Harmonic Response of the Fully Assembled System

The harmonic analysis data for both workpiece configurations is presented in Table 2.

Table 2. Workpiece excitation parameters

Workpiece	Excitation force [N]	Frequency [kHz]
Uniform cylinder	20	15.850
Stepped shaft	19	15.794

The workpiece displacement graphs (Figs. 5 and 6) show a noticeable reduction in amplitude.

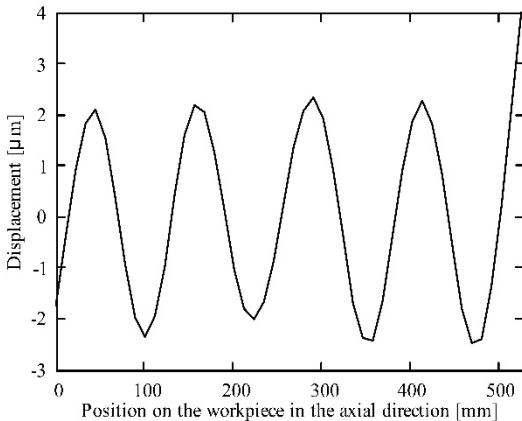


Fig. 5. Response of the uniform cylinder workpiece, being driven by 20 N at 15.85 kHz frequency, with the actuator attached

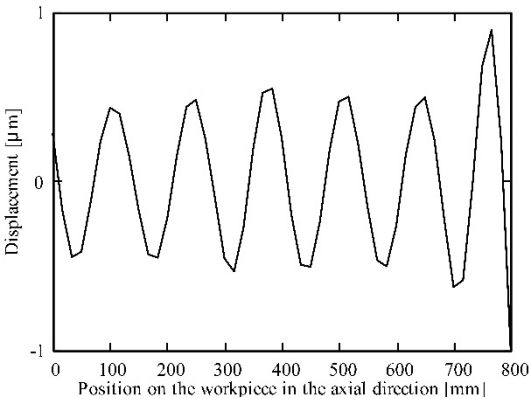


Fig. 6. Response of the stepped shaft workpiece, driven by 20 N at 15.794 kHz frequency with the actuator attached

Additional modal analysis of the entire assembly was performed, demonstrating that the addition of the actuator to the system shifted the transverse mode frequency to 17.349 kHz and 17.722 kHz for the uniform cylinder and stepped shaft workpieces, respectively (Figs. 7 and 8), which was the cause for the decrease in displacement.

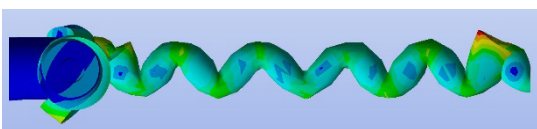


Fig. 7. Shifted transverse mode for uniform cylinder at 17.349 kHz

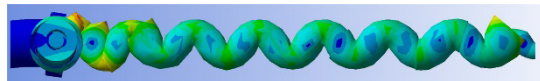


Fig. 8. Shifted transverse mode for stepped shaft at 17.722 kHz

Driving the systems at 17.349 kHz and 17.722 kHz yielded more appropriate responses in the order of micrometres (Figs. 9 and 10).

Similar changes are also expected to occur in the physical system; therefore, experimental vibration analysis is essential in this case.

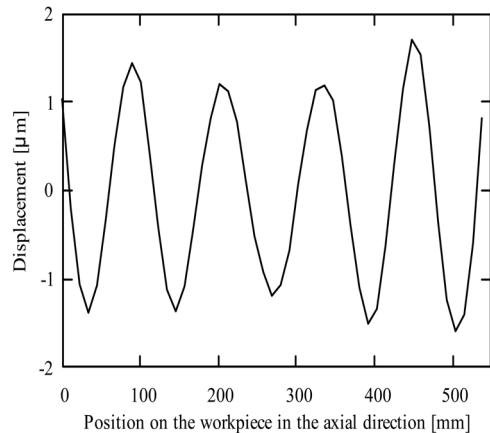


Fig. 9. Response of the uniform cylinder workpiece, driven by 19 N at 17.349 kHz frequency, with the actuator attached

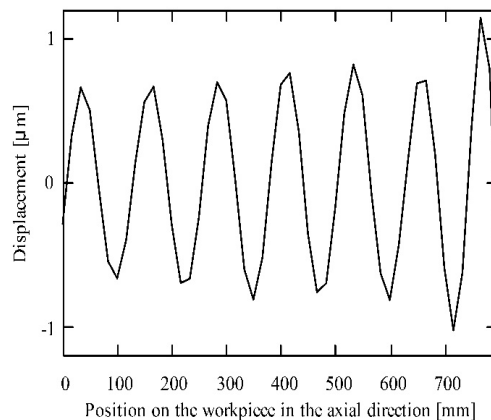


Fig. 10. Response of the stepped shaft workpiece, driven by 19 N at 17.722 kHz frequency with the actuator attached

2.2 Physical Excitation Measurements

The physical system consists of a Supertec G32D 100NC cylindrical grinding machine with the actuator mounted at the tailstock. The actuator is driven by a Sensotronica BT400 ultrasonic generator; from the tailstock, the oscillations are expected to be transferred to the workpiece at 17.349 kHz for a

uniform cylinder workpiece and 17.722 kHz for a stepped shaft workpiece.

For measurement, a PicoScope 3424 oscilloscope with a KD-91 accelerometer is used. With the ultrasonic generator at 40 % power, amplitudes of $0.368 \mu\text{m}$ were observed to occur at 16.818 kHz for both workpieces. The acceleration (Fig. 11) is in close proximity to the values obtained during simulation. This change corresponds with observations made in the previous sub-chapter, regarding the shift of mode frequency, due to the addition of the actuator. These conditions are to be further used in vibration assisted grinding (VAG) experiments.

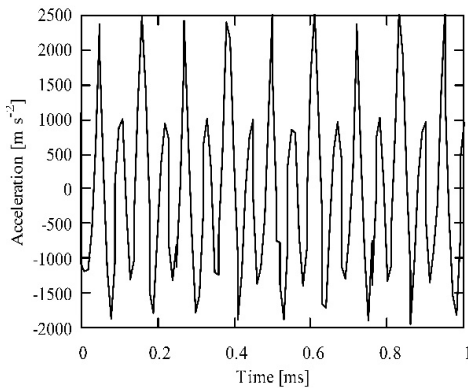


Fig. 11. Acceleration at 16.818 kHz

2.3 Experimental Vibration-Assisted Grinding Study

To test the effectiveness of the system, a grinding trial was conducted. After each grinding run, surface quality was measured using a Mitutoyo SurfTest SJ-210 surface roughness tester. Each measurement was performed 5 times, at sampling and cut-off lengths of 0.8 mm.

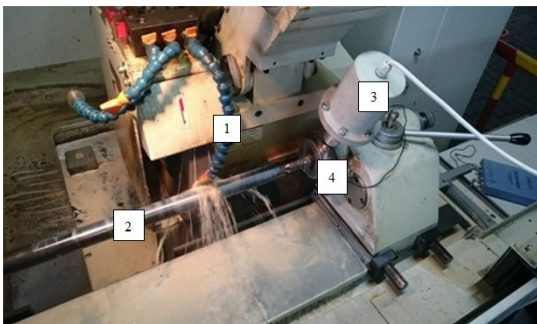


Fig. 12. Wet cylindrical grinding process : 1. Coolant nozzle; 2. Actuator; 3. Work-piece; 4. Bracket link

Experiments were carried out with and without vibrations for wet (Fig. 12) and dry grinding.

The settings of the machining parameters for the experiment are summarized in Table 3 and ultrasonically-assisted grinding zones are shown in Fig. 13.

The first experiment was carried out on a 1.1186 steel shaft using a conventional grinding method (without ultrasonic vibrations).

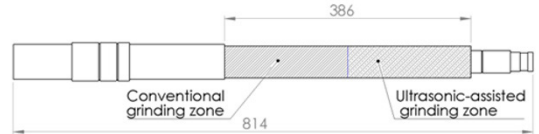


Fig. 13. Different grinding areas for stepped shaft workpiece

Table 3. Experimental set-up

Grinding wheel	Vitrified bond ZrA grinding wheel, grain size 80, 405/210/50
Workpiece 1 (stepped shaft)	1.1186 medium carbon steel, Vickers hardness 280 ($L=814 \text{ mm}$, $\varnothing=50 \text{ mm}$)
Workpiece 2 (uniform cylinder)	1.7225 42CrMo4, Vickers hardness 207 ($L=500 \text{ mm}$, $\varnothing=35 \text{ mm}$)
Grinding process	Dry/wet cylindrical grinding
Grinding conditions	Feed speed $v_f = 5 \text{ m min}^{-1}$; depth of cut $a_p = 0.01 \text{ mm}$; cutting speed $v_c = 34 \text{ m s}^{-1}$
Ultrasonic vibration conditions	Frequency $f = 16818 \text{ Hz}$; power $P = 40 \%$; amplitude $A = 0.386 \mu\text{m}$.

The second experiment was carried out on a 1.7225 steel bar. The grinding zones of the experiment are shown in Fig. 14.

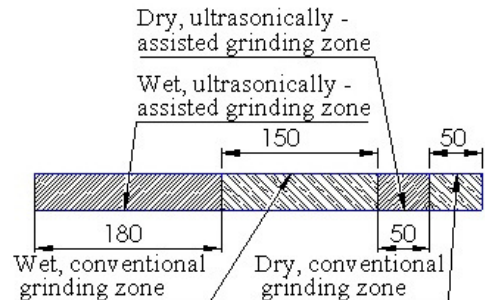


Fig. 14. Different grinding areas for uniform cylinder workpiece

After the experiments, the roughness of shaft and bar was measured with surface roughness tester at defined zones for conventional and ultrasonically-assisted grinding with and without cooling fluid. The results of surface roughness are summarized

in Table 4 and shown in Figs. 15 and 16. Here, UG and CG refer to wet grinding with ultrasound and without it, when applied to the stepped shaft, while UDG and CDG stand for ultrasonic and conventional dry grinding with UWG and CWG applied for wet grinding respectively, when dealing with the uniform steel bar.

Table 4. Surface roughness values

Roughness parameter [μm]	1.7225 steel bar				1.1186 shaft	
	Dry grinding		Wet grinding		Wet grinding	
	UG	CG	UG	CG	UG	CG
R_a	0.442	0.491	0.418	0.432	0.251	0.298
R_q	0.556	0.611	0.516	0.545	0.334	0.408
R_z	3.323	3.315	2.818	2.843	2.291	2.939

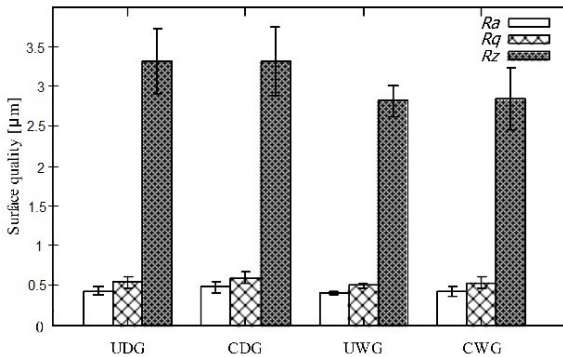


Fig. 15. Surface roughness values for grinding trials on a uniform cylinder workpiece

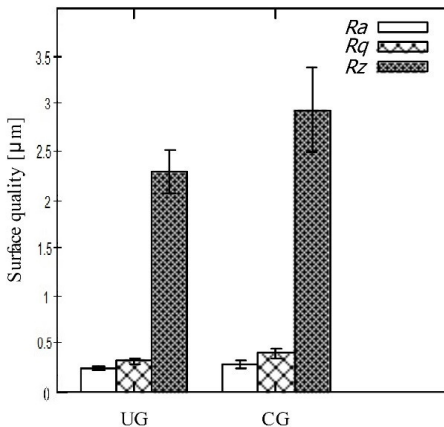


Fig. 16. Surface roughness values for grinding trials on a uniform stepped shaft workpiece

The results in the case of dry grinding are not much different between ultrasonic and conventional counterparts. Noticeable improvements were observed in ultrasonic wet grinding when compared to its conventional counterpart. This may suggest that

ultrasound enables a better lubrication mechanism, improving the surface quality as a result. However, more research needs to be conducted at different amplitudes, frequencies and machining parameters.

3 CONCLUSIONS

This research has concluded that the application of a high-powered oscillator to the stationary support of a rotating part is a viable approach to workpiece excitation in vibration-assisted machining. In the case of this research, based on FEM calculations, a generator of 400W with a transducer can produce workpiece amplitude of up to 1.5 μm .

Experimental investigations demonstrate the viability of the method in practice. However, the practical efficacy of the method is inconclusive, as the surface roughness test values show only a marginal improvement in the ultrasonically-assisted case.

To further contribute to this topic, upcoming research should investigate the dependence of surface roughness values on the excitation frequency and local amplitudes.

4 ACKNOWLEDGEMENTS

This work has been funded by EU Structural Funds project “High-level R&D” program: measure 01.2.2-LMT-K-718.

5 NOMENCLATURES

- A excitation amplitude [μm]
- c sound velocity [m s^{-1}]
- a_p cutting depth [mm]
- E Young’s modulus [GPa]
- F force [N]
- f frequency [kHz]
- K node index [-]
- \mathbf{K} stiffness matrix [N m^{-1}]
- λ wavelength [m]
- \mathbf{M} mass matrix [kg]
- N node index [-]
- P power [W]
- \mathbf{R} unknown reaction force vector [N]
- R_a roughness average [μm]
- R_q root mean square roughness [μm]
- R_z average maximum height of the profile [μm]
- ρ density [g cm^{-3}]
- \mathbf{U} nodal displacement vector [m]
- $\hat{\mathbf{U}}$ mode shape vector [-]
- v velocity [mm s^{-1}]
- v_c cutting speed [m s^{-1}]

- v_f feed speed [m min⁻¹]
 φ phase angle between force and velocity [degrees]
 z_c, z_f, z_b characteristic impedances [N s m⁻¹]
 ω angular frequency [degrees s⁻¹]

8 REFERENCES

- [1] Lauwers, B. (2011). Surface integrity in hybrid machining processes. *Procedia Engineering*, vol. 19, p. 241-251, DOI:10.1016/j.proeng.2011.11.107.
- [2] Schuh, G., Kreysa, J., Oriiski, S. (2009). Roadmap "Hybride Produktion". *Zeitschrift für Wirtschaftlichen Fabrikbetrieb*, vol. 104, no. 5, p. 385-391, DOI:10.3139/104.110072.
- [3] Graževičiūtė, J., Skiedraitė, I., Ostaševičius, V., Jurėnas, V., Bubulis, A. (2006). Ultrasound application in turning process. *Proceedings of 6th International Conference Vibroengineering*, p. 152-154.
- [4] Ostaševičius, V., Gaidys, R., Daukševičius, R., Mikuckytė, S. (2013). Study of vibration milling for improving surface finish of difficult-to-cut materials. *Strojniški vestnik - Journal of Mechanical Engineering*, vol. 59, no. 6, p. 351-357, DOI:10.5545/sv-jme.2012.856.
- [5] Tawakoli, T., Azarhoushang, B. (2008). Influence of ultrasonic vibrations on dry grinding of soft steel. *International Journal of Machine Tools and Manufacture*, vol. 48, no. 14, p. 1585-1591, DOI:10.1016/j.ijmactools.2008.05.010.
- [6] Choi, Y., Park, K., Hong, Y., Kim, K., Lee, S., Choi, H. (2008). Effect of ultrasonic vibration in grinding; horn design and experiment. *International Journal of Precision Engineering and Manufacturing*, vol. 14, no. 11, p. 1873-1879, DOI:10.1007/s12541-013-0253-1.
- [7] Kuo, K. (2009). Ultrasonic vibrating system design and tool analysis. *Transactions of Nonferrous Metals Society of China*, vol. 19, suppl. 1, p. s225-s231, DOI:10.1016/S1003-6326(10)60275-0.
- [8] Liang, Z., Wu, Y., Wang, X., Zhao, W. (2010). A new two-dimensional ultrasonic assisted grinding (2D-UAG) method and its fundamental performance in monocrystal silicon machining. *International Journal of Machine Tools & Manufacture*, vol. 50, no. 8, p. 728-736, DOI:10.1016/j.ijmactools.2010.04.005.
- [9] Abdullah, A., Shahini, M., Pak, A. (2009). An approach to design a high power piezoelectric ultrasonic transducer. *Journal of Electroceramics*, vol. 22, no. 4, p. 369-382, DOI:10.1007/s10832-007-9408-8.
- [10] Nad, M. (2010). Ultrasonic horn design for ultrasonic machining technologies. *Applied and Computational Mechanics*, vol. 4, no. 1, p. 79-88.
- [11] Nguyen, H., Wang, D. (2012). Design of an ultrasonic steel horn with a Bézier profile. *International Conference on Green Technology and Sustainable Development*, p. 1-9.
- [12] Al-Budairi, H.D. (2012). *Design and analysis of ultrasonic horns operating in longitudinal and torsional vibration*. PhD thesis, University of Glasgow, Glasgow.

9 APPENDICES

9.1 Appendix A

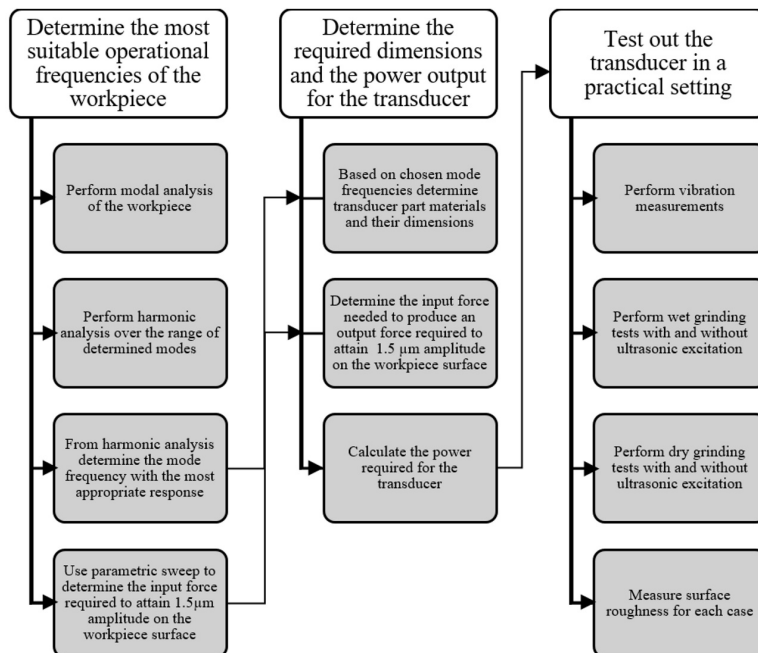


Fig. A1. Research process diagram

9.2 Appendix B

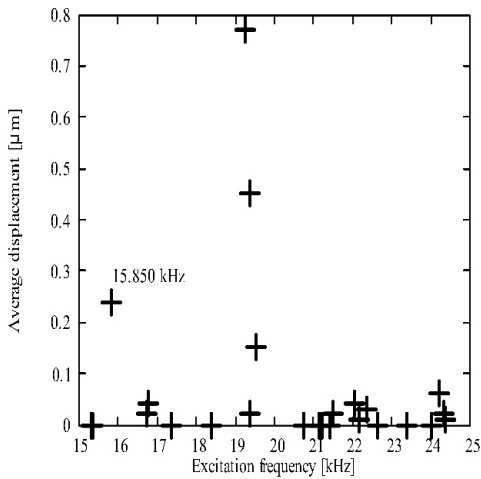


Fig. B1. Average displacement distribution based on excitation frequency (Y axis - uniform cylinder)

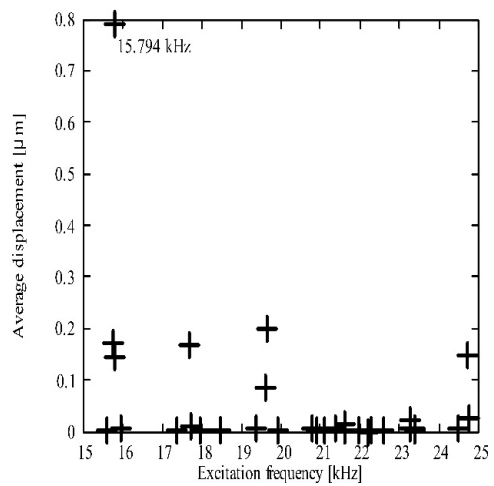


Fig. B3. Average displacement distribution based on excitation frequency (Y axis - stepped shaft)

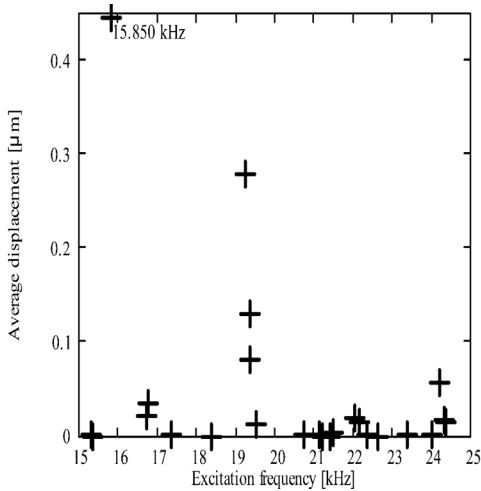


Fig. B2. Average displacement distribution based on excitation frequency (Z axis - uniform cylinder)

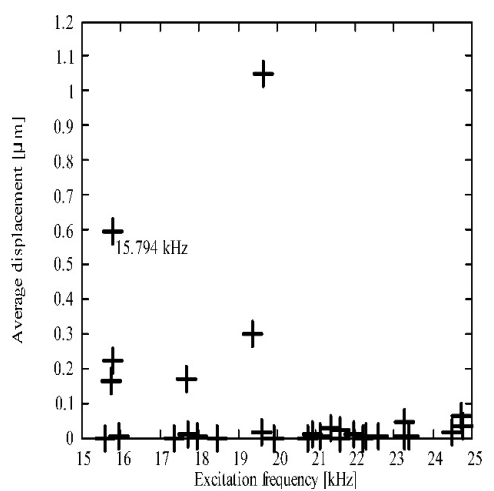


Fig. B4. Average displacement distribution based on excitation frequency (Z axis - stepped shaft)

9.3 Appendix C

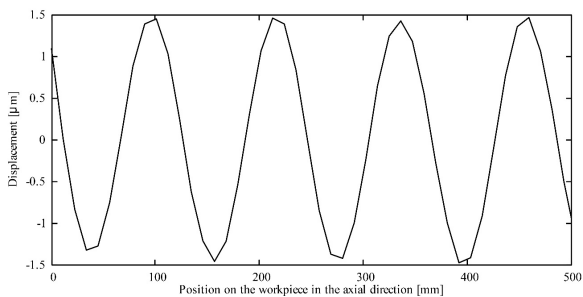


Fig. C1. Response of the uniform cylinder workpiece, driven by 2.1 N at 15.85 kHz frequency

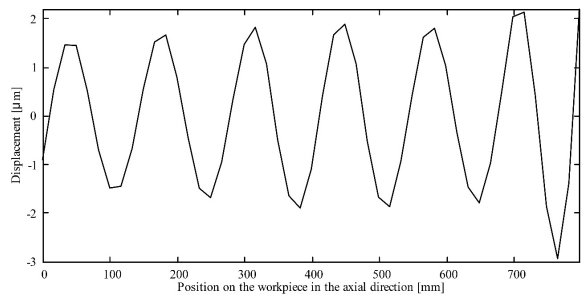


Fig. C2. Response of the stepped shaft workpiece, driven by 2.1 N at 15.794 kHz frequency

Fabrication of High Chromium White Iron Surface Layers on Ductile Cast Iron Substrate by Laser Surface Alloying

Damian Janicki*

Silesian University of Technology, Faculty of Mechanical Engineering, Poland

High chromium white iron surface layers (HWSLs) have been produced on a ductile cast iron EN-GJS-700-2 substrate by diode laser surface alloying with a direct injection of a pure chromium powder into the molten pool. The main objective of this study was to investigate the effect of laser alloying parameters on the microstructural evolution in the HWSLs. The composition of the uniformly alloyed HWSLs contained up to 14.4 wt.% Cr. Both hypoeutectic and eutectic high chromium white iron microstructures were obtained. The type and morphology of eutectic carbides are affected by both the chromium concentration in the molten pool and the solidification conditions. With increasing chromium content, the fraction of eutectic regions in the hypoeutectic HWSLs increases and the eutectic carbides become progressively smaller. The rod-type morphology of the M_7C_3 eutectic carbides was dominant in the eutectic HWSLs. An average hardness of the HWSLs was influenced by the size of carbide precipitations, and was 675 HV and 650 HV for hypoeutectic and eutectic compositions, respectively.

Keywords: high chromium white iron, ductile cast iron, surface alloying, diode laser

Highlights

- The hypoeutectic and eutectic HWSLs were produced on a ductile cast iron EN-GJS-700-2 substrate by diode laser surface alloying with a pure chromium powder.
- The composition of the uniformly alloyed HWSL contained up to 14.4 wt.% Cr.
- The type and morphology of eutectic carbides are influenced by both the chromium concentration in the molten pool and the solidification conditions.
- The size of eutectic carbides has a direct impact on the overall hardness of the HWSL.
- The rod-type morphology of the M_7C_3 eutectic carbides was dominant in the eutectic HWSLs.

0 INTRODUCTION

Ductile cast irons (DCIs) are finding use in a growing range of applications due to a beneficial combination of their properties, such as high ductility and toughness, good fatigue strength, excellent machinability, and the ability to be cast into complex shapes [1]. However, DCIs are simultaneously characterized by low abrasion and erosion resistance [2]. Because of this, their use under severe wear conditions is generally limited. Currently, much emphasis has been placed on the improvement of wear performances of the working surface of machine parts made of the DCIs. Most published works have been focused on surface modification methods with the use of fusion welding technologies, such as surface melting [3] and surface alloying processes [4]. Due to the ability to change a chemical composition of modified surface layers, the surface alloying process is an especially promising method to tailor surface properties of cast irons. An ideal source of heat for the above-mentioned surface treatment process is the laser beam having a uniform intensity distribution (a top-hat profile) [5] to [7].

In contrast, it is well known that high chromium white irons (HWIs) have excellent abrasive and erosive wear resistance [8]. Their exceptional wear

performances result from a high-volume fraction of hard proeutectic and/or eutectic M_7C_3 carbides and a tough matrix [9]. Several researchers have reported the formation of such composite structures during the surface alloying of different types of cast irons [10] to [11]. However, little work has been done to investigate the formation of HWI surface layers on DCIs using laser-alloying systems that utilize both laser sources with the top-hat beam profile and a direct injection of an alloying powder into the molten pool.

Therefore, the aim of the present work has been to explore the potential of a laser-alloying system comprising a high power direct diode (HPDD) laser with the top-hat beam profile and a direct injection of an alloying powder into the molten pool for the fabrication of HWI surface layers on the DCI substrate.

1 EXPERIMENTAL PROCEDURE

1.1 Materials

The substrate material (SM) used in this study was a DCI grade EN-GJS-700-2 with chemical composition shown in Table 1. The microstructure of the as-received DCI consists of a perlitic/ferritic matrix and

*Corr. Author's Address: Silesian University of Technology, Faculty of Mechanical Engineering, Konarskiego 18A, Gliwice, Poland, damian.janicki@polsl.pl

graphite spheres with an average diameter of 30 μm (Fig. 1). Specimens of the SM were in the form of discs 60 mm in diameter and 10 mm thick. Prior to the alloying process, the specimens were ground to a surface finish of 0.5 μm R_a and cleaned with acetone. A chromium powder used as the alloying material has a purity of 99.8 % and a particle size range of 40 μm to 90 μm .

Table 1. Chemical composition of the used DCI grade EN-GJS-700-2 (wt.%)

C	Si	Cu	Mn	Cr
3.60	2.51	0.78	0.25	0.02
Ni	S	P	Fe	
0.04	0.008	0.016	balance	

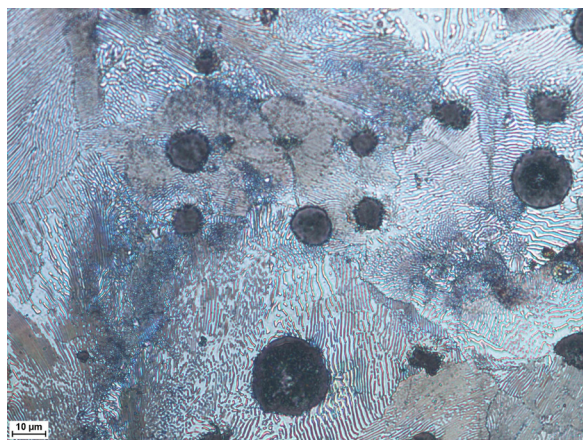


Fig. 1. Microstructure of the used DCI grade EN-GJS-700-2

1.2 Laser processing

A continuous wave Rofin DL020 HPDD laser with a rectangular beam spot of size 1.5 mm \times 6.6 mm and a uniform intensity distribution profile (the top-hat profile) was used for single-pass and multi-pass overlapping alloying trials. The beam profile of the used laser, measured with a Promotec Laserscope UFF100, is presented in Fig. 2. All alloying trials were performed in the fast-axis direction using a direct injection of the alloying powder into the molten pool via an off-axis powder injection nozzle. To provide a uniform powder distribution on the surface of the molten pool, the powder injection nozzle shape has been adopted to the laser beam spot (Fig. 3). The powder delivery system used had a feed rate accuracy of $\pm 0.5\%$. Argon was used as a shielding gas and was injected through a cylindrical nozzle at a flow rate of 8 l/min (coaxially with the powder stream).

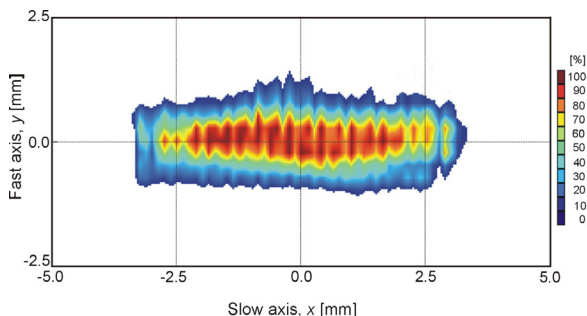


Fig. 2. 2D beam profile of the used HPDD laser in the focal plane

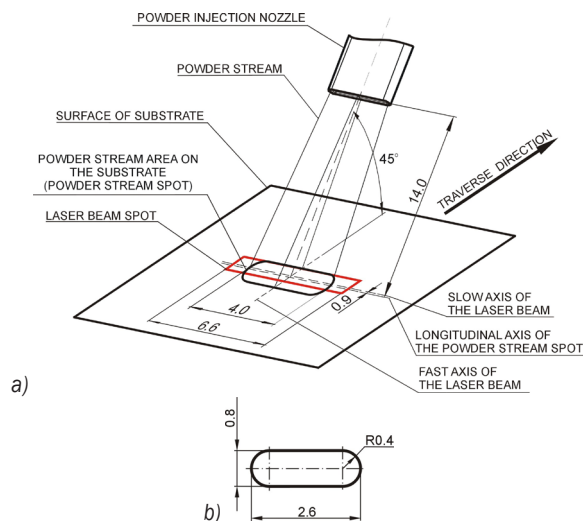


Fig. 3. Diagram showing a) the alignment of the powder injection nozzle relative to the laser beam spot, and b) the geometry of the powder injection nozzle opening used

To investigate the impact of processing conditions on the composition, microstructure, and hardness of the HWI surface layers, the experiments were divided into two stages. The first stage was focused on the determination of the maximum chromium powder feed rate (MCP) for a given heat input (HI) level (defined by the ratio of the laser power and the traverse speed). The MCP was determined as the powder feed rate providing a uniform concentration of Cr in the fusion zone (FZ). In this stage, a series of single-pass alloyed beads (SBs) were made at several laser power levels, in the range of 1200 W to 1600 W, with traverse speeds varying from 1.66 mm/s and 3.33 mm/s. The powder feed rate, which is defined in this study as the amount of chromium powder provided per unit length of the SB, was in the range of 1.5 mg/mm to 12 mg/mm, Table 2. The second stage of experiments included a fabrication of high chromium white iron surface layers (HWSLs) via a multi-pass overlapping alloying process using optimal processing conditions (Table 3). This stage provided an understanding of the

effect of Cr concentration and solidification conditions in the molten pool on the microstructural evolution of the alloyed layers. All alloying trials were carried out without substrate preheating.

1.3 Metallographic Examination

Geometrical parameters of the SBs and multi-pass overlapping alloying layers were measured using an optical microscope and a Nikon NIS-Elements quantitative image analysis system. Microstructural analysis was performed using both an optical and a scanning electron microscope (SEM) equipped with an energy dispersive X-ray spectrometer (EDS). The fraction of eutectic regions in the microstructure of the HWSLs was measured using Carl Zeiss digital image processing software. The measurements were conducted on SEM images taken from the undersurface and mid-section of the alloyed layer, over a total area of the 8 mm² for each layer. The phase composition was determined by the X-ray diffraction (XRD) technique. Diffraction patterns were recorded using Co-K_α radiation ($\lambda=0.179$ nm).

1.4 Hardness Testing

The HWSLs' hardness was measured on polished cross sections with Vickers micro-indentation load of 200 g using Wilson Wolpert 401 MVD Vickers.

2 RESULTS AND DISCUSSION

2.1 Macro and Micro Analysis

Fig. 4 shows cross-sectional macrographs of the SBs produced at a laser power of 1200 W, traverse speed of 3.33 mm/s (HI of 360 J/mm) and two levels of powder feed rate. The cross-sectional fusion profiles suggest that the molten pool had a negative surface tension temperature coefficient, meaning that the surface tension was greatest at the edges of the molten pool and lowest in the centre. In this case, the surface tension gradient induces fluid flow outward along the surface of the molten pool, producing the wide and shallow FZ. This shape of the FZ enables reducing overlap ratios during a multi-pass overlapping alloying process, limiting the overall HI. Moreover, it is important to note that the EDS line-scan analysis collected on cross-sections of the SBs has shown that the above-mentioned character of the fluid flow in the molten pool provides a homogeneous Cr distribution throughout the FZ even at relatively high powder feed rates (Fig. 5a).

It is clear that the MCP increases with an increase in the HI levels (Fig. 6). However, the data listed in Table 2 imply that the increase in the MCP does not provide a significant change in the Cr content in the SBs. This follows from the fact that the increase in the HI level leads simultaneously to progressively

Table 2. Selected processing parameters of the HPDD laser surface alloying process and geometrical parameters of the FZ of the SB and a total Cr content in the SB

Processing condition no./ SB no.	Laser power [W]	Traverse speed [mm/s]	Heat input [J/mm]	Powder feed rate [mg/mm]	Cross-sectional bead geometry		Quality	Cr content [wt.%]
					Fusion zone depth, <i>f</i> [mm]	Fusion area of the bead, <i>A</i> [mm ²]		
C1	1200	3.33	360	1.5	0.70	3.2	Uniform	3.9
C2				4.5	0.69	3.3	Uniform	8.7
C3				5.5	0.70	3.4	Uniform	11.4
C4		1.67	720	6.0	0.72	3.6	Non-uniform	-
C5				5.5	0.88	4.2	Uniform	11.0
C6				7.5	0.93	4.4	Uniform	12.1
C7	1400	3.33	420	6.0	0.77	4.0	Uniform	11.8
C8		1.67	840	8.0	0.99	5.0	Uniform	12.2
C9			1600	960	9.0	1.09	6.6	Uniform

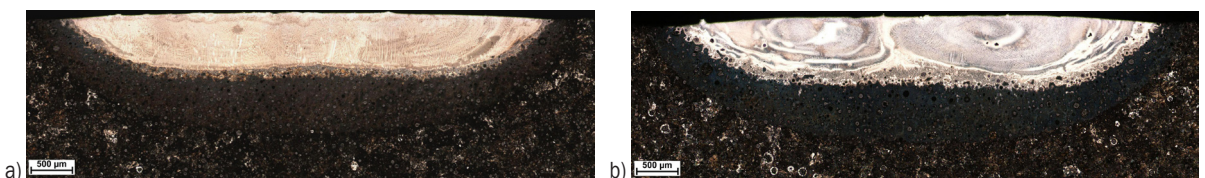


Fig. 4. Macrographs of the SBs no.: a) C3; b) C4

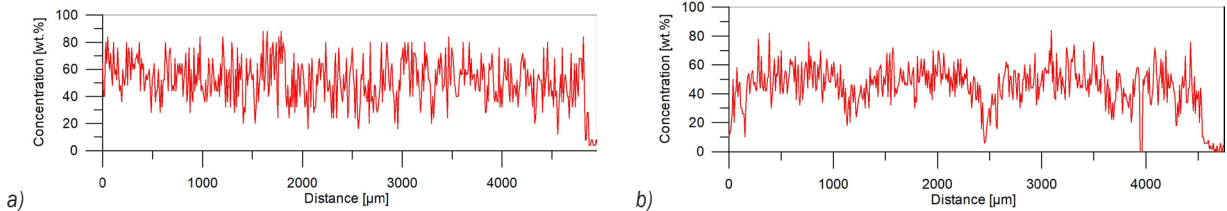


Fig. 5. Chromium concentration profiles on the cross-section of the SB no.: a) C3; b) C4. Results from SEM/EDS line-scans analysis collected along line parallel to the bead surfaces at 350 μm depth

higher fusion areas of the SB (Table 2). As a result, the maximum amount of Cr which can be introduced into the molten pool during fabrication of the uniformly alloyed SB, in the used range of the HI, was found to be approx. 14.4 wt.%. The increase of powder feed rate above the MCP for the given HI level led to a non-uniform composition (Fig. 5b) and microstructure in the SB as a consequence of incomplete mixing in the molten pool (including an incomplete dissolution of graphite nodules, Fig. 7). The chromium powder capture efficiency, which in the laser-allying process with an off-axis powder injection system depends directly on the size of the molten pool, was estimated to be in the range of 40 % to 50 %. Typical dimensions of the uniformly alloyed SB were width of approx. 6 mm and fusion depth in the range of 0.7 mm to 1.09 mm.

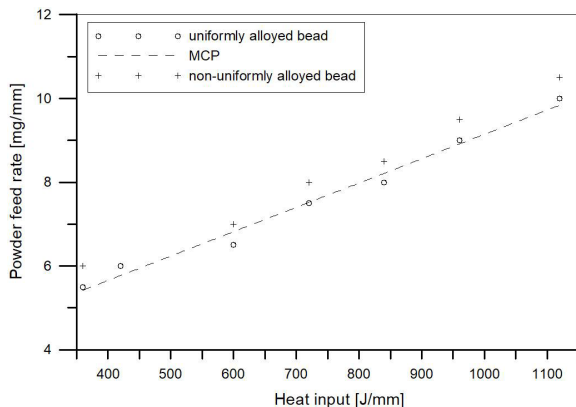


Fig. 6. Effect of the HI level on the MCP

The typical cross-sectional macrograph of the HWSL produced at the HI level of 720 J/mm and the powder feed rate of 5.5 mg/min (HWSL no. H4, Table 3) is presented in Fig. 8. The microstructural parameters of the selected HWSLs produced at the optimal range of processing parameters are summarized in Table 3. As a result of the specific FZ geometry of the SB (wide and shallow), the uniform thickness of the HWSL was achieved at a low overlap

ratio of 30 %. The thickness of the fabricated HWSLs, which directly depends on the used HI level, was in the range of 0.7 mm to 1.1 mm. Generally, the HWSLs produced in the optimal range of processing parameters have uniform microstructures and no porosity. Due to the leak of preheating, all HWSLs possessed a crack network. The cracks propagated perpendicularly to the fusion boundary (FB) and did not affect the structural integrity of the alloyed layers. The cracking propensity of the HWSLs was found to decrease with increasing Cr content.



Fig. 7. Low magnification SEM image showing the non-uniformity in the microstructure on the cross-section of the SB no. C4



Fig. 8. Macrograph of the HWSL no. H4

The metallographic data, presented in Table 3, indicate that the HWSLs having up to 12 wt.% Cr contents exhibited the hypo-eutectic microstructure (Figs. 11a to d). Higher Cr contents in the molten

pool led to a formation the eutectic microstructure (Fig. 11e). A low magnification cross-sectional SEM micrograph of the hypo-eutectic HWSL no. H3 is presented in Fig. 9. Fig. 10 shows the EDS line-scan analysis of Cr concentration across the FZ (depth profile) of the above-motioned HWSL. The FZ can be divided into two layers: a layer with constant Cr content and a very thin layer directly adjacent to the FB exhibiting a gradient distribution of chromium. The thickness of the layer with the gradient Cr distribution decreases with the increase in the HI level and ranged from about 150 μm to 20 μm . The microstructure of this layer is composed of primary austenite (γ_p) grains partially transformed into martensite and a network of the ledeburite distributed between the γ_p grains. Graphite nodules surrounded by ledeburite shells are also present in this layer. Cross-sectional SEM micrographs taken from the mid-section of the selected HWSLs, produced in the range of optimal processing parameters (Table 3), are shown in Fig. 11. In general, the hypo-eutectic microstructure of the HWSLs contains primary γ_p dendrites and eutectic regions composed of eutectic carbides (M_3C or M_7C_3 depending upon the chromium content) and the eutectic austenite phase (γ_e). Non-equilibrium cooling conditions in the molten pool and a chromium addition suppress the martensitic transformation [12] and [13]. In consequence, martensite needles were not observed in the γ_p dendrites. However, as can be seen in Figs. 11a and d the eutectic austenite phase in the HWSLs with low chromium contents (~ 4.0 wt.%) or produced at low solidification rates are partially transformed into martensite. The γ_p dendrite growth generally occurs at a faster rate in the direction perpendicular to the FB. This is because the SM (solid) acts as a heat sink. As a result, during solidification in the molten pool, cooling mostly occurs via the substrate, which brings about the directional growth of the γ_p dendrites counter to the heat flow direction (Fig. 9). An increase of the traverse speed, at constant powder feed rate, leads to a refinement of the γ_p dendrites. An average spacing between secondary dendrite arms varied from

2.5 μm to 1.6 μm , at traverse speeds of 1.67 mm/s and 3.33 mm/s, respectively (processing conditions no. C3 and C5, respectively, Table 2).

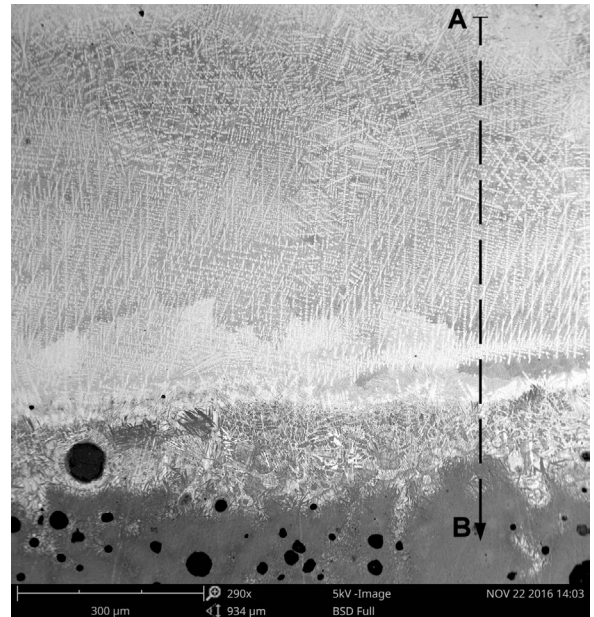


Fig. 9. Low magnification SEM image of the microstructure of the hypo-eutectic HWSL no. H3

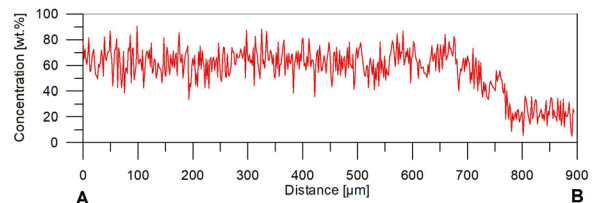


Fig. 10. Chromium concentration profile on the cross-section of HWSL no. H3; profile taken along the line marked in Fig. 9

The type and morphology of eutectic carbides in the hypo-eutectic HWSLs depend both on the Cr concentration in the molten pool and on solidification conditions. In the HWSL with Cr content of about 4.0 wt.% (no. H1, Table 3), only the eutectic carbides of the M_3C type was present. In turn, when the Cr

Table 3. Processing parameters of the multi-pass overlapping alloying process and the HWSLs' microstructural characteristics

HWSL no.	Processing condition no. (Table 3)*	Structure of the HWSL	Cr content in the HWSL [wt.%]			Type of eutectic carbide	Fraction of eutectic region [vol.%]
			Dendrite cores	Eutectic regions	Total		
H1	C1	hypo-eutectic	1.9	3.5	4.1	M_3C	54.5 ± 2.9
H2	C2	hypo-eutectic	5.4	10.3	9.2	$\text{M}_3\text{C} + \text{M}_7\text{C}_3$	66.6 ± 2.4
H3	C3	hypo-eutectic	7.7	13.5	11.6	M_7C_3	72.5 ± 2.5
H4	C5	hypo-eutectic	6.0	13.9	11.4	M_7C_3	78.6 ± 3.5
H5	C8	eutectic	-	-	12.6	M_7C_3	~ 100

Remarks: *overlap ratio: 30 %.

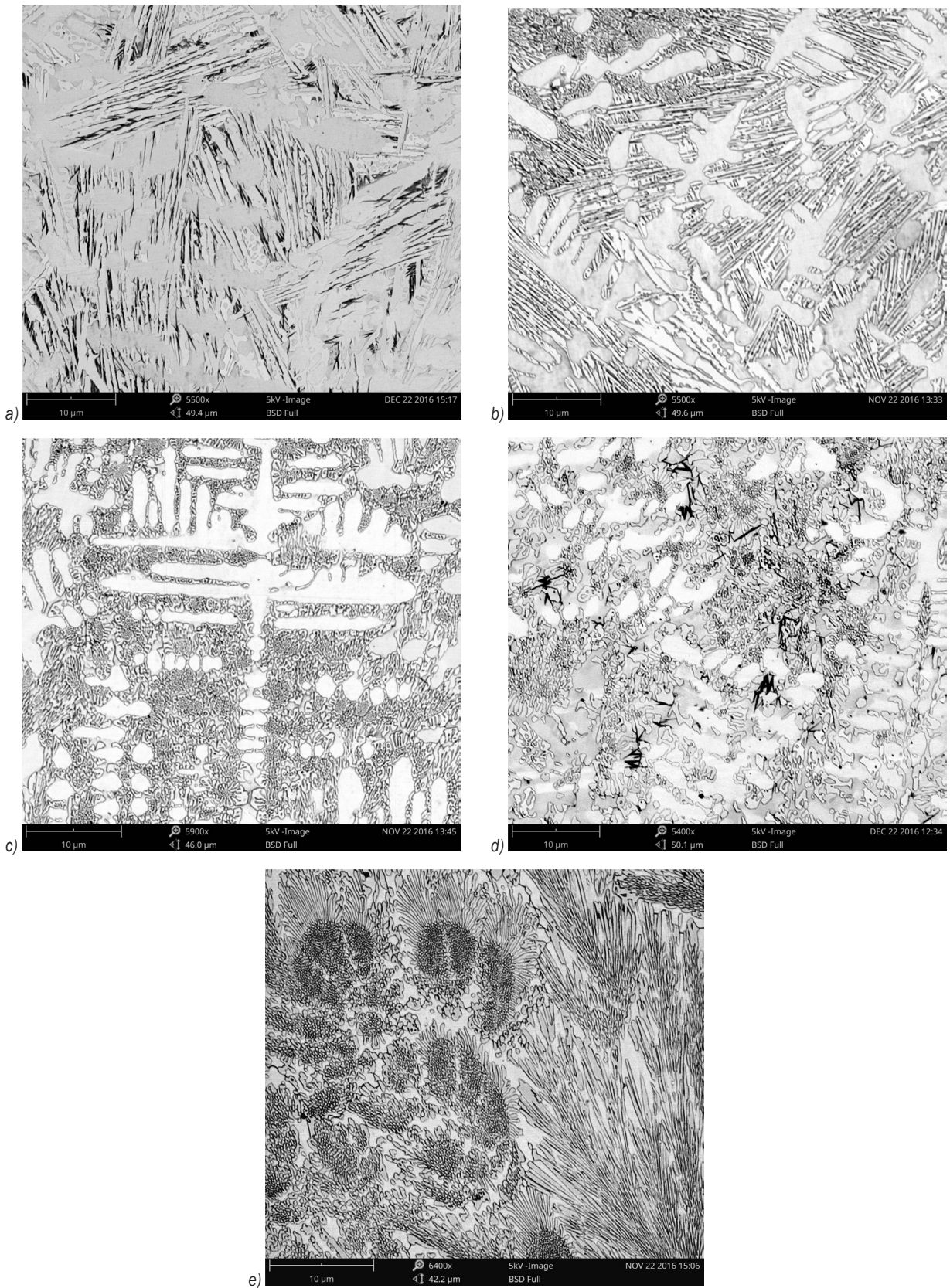


Fig. 11. SEM micrographs taken from the mid-section of the HWSL no.: a) H1; b) H2; c) H3; d) H4; e) H5

content was higher than about 10 wt.%, the eutectic regions were composed completely of $\gamma_e + M_7C_3$. Representative XRD patterns for the HWSLs exhibiting the above-mentioned two modes of solidifications (HWSLs no. H1 and H3) are depicted in Figs. 12a and b, respectively. The XRD pattern for the HWSL no. H1 gave peaks which can be identified as belonging to the following: γ -Fe (fcc) phase, M_7C_3 ($M = Cr, Fe$) and α -Fe (bcc) phase. The α -Fe (bcc) peaks suggest the partial austenite to martensite transformation. In contrast, the XRD analysis of the HWSL no. H3 confirmed the presence of γ -Fe (fcc) phase and M_7C_3 ($M = Cr, Fe$) carbides.

As expected, the volume fraction of the eutectic regions increases with increased total Cr content. Additionally, the data presented in Table 3 imply that the volume fraction of the eutectic regions, at constant Cr content, is affected by the traverse speed and HI level, that determine solidification conditions in the molten pool. Quantitative analysis of micrographs of the HWSLs no. H3 and H4, that is, having similar Cr contents (~ 11.5 wt.%), indicated that the increase in the traverse speed from 1.67 mm/s to 3.33 mm/s resulted in the reduction of the total fraction of the eutectic regions from approx. 78.6 vol.% to 72.5 vol.%, respectively. Taking into account that the above-mentioned change in the traverse speed simultaneously led to the decrease in the HI level, it can be considered that the fraction of the eutectic carbides increases with a decrease of solidification and cooling rates, as a consequence of the change in the microsegregation. This is consistent with SEM/EDS analysis which revealed that the γ_p dendrites become depleted in chromium with the decrease in solidification and cooling rates (Table 3). The total fraction of the eutectic regions in the HWSL with the lowest Cr content (~ 4.0 wt.% Cr) was measured to be approx. 54.5 vol.%. This implies that in all hypo-eutectic HWSLs the eutectic regions formed a continuous network surrounding the γ_p dendrites.

Generally, the $\gamma_e + M_3C$ eutectic has the ledeburite structure (Fig. 11a). The increase in the Cr content leads to the refinement of the M_3C plates (Fig. 11b). The M_7C_3 carbides exhibit both the rod-type and blade-type morphologies (Fig. 11c). As in the case of M_3C carbides, with increasing Cr content the M_7C_3 precipitations become progressively smaller. Additionally, as can be seen in Figs. 11c and d, at constant Cr concentration in the molten pool, lower cooling and solidification rates promote a coarsening of M_7C_3 carbides. Since the eutectic carbides in the hypo-eutectic HWSLs grow around the pre-existing γ_p dendrites, their growth directions are affected by these dendrites. As a result, the orientation of the eutectic carbides varies with the heat-flow direction.

The eutectic HWSL (no. H5, Table 3) shows the eutectic microstructure ($\gamma_e + M_7C_3$) throughout the entire layer with constant Cr content (Fig. 13). In this microstructure, the M_7C_3 type eutectic carbides grow as eutectic colonies (Fig. 11e). The M_7C_3 carbides within the eutectic colony are fine rod-like (fibrous) at the centre region of the colony and become slightly coarser and blade-like at the edge of the colony (Fig. 14). Simultaneously, with increasing distance from the centre of the colony, the volume fraction of the carbides decreases. This morphology of the eutectic colony indicates that the solidification begins in the centre with a certain level of undercooling and proceeds radially outward. The progress of solidification leads to a drop in the undercooling and, consequently, to the formation of coarser carbides in the last stage of the eutectic colony growth process. An average diameter of the carbide rod at the centre of the eutectic colony was approx. 180 nm. The diameter of the eutectic colony varied within the range from 4 μm to 10 μm . Based on the quantitative analysis of micrographs of the HWSL no. H5, the volume fraction of the carbides in eutectic colonies was estimated to be approx. 52 ± 4.5 %.

An optical micrograph showing the FB region in HWSLs is presented in Fig. 15a. In general, the

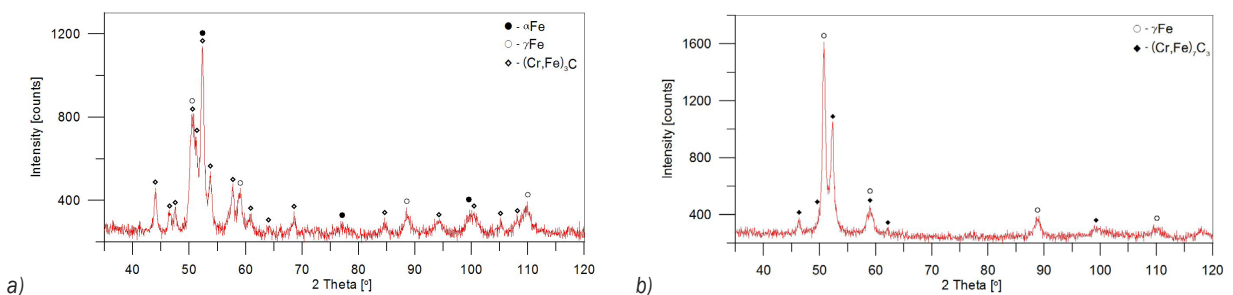


Fig. 12. XRD patterns of the HWSLs no.: a) H1; b) H3

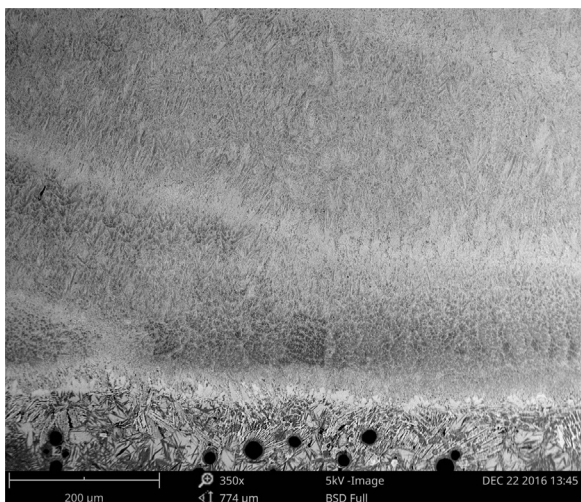
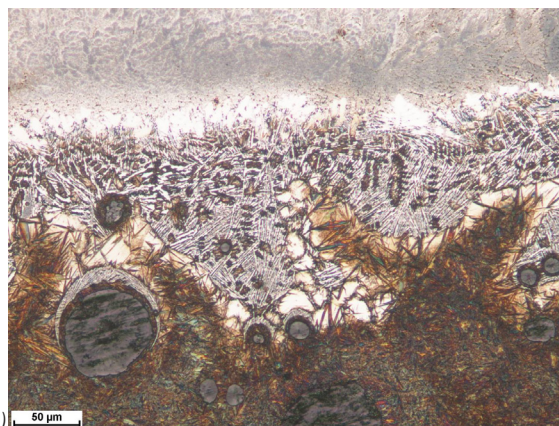


Fig. 13. Low magnification SEM image of the microstructure of the eutectic HWSL no. H5

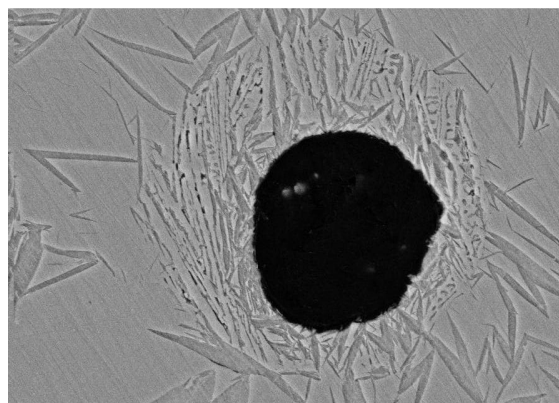


Fig. 14. SEM image of the deep-etched HWSL no. H5 showing morphology of eutectic colonies

heat-affected zone (HAZ) of the HWSLs comprises of three sub-regions: a thin layer containing high amounts of retained austenite directly adjacent to the fusion line (AZ), the partial fusion zone (PFZ) and the solid-state transformation zone (SZ). The microstructure of AZ region contains large retained austenite grains with a small amount of martensite needles. The width of this zone was approx. 20 μm . The presence of the PFZ region is a consequence of a significant elemental segregation and a broad solidification temperature range of the DCI [14]. These two factors result in a development of regions containing the carbide eutectic structure (ledeburite). The ledeburite regions mainly occupy the periphery of graphite nodules where carbon diffuses into the matrix lowering the solidus and liquidus temperatures



a)



b)

Fig. 15. a) An optical micrograph of the FB region in HWSLs no. H5, and b) SEM image showing the ledeburite-martensite shell around the graphite nodule in the PFZ of the HAZ

of austenite, and forming liquid pools. The subsequent rapid cooling of these liquid pools leads to the formation of ledeburite-martensite shells around the graphite nodules. As can be seen from Fig. 15b, a thin martensite layer is directly adjacent to the graphite nodule. The occurrence of such double shells around graphite nodules has already been documented in the literature [15], and it appears to be associated with a slower cooling rate in the direct vicinity of the surface of the graphite nodule than in the region further away from the graphite. The matrix microstructure of the SZ is composed mainly of martensite and residual austenite. The total width of the HAZ is dependent upon the HI level, and ranged from about 0.8 mm for HI of 360 J/mm to 1.3 mm for HI of 960 J/mm.

2.2 Microhardness Analysis

Microhardness profiles of the cross-section of the HWSLs with different Cr contents are compared in

Fig. 16. Generally, the microhardness data indicate that the size of eutectic carbides has a direct impact on the overall hardness of the HWSL. Note that the average hardness values for the hypo-eutectic HWSLs no. H1 and no. H3, that is with the eutectic regions composed of $\gamma_e + M_3C$ and $\gamma_e + M_7C_3$, respectively, are similar. In the above-mentioned cases, the average hardness was approx. 673 HV and 677 HV, respectively. In contrast, it is well known that M_7C_3 carbides are significantly harder than M_3C carbides (hardness ranges of M_3C and M_7C_3 are 1060 HV to 1230 HV and 1500 HV to 1800 HV, respectively [16]). Additionally, the volume fraction of eutectic regions in the HWSL no. H3 is significantly higher than in the other one. This finding is associated with changes in the morphology of precipitated eutectic carbides. As mentioned previously, increasing the Cr content produces a progressive reduction in the size of eutectic carbides regardless of their type. This suggestion is supported by the hardness profile of the eutectic HWSL no. H5. The eutectic HWSL, having the smallest precipitations of M_7C_3 eutectic carbides and their uniform distributions throughout the alloyed layer, exhibited the lowest average hardness value of about 650 HV. Moreover, it is essential to take into consideration that the presence of martensite can also affect the overall hardness of the HWSLs no. H1 and H5. It should be mentioned that a detailed microstructural analysis of the eutectic regions is currently in progress and the results will be reported elsewhere.

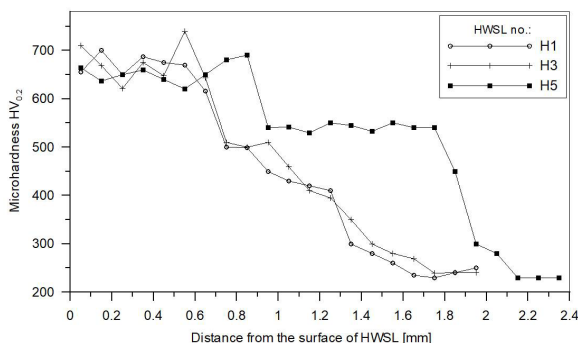


Fig. 16. Microhardness profiles for the HWSLs no. H1, H3, and H5

3 CONCLUSIONS

The hypoeutectic and eutectic HWSLs with a thickness up to 1.1 mm have been obtained on the DCI grade EN-GJS-700-2 substrate by the HPDD laser surface alloying with a pure chromium powder. The composition of the uniformly alloyed

layer contained up to 14.4 wt.% Cr. The type and morphology of eutectic carbides are influenced by both the Cr concentration in the molten pool and solidification conditions. It has been determined that when the total Cr content in the HWSL is higher than 10 wt.% the eutectic regions are composed almost completely of $\gamma_e + M_7C_3$. In turn, Cr contents higher than 12 wt.% ensure a formation of the eutectic microstructure ($\gamma_e + M_7C_3$). In general, the size of the eutectic carbides is found to decrease with increasing Cr content, regardless of the carbide type. One possible explanation for this finding is that the Cr concentration in the molten pool, at constant heat input level, influences the nucleation and growth process in the eutectic regions. Increasing the Cr content increases the eutectic carbide nucleation limiting their growth. At constant Cr content in the hypo-eutectic HWSL, the fraction of the eutectic carbides increases with a decrease of solidification and cooling rates. This variation in the fraction of eutectic carbides is attributed to a change of the Cr content in the primary austenite grains. Faster solidification and cooling rates result in the higher amount of Cr enrichment in the primary austenite grains, which, in turn, reduces the extent of the eutectic structure.

4 ACKNOWLEDGEMENTS

Publication of this article was funded by statutory grant of the Faculty of Mechanical Engineering, Silesian University of Technology.

5 REFERENCES

- [1] Fraś, E., Górny, M., Kapturkiewicz, W. (2013). Thin wall ductile iron casting: technological aspects. *Archives of Foundry Engineering*, vol. 13, no. 1, p. 23-28, DOI:10.2478/afe-2013-0005.
- [2] Abboud, J.H. (2012). Microstructure and erosion characteristic of nodular cast iron surface modified by tungsten inert gas. *Materials and Design*, vol. 35, p. 677-684, DOI:10.1016/j.matdes.2011.09.029.
- [3] Alabeedi, K.F., Abboud, J.H., Benyounis, K.Y. (2009). Microstructure and erosion resistance enhancement of nodular cast iron by laser melting. *Wear*, vol. 266, no. 9-10, p. 925-933, DOI:10.1016/j.wear.2008.12.015.
- [4] Sun, G., Zhou, R., Li, P., Feng, A., Zhang, Y. (2011). Laser surface alloying of C-B-W-Cr powders on nodular cast iron rolls. *Surface and Coatings Technology*, vol. 205, no. 8-9, p. 2747-2754, DOI:10.1016/j.surfcoat.2010.10.032.
- [5] Tański, T., Pakieła, W., Janicki, D., Tomiczek, B., Król, M. (2016). Properties of the aluminium alloy EN AC-51100 after laser surface treatment. *Archive of Metallurgy and Materials*, vol. 61, no. 1, p. 199-204, DOI:10.1515/amm-2016-0035.

- [6] Sušnik, J., Grum, J., Šturm, R. (2015). Effect of pulse laser energy density on TiC cladding of aluminium substrate. *Tehnički vjesnik - Technical Gazette*, vol. 22, no. 6, p. 1553-1560, DOI:10.17559/TV-20150221215735.
- [7] Nelson, G.D., Powell, G.L.F., Linton, V.M. (2006). Investigation of the wear resistance of high chromium white irons. *Surface Modification Technologies 2005: Proceedings of the 19th International Conference on Surface Modification Technologies*, p. 111-118.
- [8] Janicki, D. (2017). Laser cladding of Inconel 625-based composite coatings reinforced by porous chromium carbide particles. *Optics and Laser Technology*, vol. 94, p. 6-14, DOI:10.1016/j.optlastec.2017.03.007.
- [9] Dogan, O.N., Hawk, J.A., Laird II, G. (1997). Solidification structure and abrasion resistance of high chromium white irons. *Metallurgical and Materials Transactions A*, vol. 28, no. 6, p. 1315-1328, DOI:10.1007/s11661-997-0267-3.
- [10] Yan, H., Wang, A., Xiong, Z., Xu, K., Huang, Z. (2010). Microstructure and wear resistance of composite layers on a ductile iron with multcarbide by laser surface alloying. *Applied Surface Science*, vol. 256, no. 23, p. 7001-7009, DOI:10.1016/j.apsusc.2010.05.015.
- [11] Heydarzadeh Sohi, M., Ebrahimi, M., Ghasemi, H.M., Shahripour, A. (2012). Microstructural study of surface melted and chromium surface alloyed ductile iron. *Applied Surface Science*, vol. 258, no. 19, p. 7248-7353, DOI:10.1016/j.apsusc.2012.04.014.
- [12] Zárubová, N., Kraus, V., Čermák, J. (1992). Mechanisms of phase transformations during laser treatment of grey cast iron. *Journal of Materials Science*, vol. 27, no. 13, p. 3487-3496, DOI:10.1007/BF01151824.
- [13] Janicki, D. (2015). Direct diode laser surface melting of nodular cast iron. *Applied Mechanics and Materials*, vol. 809-810, p. 423-428, DOI:10.4028/www.scientific.net/AMM.809-810.423.
- [14] Voigt, R.C., Lopper, C.R. (1983). A study of heat-affected zone structure in ductile cast iron. *Welding Journal*, vol. 62, p. 82-88.
- [15] Orłowicz, W., Trytek, A. (2007). Shaping the microstructure and surface properties of ductile cast iron components by means of plasma surface modification. *Archive of Foundry*, vol. 7, no. 23. (in Polish)
- [16] Song, L. Qiao, Y., Wang, M. (2013). Effect of carbide orientation on impact-abrasive wear resistance of high-Cr iron used in shot balast machine. *Tribology Letters*, vol. 50, no. 3, p. 439-448, DOI:10.1007/s11249-013-0140-z.

Rapid and Automatic Zero-Offset Calibration of a 2-DOF Parallel Robot Based on a New Measuring Mechanism

Jiangping Mei – Jiawei Zang – Yabin Ding* – Shenglong Xie – Xu Zhang

Ministry of Education, Tianjin University, Key Laboratory of Mechanism Theory and Equipment Design, China

This paper deals with the rapid and automatic zero-offset calibration of a 2-DOF parallel robot using distance measurements. The calibration system is introduced with emphasis on the design of a new measuring mechanism. A simplified error model of the robot is proposed after the sensitivity analyses of source errors, based on which a zero-offset identification model is developed using the truncated singular value decomposition (TSVD) method, and then it is modified with the manufacturing and assembly errors of the measuring mechanism (MAEMM). Furthermore, an optimization approach for selecting measurement positions is proposed by considering the condition number of the identification matrix. Finally, simulations and experiments are carried out to verify the effectiveness of the zero-offset calibration method. The results show that the identification model has good identifiability and robustness, and the position accuracy after calibration can be significantly improved.

Keywords: parallel robot, calibration, zero offset, measuring mechanism

Highlights

- A new measuring mechanism is designed for the zero-offset calibration of a 2-DOF parallel robot.
- The zero-offset identification model is truncated by the TSVD method and modified with the MAEMM.
- The measurement positions are optimized based on the condition number of the identification matrix.
- Simulations and experiments are carried out to verify the effectiveness of the calibration method.

0 INTRODUCTION

Parallel robots have been widely used in many fields. This can be exemplified by the well-known Delta robot [1], including many applications of its modified versions, [2] to [4]. In recent years, the 2-DOF translational parallel robots has drawn ongoing interest from academia and industry due to their compact configurations and high stiffness, such as the very successful 4-PP [5] and 4-PP-E [6] simple decoupled XY parallel robots with enhanced stiffness, the Diamond [7] for high speed operation and the large-workspace 2-DOF parallel robot for solar tracking systems [8].

Position errors of parallel robots are mainly caused by their zero offsets, i.e. the errors between the nominal and actual initial positions of active links (see Fig. 1), provided that adequate fundamental geometric accuracy can be achieved at the manufacturing and assembly levels, [9] and [10]. The zero offsets may be caused by the control faults, collisions, or looseness of active joints at any time in practical applications. Therefore, to ensure the position accuracy, it is necessary to eliminate the zero offsets when they occur.

It is well recognized that the zero-offset calibration, one of the kinematic calibrations, is a practical and economical way to reduce zero offsets, [11] and [12]. The zero-offset calibration pays more

attention to the calibration of the zero offsets than the geometric errors. Furthermore, a fine calibration of the zero offsets is the premise to ensure the calibration accuracy of the geometric errors [13]. In general, the calibration can be implemented by four sequential processes, i.e. error modelling, measurement, identification and compensation such that the zero offsets affecting the position accuracy can be suppressed [14].

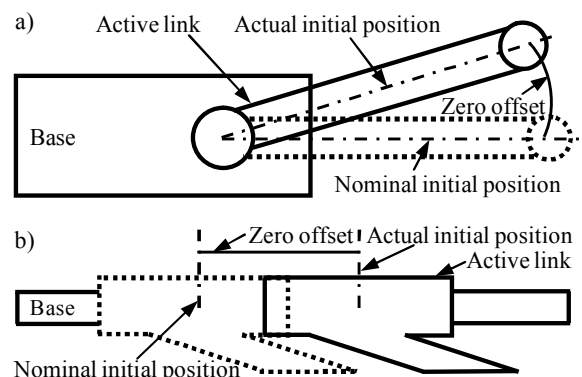


Fig. 1. Zero offsets of parallel robots; a) parallel robot with revolute joint; and b) parallel robot with prismatic joint

The methods of the zero-offset calibration can be classified into self/autonomous calibration [15] and external calibration [16]. Compared with the self/autonomous calibration that realizes the

*Corr. Author's Address: Tianjin University, Key Laboratory of Mechanism Theory and Equipment Design, No. 92 Weijin Road, Nankai District, Tianjin, China, dingyabin@126.com

identification of the zero offsets through minimizing the discrepancies between the measured and computed values of joint space sensors, the external calibration finishes the same work using task space sensors. Furthermore, the external calibration can be classified into the coordinate-based approach and the distance-based approach, [17] to [20]. In comparison with the coordinate-based approach, the advantage of the distance-based approach lies in that it is invariant with the chosen reference frame. Hence, it has been widely applied for the calibrations. For the data acquisition during the measurement process, it is usually implemented using a large metrology device, e.g. a laser tracker or interferometer, which is costly and inconvenient to use. Meanwhile, to ensure the identifiability, the number of measurement positions usually tends to be overlarge, which reduces the measurement efficiency. Therefore, the problem of how to make the measurement process in a time and cost-effective manner needs to be further studied.

The identification is the kernel process of calibration, and it is usually implemented using the least square (LS) method [21]. However, if the zero offsets are identified together with too many geometric errors, it may lead to a sharp increase in the condition number of the identification matrix and thereby cause the nonlinear ill-conditioning problem for identification model. To solve this problem, the ridge estimation (RE) method and the truncated singular value decomposition (TSVD) method have been widely adopted [22] and [23]. Some studies have indicated that the TSVD has better identification accuracy than the LS does, and it is easier to implement than the RE is. Though the nonlinear ill-conditioning problem can be solved to some extent by the RE or TSVD, the problem of how to further improve the identification accuracy of the zero offsets needs to be thoroughly investigated.

This paper deals with the rapid and automatic zero offset calibration of a 2-DOF parallel robot [24]. We focus on: 1) the design of a new measuring mechanism to make the measurement process in a time and cost-effective manner; 2) the development of a simplified error model containing the zero offsets of the robot; 3) the development of an identification method to solve the nonlinear ill-conditioning problem and improve the identifiability; 4) the selection of optimal measurement positions to further improve the identifiability and the measurement efficiency. Simulations and experiments are also carried out to validate the proposed calibration method.

1 SYSTEM DESCRIPTION

As shown in Fig. 2, the 2-DOF parallel robot is revolute jointed. Driven by two active proximal links, the robot can provide its moving platform with a 2-DOF translational moving capability.

Fig. 3 shows the new measuring mechanism which mainly consists of two revolute joints, two guide rods, a shipper rod and a linear scale. The two guide rods and the linear scale are arranged in parallel and fixed on two connecting plates. The shipper rod and the reading head of the linear scale are fixed on a slider which is vertically connected to the two guide rods by linear bearings. The revolute joints 3 and 4 are fixed on the upper connecting plate and the end of the shipper rod, respectively, based on which the measuring mechanism can be connected to the base and the moving platform of the robot.

By letting the moving platform undergo several measurement positions, the distance changes between the revolute joints 3 and 4 can be automatically obtained by the reading head and then transferred into the zero-offset calibration model in the robot controller. Thus, the zero offsets can be rapidly calibrated.

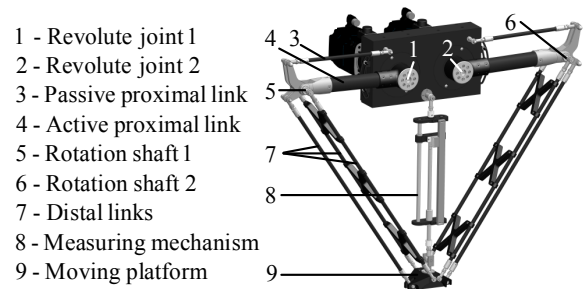


Fig. 2. 3D model of the 2-DOF parallel robot

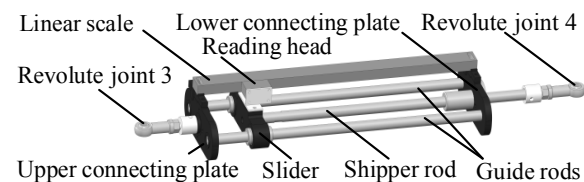


Fig. 3. 3D model of the measuring mechanism

2 KINEMATIC ANALYSES

The 2-DOF parallel robot can be simplified as shown in Fig. 4. In the $O-xy$ coordinate system, the nominal position vector, $\mathbf{r} = (x \ y)^T$, of the reference point P can be written as:

$$\mathbf{r} = \mathbf{e}_i + L_i \mathbf{u}_i + l_i \mathbf{w}_i, \quad i = 1, 2, \quad (1)$$

where L_i , l_i , \mathbf{u}_i and \mathbf{w}_i are the nominal lengths and nominal unit orientation vectors of the proximal and distal links, respectively; \mathbf{e}_i is the nominal position vector of A_i ; and

$$\begin{aligned} \mathbf{u}_i &= (\cos\theta_i \quad \sin\theta_i)^\top, \quad \mathbf{w}_i = (\cos\varphi_i \quad \sin\varphi_i)^\top, \\ \mathbf{e}_i &= (e_{ix} \quad e_{iy})^\top, \end{aligned} \quad (2)$$

where θ_i and φ_i are the nominal rotation angles of the proximal and distal links, respectively.

Taking 2-norm on the two sides of Eq. (1), the solution of the inverse positional analysis can then be expressed as:

$$\theta_i = 2 \arctan \frac{-C_i - \sqrt{C_i^2 - D_i^2 + E_i^2}}{D_i - E_i}, \quad (3)$$

where $C_i = -2L_i(y - e_{iy})$, $D_i = -2L_i(x - e_{ix})$,

$$E_i = (x - e_{ix})^2 + (y - e_{iy})^2 + L_i^2 - l_i^2.$$

Hence, \mathbf{w}_i and the position vector from O_1 to O_2 , denoted by λ , can be calculated as follows:

$$\mathbf{w}_i = \frac{\mathbf{r} - \mathbf{e}_i - L_i \mathbf{u}_i}{l_i}, \quad \lambda = \mathbf{r} - \mathbf{c} - \mathbf{d}, \quad (4)$$

where \mathbf{c} is the position vector from O to O_1 ; \mathbf{d} is the position vector from O_2 to P .

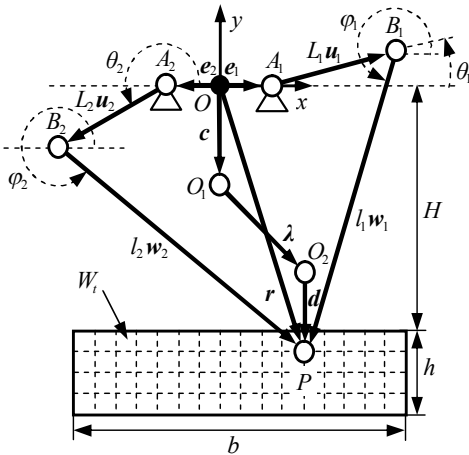


Fig. 4. Kinematic model of the 2-DOF parallel robot

(Note: A_1 (A_2) is the nominal rotation centre of the revolute joint 1 (2);

B_1 (B_2) is the nominal rotation centre of the rotation shaft 1 (2);

O_1 (O_2) is the nominal rotation centre of the revolute joint 3 (4);

P is a reference point at the centre of the moving platform;

W_1 is the workspace; H is the distance between O and the upper boundary

of the workspace; h is the height of the workspace;

b is the width of the workspace)

To develop the forward positional model, rewrite Eq. (1) as:

$$\mathbf{r}^\top \mathbf{r} - 2(\mathbf{e}_i + L_i \mathbf{u}_i)^\top \mathbf{r} + (\mathbf{e}_i + L_i \mathbf{u}_i)^\top (\mathbf{e}_i + L_i \mathbf{u}_i) = l_i^2. \quad (5)$$

Subtract the two equations in Eq. (5) with each other yields:

$$x = -\frac{My + S}{F}, \quad (6)$$

$$\begin{aligned} \text{where } F &= 2[(\mathbf{e}_2 + L_2 \mathbf{u}_2)^\top - (\mathbf{e}_1 + L_1 \mathbf{u}_1)^\top] \mathbf{a}_1, \\ M &= 2[(\mathbf{e}_2 + L_2 \mathbf{u}_2)^\top - (\mathbf{e}_1 + L_1 \mathbf{u}_1)^\top] \mathbf{a}_2, \\ S &= \|\mathbf{e}_1 + L_1 \mathbf{u}_1\|^2 - \|\mathbf{e}_2 + L_2 \mathbf{u}_2\|^2 - (l_1^2 - l_2^2), \\ \mathbf{a}_1 &= (1 \quad 0)^\top, \quad \mathbf{a}_2 = (0 \quad 1)^\top. \end{aligned}$$

Substitute Eq. (6) into Eq. (5), then the quadratic equation of y can be written as:

$$Ny^2 + Q_i + R_i = 0, \quad (7)$$

where

$$R_i = \frac{S^2}{F^2} + 2 \frac{S}{F} (\mathbf{e}_i + L_i \mathbf{u}_i)^\top \mathbf{a}_1 + \|\mathbf{e}_i + L_i \mathbf{u}_i\|^2 - l_i^2,$$

$$N = 1 + \frac{M^2}{F^2}, \quad Q_i = \frac{2MS}{F^2} + 2(\mathbf{e}_i + L_i \mathbf{u}_i)^\top \left(\frac{M}{F} \mathbf{a}_1 - \mathbf{a}_2 \right).$$

According to the assembly mode of the robot, the y coordinate of P can be expressed as:

$$y = \frac{-Q_i - \sqrt{Q_i^2 - 4NR_i}}{2N}. \quad (8)$$

Hence, substitute Eq. (8) into Eq. (6), then the x coordinate of P can be determined.

3 ERROR MODELLING AND SENSITIVITY ANALYSES

The first-order approximation of Eq. (1) can be formulated by:

$$\Delta \mathbf{r} = \Delta \mathbf{e}_i + \Delta L_i \mathbf{u}_i + L_i \Delta \mathbf{u}_i + \Delta l_i \mathbf{w}_i + l_i \Delta \mathbf{w}_i, \quad (9)$$

where $\Delta \mathbf{r} = (\Delta x \quad \Delta y)^\top$ is the position error vector of the reference point P ; $\Delta \mathbf{e}_i = (\Delta e_{ix} \quad \Delta e_{iy})^\top$ is the position error vector of A_i ; ΔL_i , Δl_i , $\Delta \mathbf{u}_i$ and $\Delta \mathbf{w}_i$ are the length errors and orientation error vectors of the proximal and distal links. Furthermore, the first-order approximation of \mathbf{u}_i can be written as:

$$\Delta \mathbf{u}_i = \Delta \theta_i (-\sin \theta_i \quad \cos \theta_i)^\top = \mathbf{Q} \mathbf{u}_i \Delta \theta_i, \quad \mathbf{Q} = \begin{bmatrix} 0 & -1 \\ 1 & 0 \end{bmatrix}, \quad (10)$$

where $\Delta \theta_i$ is the zero offset of the robot.

Then, taking the dot product with $\Delta \mathbf{w}_i^\top$ on the both sides of Eq. (9) (note that $\mathbf{w}_i \perp \Delta \mathbf{w}_i$) yields:

$$\mathbf{w}_i^\top \Delta \mathbf{r} = \mathbf{w}_i^\top \Delta \mathbf{e}_i + \Delta L_i \mathbf{w}_i^\top \mathbf{u}_i + L_i \mathbf{w}_i^\top \mathbf{Q} \mathbf{u}_i \Delta \theta_i + \Delta l_i. \quad (11)$$

For a parallel robot, its error model is usually expressed in matrix form, such that the relationship between the position error and the source errors can be directly revealed by an error transfer matrix.

According to Eq. (11), the error model of the robot can be expressed as

$$\Delta \mathbf{r} = \mathbf{J}' \Delta \mathbf{q}', \quad (12)$$

where \mathbf{J}' denotes the error transfer matrix, and

$$\begin{aligned} \mathbf{J}' &= [\mathbf{w}_1 \quad \mathbf{w}_2]^{-\text{T}} \begin{bmatrix} \mathbf{J}'_1 & \mathbf{0} \\ \mathbf{0} & \mathbf{J}'_2 \end{bmatrix}, \quad \Delta \mathbf{q}' = \begin{pmatrix} \Delta \mathbf{q}'_1 \\ \Delta \mathbf{q}'_2 \end{pmatrix}, \\ \mathbf{J}'_1 &= (\mathbf{w}_1^{\text{T}} \mathbf{Q} \mathbf{u}_1 \quad w_{1x} \quad w_{1y} \quad \mathbf{w}_1^{\text{T}} \mathbf{u}_1 \quad 1), \\ \mathbf{J}'_2 &= (\mathbf{w}_2^{\text{T}} \mathbf{Q} \mathbf{u}_2 \quad w_{2x} \quad w_{2y} \quad \mathbf{w}_2^{\text{T}} \mathbf{u}_2 \quad 1), \\ \Delta \mathbf{q}'_1 &= (L_1 \Delta_1 \quad \Delta e_{1x} \quad \Delta e_{1y} \quad \Delta L_1 \quad \Delta l_1)^{\text{T}}, \\ \Delta \mathbf{q}'_2 &= (L_2 \Delta_2 \quad \Delta e_{2x} \quad \Delta e_{2y} \quad \Delta L_2 \quad \Delta l_2)^{\text{T}}. \end{aligned}$$

Since the robot has symmetrical geometry, the sensitivity analyses of the source errors can be studied by analysing the variation of $\Delta \rho_0$ ($\Delta \rho_0$ is the absolute distance error of P_0 , and P_0 is the home position at which $\theta_1 = 0^\circ$ and $\theta_2 = 180^\circ$) versus the source errors within the 1st limb.

Given $L_1 = L_2 = L$, $l_1 = l_2 = l$, $e_{1x} = -e_{2x} = e_x$ and $e_{1y} = e_{2y} = e_y$, the nominal geometric parameters of the robot are listed in Table 1, and the results of the sensitivity analyses are presented in Fig. 5. It can be seen that the position accuracy is more sensitive to the zero offset than the geometric errors. Hence assume that the adequate fundamental geometric accuracy of the robot can be achieved, Eq. (12) can be simplified as follows:

$$\Delta \mathbf{r} = \mathbf{J} \Delta \mathbf{q}, \quad (13)$$

where

$$\mathbf{J} = [\mathbf{w}_1 \quad \mathbf{w}_2]^{-\text{T}} \begin{bmatrix} \mathbf{w}_1^{\text{T}} \mathbf{Q} \mathbf{u}_1 & 0 \\ 0 & \mathbf{w}_2^{\text{T}} \mathbf{Q} \mathbf{u}_2 \end{bmatrix}, \quad \Delta \mathbf{q} = \begin{pmatrix} L_1 \Delta \theta_1 \\ L_2 \Delta \theta_2 \end{pmatrix}.$$

Table 1. Nominal geometric parameters [mm]

e_x	e_y	L	l	H	b	h	c_x	c_y	d_x	d_y
80	0	375	825	632	480	150	0	79	0	51

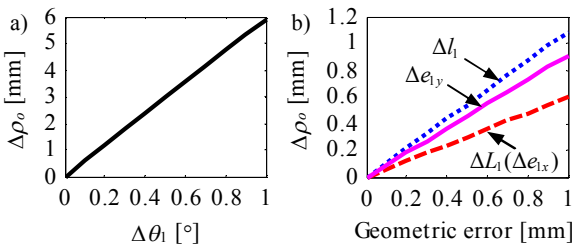


Fig. 5. Sensitivity analyses; a) variation of $\Delta \rho_0$ vs. $\Delta \theta_1$ and $\Delta \phi_0$ and b) variations of $\Delta \rho_0$ vs. geometric errors

4 ZERO OFFSET IDENTIFICATION

The zero-offset identification model is developed based on two adjacent measurement positions, P_k and P_{k+1} ($1 \leq k \leq K-1$, and K is the total number of measurement positions). As shown in Fig. 6, considering the position errors of O_1 and O_2 , then $\widehat{O}_1 \widehat{O}_2$ and $\widehat{O}'_1 \widehat{O}'_2$ of P_k , denoted by λ_k and ρ_k , respectively, can be expressed as:

$$\lambda_k = \lambda_k \widehat{\lambda}_k = \mathbf{r}_k - \mathbf{c} - \mathbf{d}, \quad (14)$$

$$\rho_k = \rho_k \widehat{\rho}_k = \mathbf{r}'_k - \mathbf{c}' - \mathbf{d}', \quad (15)$$

where λ_k and $\widehat{\lambda}_k$ are the length and unit orientation vector of λ_k ; ρ_k and $\widehat{\rho}_k$ are the length and unit orientation vector of ρ_k ; \mathbf{r}_k and \mathbf{r}'_k are the nominal and actual position vectors of P_k ; \mathbf{c}' is the position vector from O to O'_1 ; \mathbf{d}' is the position vector from O'_2 to P'_k . Then, taking the first-order approximation of Eq. (14) yields:

$$\Delta \lambda_k \widehat{\lambda}_k + \lambda_k \Delta \widehat{\lambda}_k = \Delta \mathbf{r}_k - \Delta \mathbf{r}_M, \quad (16)$$

where $\Delta \lambda_k$ and $\Delta \widehat{\lambda}_k$ are the length error and orientation error vector of λ_k ; $\Delta \mathbf{r}_k$ is the position error vector of P_k ; $\Delta \mathbf{r}_M = (\Delta r_{Mx} \quad \Delta r_{My})^{\text{T}}$ is the MAEMM; and we can obtain:

$$\Delta \mathbf{r}_M = \Delta \mathbf{c} + \Delta \mathbf{d}, \quad \Delta \mathbf{c} = \mathbf{c}' - \mathbf{c}, \quad \Delta \mathbf{d} = \mathbf{d}' - \mathbf{d}, \quad (17)$$

$$\Delta \lambda_k = \rho_k - \lambda_k, \quad (18)$$

where $\Delta \mathbf{c}'$ and $\Delta \mathbf{d}'$ are the position error vectors of O_1 and O_2 , respectively.

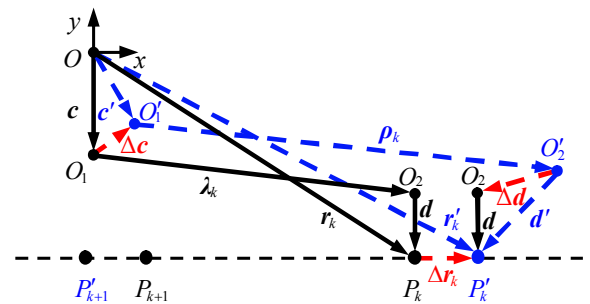


Fig. 6. Error model of the measuring mechanism

Note: O'_1 (O'_2) is the actual rotation centre of the revolute joint 3 (4); P_k (P_{k+1}) and P'_k (P'_{k+1}) are the k^{th} ($(k+1)^{\text{th}}$) nominal and actual measurement positions, respectively

Taking dot product with $\widehat{\lambda}_k^{\text{T}}$ on the both sides of Eq. (16) (note that $\widehat{\lambda}_k \perp \Delta \widehat{\lambda}_k$) yields:

$$\Delta \lambda_k = \widehat{\lambda}_k^{\text{T}} (\Delta \mathbf{r}_k - \Delta \mathbf{r}_M). \quad (19)$$

Then substituting Eq. (12) and Eq. (18) into Eq. (19), we can obtain:

$$\rho_k - \lambda_k = \hat{\lambda}_k^T (\mathbf{J}'_k \Delta \mathbf{q}' - \Delta \mathbf{r}_M), \quad (20)$$

where \mathbf{J}'_k is the error transfer matrix \mathbf{J}' of P_k .

Rewriting Eq. (20) as:

$$\rho_k - \lambda_k = \mathbf{g}'_k \Delta \mathbf{p}, \quad (21)$$

where $\mathbf{g}'_k = \hat{\lambda}_k^T [\mathbf{J}'_k \quad -\mathbf{I}]$, $\mathbf{I} = \begin{bmatrix} 1 & 0 \\ 0 & 1 \end{bmatrix}$, $\Delta \mathbf{p}' = \begin{pmatrix} \Delta \mathbf{q}' \\ \Delta \mathbf{r}_M \end{pmatrix}$.

We can also get Eq. (22) according to P_{k+1} :

$$\rho_{k+1} - \lambda_{k+1} = \mathbf{g}'_{k+1} \Delta \mathbf{p}', \quad (22)$$

where $\mathbf{g}'_{k+1} = \hat{\lambda}_{k+1}^T [\mathbf{J}'_{k+1} \quad -\mathbf{I}]$; ρ_{k+1} and $\hat{\rho}_{k+1}$ are the length and unit orientation vector of ρ_{k+1} ; ρ_{k+1} is $\overline{O_1 O_2}$ of P_{k+1} ; λ_{k+1} and $\hat{\lambda}_{k+1}$ are the length and unit orientation vector of λ_{k+1} ; λ_{k+1} is $\overline{O_1 O_2}$ of P_{k+1} ; and \mathbf{J}'_{k+1} is the error transfer matrix \mathbf{J}' of P_{k+1} .

Subtracting Eq. (22) with Eq. (21) leads to:

$$(\rho_{k+1} - \rho_k) - (\lambda_{k+1} - \lambda_k) = (\mathbf{g}'_{k+1} - \mathbf{g}'_k) \Delta \mathbf{p}'. \quad (23)$$

Hence, the matrix form of the identification model can be expressed as:

$$\Delta \lambda = \mathbf{G}' \Delta \mathbf{p}', \quad (24)$$

where

$$\Delta \lambda = \begin{pmatrix} (\rho_2 - \rho_1) - (\lambda_2 - \lambda_1) \\ \vdots \\ (\rho_{k+1} - \rho_k) - (\lambda_{k+1} - \lambda_k) \\ \vdots \\ (\rho_K - \rho_{K-1}) - (\lambda_K - \lambda_{K-1}) \end{pmatrix}, \quad \mathbf{G}' = \begin{pmatrix} \mathbf{g}'_2 - \mathbf{g}'_1 \\ \vdots \\ \mathbf{g}'_{k+1} - \mathbf{g}'_k \\ \vdots \\ \mathbf{g}'_K - \mathbf{g}'_{K-1} \end{pmatrix}.$$

It is easy to prove that $\text{rank}(\mathbf{G}') = 12$ if $K \geq 13$ provided that $\hat{\lambda}_1, \hat{\lambda}_2, \dots, \hat{\lambda}_{K-1}$ and $\hat{\lambda}_K$ are not co-linear, then $\Delta \mathbf{p}'$ can be identified using the LS method:

$$\Delta \mathbf{p}' = [(\mathbf{G}')^T \mathbf{G}']^{-1} (\mathbf{G}')^T \Delta \lambda. \quad (25)$$

The singular value decomposition method is often used to study the identifiability, by which the identification matrix \mathbf{G}' can be rewritten as:

$$\mathbf{G}' = \mathbf{U}' \mathbf{S}' (\mathbf{V}')^T \quad (26)$$

where \mathbf{U}' and \mathbf{V}' are $(K-1) \times (K-1)$ and 12×12 matrixes, respectively, and each of them is composed of a set of standard orthogonal bases; \mathbf{S}' is a diagonal matrix composed of the singular values of \mathbf{G}' . Hence, Eq. (25) can be rewritten as:

$$\Delta \mathbf{p}' = \sum_{i=1}^{12} \frac{(\mathbf{u}'_i)^T \Delta \lambda}{\sigma'_i} \mathbf{v}'_i, \quad (27)$$

where \mathbf{u}'_i is the standard orthogonal basis of \mathbf{U}' ; \mathbf{v}'_i is the standard orthogonal basis of \mathbf{V}' ; σ'_i is the singular value of \mathbf{G}' , and $\sigma'_1 \geq \sigma'_2 \geq \dots \geq \sigma'_{12} > 0$.

The TSVD method can be used to improve the identifiability of $\Delta \mathbf{p}'$ by simply truncating the summation in Eq. (27) at an upper limit $t \leq 12$ before the small singular values start to dominate. However, if the zero offsets are identified together with too many geometric errors, the upper limit of t will be too large and then the TSVD may be performed like the LS that cannot overcome the nonlinear ill-conditioning problem of Eq. (25). Since it has been proved in Section 3 that the position accuracy is more sensitive to the zero offset than the geometric errors, the nonlinear ill-conditioning problem can be directly solved to some extent by neglecting the identification of the geometric errors according to the TSVD method, i.e. by substituting Eq. (13) and Eq. (18) into Eq. (19), then the identification model can be degenerated into the following form:

$$\Delta \lambda = \mathbf{G} \Delta \mathbf{p}, \quad \mathbf{G} = \begin{bmatrix} \mathbf{g}_2 - \mathbf{g}_1 \\ \vdots \\ \mathbf{g}_{k+1} - \mathbf{g}_k \\ \vdots \\ \mathbf{g}_K - \mathbf{g}_{K-1} \end{bmatrix}, \quad \begin{cases} \Delta \mathbf{p} = (\Delta \mathbf{q} \quad \Delta \mathbf{r}_M)^T \\ \mathbf{g}_k = \hat{\lambda}_k^T [\mathbf{J}_k \quad -\mathbf{I}] \\ \mathbf{g}_{k+1} = \hat{\lambda}_{k+1}^T [\mathbf{J}_{k+1} \quad -\mathbf{I}] \end{cases}, \quad (28)$$

where \mathbf{J}_k and \mathbf{J}_{k+1} are the error transfer matrix \mathbf{J} of P_k and P_{k+1} , respectively.

It can also be proved that $\text{rank}(\mathbf{G}) = 4$ if $K \geq 5$ provided that $\hat{\lambda}_1, \hat{\lambda}_2, \dots, \hat{\lambda}_{K-1}$ and $\hat{\lambda}_K$ are not co-linear. Hence, $\Delta \mathbf{p}$ can be calculated by

$$\Delta \mathbf{p} = \sum_{i=1}^4 \frac{(\mathbf{u}_i)^T \Delta \lambda}{\sigma_i} \mathbf{v}_i, \quad (29)$$

where \mathbf{u}_i , \mathbf{v}_i and σ_i are the standard orthogonal bases and singular value derived from the SVD format of the identification matrix \mathbf{G} .

Since we neglect the identification of the geometric errors, the accuracy of $\Delta \theta_i$ solved by Eq. (29) may be slightly decreased even though the nonlinear ill-conditioning problem can be solved. To improve the accuracy, the following aspects are considered: (1) the source errors should be identified multiple times; (2) the measuring mechanism is used as a metrology device and its measurement accuracy can be improved with the decrease of $\Delta \mathbf{r}_M$; (3) $\Delta \mathbf{r}_M$ is independent of the source errors of the robot, and the smaller $\Delta \mathbf{r}_M$ the better the identifiability of $\Delta \theta_i$. Based on these considerations, the identification model can be modified as follows.

For the 1st identification, we use Eq. (29) to identify $\Delta \mathbf{p}$; for the j^{th} ($j \geq 2$) identification, by modifying Eq. (20) with the former identification result of $\Delta \mathbf{r}_M$ as shown in Eq. (30), then the j^{th} identification model can be redeveloped:

6 SIMULATION ANALYSES

$$\rho_k - \|\mathbf{f}_k^{(j)}\| = \frac{(\mathbf{f}_k^{(j)})^T}{\|\mathbf{f}_k^{(j)}\|} (\mathbf{J}_k \Delta \mathbf{q}^{(j)} - \Delta \mathbf{r}_M^{(j)}), \quad (30)$$

where $\mathbf{f}_k^{(j)} = \mathbf{f}_k^{(j-1)} + \Delta \mathbf{r}_M^{(j-1)}$, and $\mathbf{f}_k^{(1)} = \lambda_k$.

5 OPTIMAL MEASUREMENT POSITIONS AND ERROR COMPENSATION STRATEGY

The identification of $\Delta \rho$ requires the moving platform to undergo $K \geq 5$ measurement positions; meanwhile, these positions should converge to the boundaries of the workspace where the highest signal-to-noise ratio may be achieved. In addition, the moving platform should experience all the controllable degrees of freedom. As shown in Fig. 7, the most straightforward way is to choose n evenly spaced positions on each of the upper and lower boundaries of the workspace.

Since the identifiability can be improved with the decrease of the condition number of the identification matrix, to make the measurements in a time-effective manner, the selection problem of the optimal measurement positions can be solved by minimizing n , κ_1 and κ_m subject to a given threshold ε_0 defined as the relative difference between κ_1 and κ_m vs. n , i.e.

$$\min \{n, \kappa_1, \kappa_m\} \quad \text{s.t.} \quad \varepsilon = \frac{|\kappa_1 - \kappa_m|}{\kappa_1} \leq \varepsilon_0, \quad n \geq 3, \quad (31)$$

where κ_1 denotes the condition number of the first identification; and κ_m denotes the mean condition number of the remaining identifications.

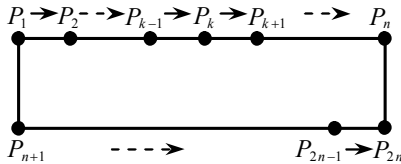


Fig. 7. Optimal measurement positions

After $\Delta \theta_i$ of the j^{th} and $(j+1)^{\text{th}}$ identifications are obtained, the position error of the robot can be reduced in an iterative manner by compensating the kinematic model in the robot controller with the identification results of $\Delta \theta_i$ until the compensation accuracy μ defined as follows converges within a given threshold μ_0 :

$$\mu = \sqrt{[(\Delta \theta_1^{(j+1)} - \Delta \theta_1^{(j)})^2 + (\Delta \theta_2^{(j+1)} - \Delta \theta_2^{(j)})^2] / 2}. \quad (32)$$

Then the compensation value of $\Delta \theta_i$ is:

$$\Delta \theta_i = \Delta \theta_i^{(1)} + \Delta \theta_i^{(2)} + \dots + \Delta \theta_i^{(j)} + \dots + \Delta \theta_i^{(m)}, \quad (33)$$

where m is the compensation number.

In this section, simulations are carried out to investigate the accuracy and robustness of the zero-offset calibration method in depth.

6.1 Simulation Parameters

The given source errors are listed in Table 2. This is because: 1) the investigation of the identification accuracy requires the given values of $\Delta \theta_i$ to cover a certain range; 2) the different attainable geometric accuracies of the robot should be considered; 3) the MAEMM can be roughly measured, and Δr_{Mx} and Δr_{My} are about 1 mm and 0.5 mm, respectively.

Given $\Delta \mathbf{r}_M^{(j)} = (1 \ 0.5)^T$ ($2 \leq j \leq m$), it can be seen from Fig. 8 that, for each simulation group, κ_1 and κ_m both monotonically increase with the increase of n . Meanwhile, κ_m is less than κ_1 corresponding to the same n , meaning that the identifiability can be slightly improved by using Eq. (30). Furthermore, given $\varepsilon_0 = 0.01$, it can also be seen that the minimum n is 3, which leads to $K = 2n = 6$ optimal measurement positions.

Based on the optimal positions, $(\lambda_k - \lambda_{k+1})$ can be obtained by the inverse positional analysis, and $(\rho_k - \rho_{k+1})$ can be derived from the forward positional model containing the source errors and considering the measurement errors. Then $\Delta \theta_i$ can be calibrated using the proposed method.

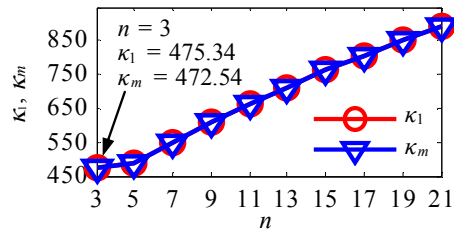


Fig. 8. Variations of κ_1 and κ_m vs. n

In the calibration, the measurement errors are mainly caused by the linear scale and servo motor, which can be reasonably set as follows.

Since the maximum measurement error of the linear scale is $\pm (3 + l_0/1000) \times 10^{-3}$ mm (l_0 is the measuring range of the linear scale and $l_0 = 350$ mm); meanwhile, the output of the reading head can be reset after each measurement, the measurement error of the linear scale corresponding to P_k , denoted by ω_k , can be set as the Gaussian distributed error with mean 0 and variance ω^2 , and ω can be calculated by:

$$\omega = \frac{1}{3} \left(3 + \frac{l_0}{1000} \right) \times 10^{-3}. \quad (34)$$

Table 2. Set values of the source errors

Group	Zero offset [°]		Geometric error [mm]								MAEMM [mm]	
	$\Delta\theta_1$	$\Delta\theta_2$	Δe_{1x}	Δe_{1y}	Δe_{2x}	Δe_{2y}	ΔL_1	ΔL_2	Δl_1	Δl_2	Δr_{Mx}	Δr_{My}
1	2	-1										
2	-1	0.5	0.03	-0.02	-0.02	0.01	0.01	0.02	-0.03	-0.02		
3	0.5	0.25										
4	2	-1									1	0.5
5	-1	0.5	0.003	-0.002	-0.002	0.001	0.001	0.002	-0.003	-0.002		
6	0.5	0.25										

Table 3. Simulation results of $\Delta\theta_i$ and $\Delta\rho_0$

Group	Zero offset	Compensation value [°]	δ [°]	$\Delta\rho_0$ (before) [mm]	$\Delta\rho_0$ (after) [mm]
1	$\Delta\theta_1$	2.033	0.033	10.933	0.402
	$\Delta\theta_2$	-0.957	0.043		
2	$\Delta\theta_1$	-1.049	0.049	5.482	0.423
	$\Delta\theta_2$	0.463	0.037		
3	$\Delta\theta_1$	0.536	0.036	3.796	0.434
	$\Delta\theta_2$	0.297	0.047		
4	$\Delta\theta_1$	2.024	0.024	10.896	0.228
	$\Delta\theta_2$	-0.978	0.022		
5	$\Delta\theta_1$	-1.025	0.025	5.5195	0.256
	$\Delta\theta_2$	0.474	0.026		
6	$\Delta\theta_1$	0.476	0.024	3.798	0.239
	$\Delta\theta_2$	0.225	0.025		

Considering that the number of pulses per revolution of the servo motor is 1×10^4 and the maximum number of pulse error per revolution is 4, the motion error of the servo motor corresponding to P_k , denoted by ξ_k , can also be set as the Gaussian distributed error with mean 0 and variance ξ^2 , and ξ can be calculated by:

$$\xi = \frac{1}{3} \left(\frac{4}{\eta \times 10^4} \right) \times 360^\circ, \quad (35)$$

where $\eta = 20$ is the reduction ratio of the reducer.

6.2 Simulation Results and Discussion

Given $\mu_0 = 0.1^\circ$, the compensation value of $\Delta\theta_i$, the absolute difference between the set and compensation values of $\Delta\theta_i$, denoted by δ , and $\Delta\rho_0$ before and after calibration are listed in Table 3. It can be seen that δ is around 0.040° in the first three groups and 0.025° in the last three groups. This indicates that the identification accuracy is invariant with the set values of $\Delta\theta_i$, and that it can be slightly improved with the decrease of the geometric errors. Furthermore, $\Delta\rho_0$ can be significantly reduced after calibration, and the

maximum $\Delta\rho_0$ after calibration is 0.434 mm in the first three groups and 0.256 mm in the last three groups.

As shown in Table 4, for each group, the maximum absolute distance error, denoted by $\Delta\rho_{\max}$, of the six optimal measurement positions can be reduced to a certain value after calibration. Since these positions are along the boundaries of the workspace where the position errors usually tend to be much larger than those of the internal positions, we can infer that the position accuracy throughout the workspace of the robot can be well improved after the calibration.

Table 4. $\Delta\rho_{\max}$ before and after calibration

Group	1	2	3	4	5	6
$\Delta\rho_{\max}$ (before) [mm]	12.906	6.418	4.672	12.868	6.455	4.663
$\Delta\rho_{\max}$ (after) [mm]	0.493	0.531	0.533	0.279	0.314	0.293

Table 5 shows the absolute differences between the set values and identification results of Δr_{Mx} and Δr_{My} , denoted by δ_{Mx} and δ_{My} , respectively. It can be seen that, similar to the identification results of $\Delta\theta_i$, the identification accuracies of Δr_{Mx} and Δr_{My} are scarcely affected by the set values of $\Delta\theta_i$, while they can be slightly improved with the decrease of the geometric errors of the robot.

Table 5. Absolute differences between the set values and identification results of Δr_{Mx} and Δr_{My}

Group	1	2	3	4	5	6
δ_{Mx} [mm]	0.069	0.074	0.071	0.044	0.051	0.047
δ_{My} [mm]	0.040	0.045	0.042	0.022	0.028	0.024

As shown in Table 6, of each group is about 472.50, which is almost the same as $\kappa_m = 472.54$ and less than $\kappa_1 = 475.34$ as shown in Fig. 8, further verifying that the identifiability of the identification

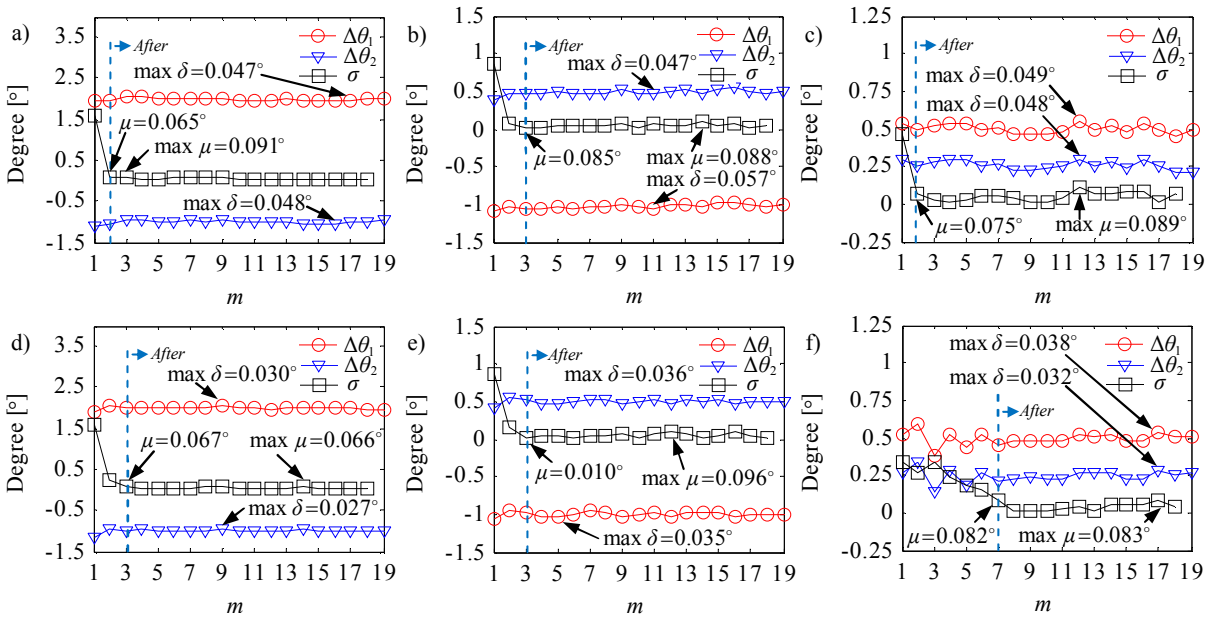


Fig. 9. Robustness analyses; a) group 1; b) group 2; c) group 3; d) group 4; e) group 5; and f) group 6

model modified using Eq. (30) can be slightly improved.

Table 6. Mean condition number

Group	1	2	3	4	5	6
κ_m	472.47	472.49	472.49	472.50	472.51	472.50

Table 7. Experimental results of $\Delta\theta_i$ and $\Delta\rho_0$

Group	Zero-offset	Compensation value [°]	δ [°]	$\Delta\rho_0$ (before) [mm]	$\Delta\rho_0$ (after) [mm]
1	$\Delta\theta_1$	1.929	0.071	12.062	0.732
	$\Delta\theta_2$	-0.924	0.076		
2	$\Delta\theta_1$	-0.935	0.065	6.964	0.605
	$\Delta\theta_2$	0.572	0.072		
3	$\Delta\theta_1$	0.569	0.069	4.945	0.711
	$\Delta\theta_2$	0.175	0.075		

Further research is performed to evaluate the robustness of the identification model. The variations of the compensation value of $\Delta\theta_i$ and the defined compensation accuracy μ versus m of each group are presented in Fig. 9. For each group, it can be observed that the compensation values of $\Delta\theta_1$ and $\Delta\theta_2$ both fluctuate slightly, but they can converge to different values with the increase of m . Furthermore, δ is less than 0.060° in the first three groups and 0.040° in the last three groups, and μ of each group after its value reduces to less than $\mu_0 = 0.1^\circ$ for the first time is

between 0° to 0.1° . These observations indicate that the identification model has good robustness.

7 EXPERIMENTAL VERIFICATION

Experiments are carried out on the 2-DOF parallel robot with the repeatability of ± 0.05 mm over its workspace to verify the effectiveness of the zero-offset calibration method.

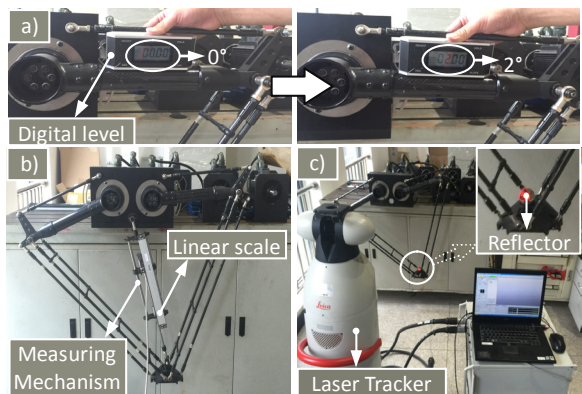


Fig. 10. Experiment set-ups; a) zero offset adjustment set-up; b) calibration set-up; and c) verification set-up

As shown in Fig. 10a, in order to compare the experiments with the simulations, a digital level with the maximum observed deviation of 0.1° is used to adjust the two active proximal links to the horizontal position before each experiment, and then

$\Delta\theta_1$ and $\Delta\theta_2$ can be roughly regarded as 0° . After that, $\Delta\theta_1$ and $\Delta\theta_2$ are set as listed in the first three groups of Table 2, respectively, by driving the two active proximal links to the corresponding positions. Having built the calibration set-up as shown in Fig. 10b, the experiments of the zero-offset calibration can be implemented, and the position errors before and after calibration are measured with a LEICA AT901 laser tracker with the maximum observed deviation of 0.016 mm as shown in Fig. 10c.

Table 8. Identification results of Δr_{Mx} and Δr_{My}

Group	1	2	3
Δr_{Mx} [mm]	0.842	0.835	0.852
Δr_{My} [mm]	0.592	0.576	0.583

Likewise, given $\mu_0 = 0.1^\circ$, the experimental results are listed in Tables 7 and 8, from which we can determine that, similar to the simulation results, the identification accuracy is invariant with the set values of $\Delta\theta_i$, and the $\Delta\rho_0$ of each group can be significantly reduced after calibration. We can also determine that the maximum δ and $\Delta\rho_0$ after calibration are 0.076° and 0.732 mm, respectively, which are slightly larger than 0.049° and 0.434 mm of the simulations. Since it has been proved via the simulation analyses that the identifiability will decrease with the increase of the geometric errors, the slight decrease of the identification accuracy in the experiments is due to the fact that the actual geometric errors of the robot are larger than those given in the simulations.

As shown in Fig. 11, in order to carry out deeper investigation on the position accuracy, the absolute distance error, denoted by $\Delta\rho$, before and after calibration of $K = 42$ evenly spaced measurement positions along the boundaries of the workspace are measured by the laser tracker, and the results are presented in Fig. 12. Furthermore, the maximum position error $\Delta\rho_{\max}$ of these positions are listed in Table 9. It can be seen that the maximum position error along the workspace of each group can also be significantly reduced to less than 0.85 mm after the calibration.

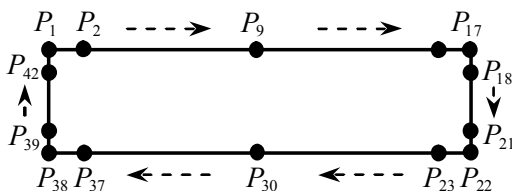


Fig. 11. The 42 measurement positions

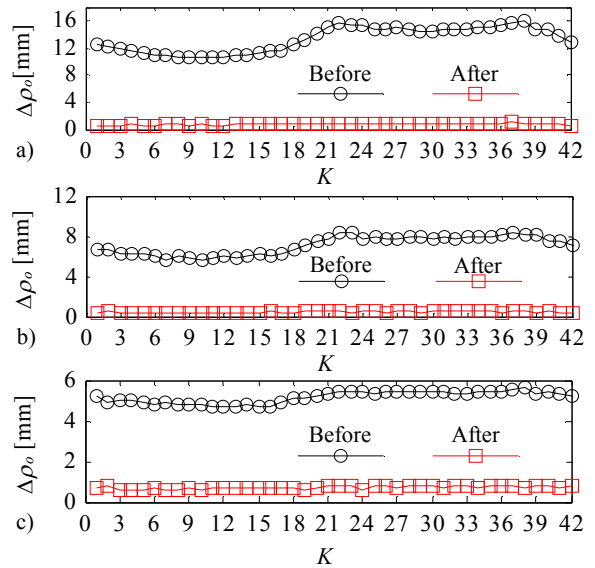


Fig. 12. $\Delta\rho$ before and after calibration; a) group 1; b) group 2; and c) group 3

Table 9. $\Delta\rho_{\max}$ before and after calibration

Group	1	2	3
$\Delta\rho_{\max}$ (before) [mm]	16.901	8.326	5.448
$\Delta\rho_{\max}$ (after) [mm]	0.847	0.623	0.825

8 CONCLUSIONS

To realize the rapid and automatic zero offset calibration of a 2-DOF parallel robot, a measuring mechanism is designed, and based on which a zero-offset calibration method is proposed in this paper. Compared with large measurement devices, the measuring mechanism is more convenient to use and it can make the measurements in a time and cost-effective manner. By using the TSVD method, the nonlinear ill-conditioning problem of the identification model can be solved. The identification model modified with the former identification result of the MAEMM can help to improve the identifiability of the zero offsets. The optimization approach for selecting measurement positions is able to maximize the measurement efficiency and further improve the identifiability. The simulation and experimental results of the calibration show that the identification model has good identifiability and robustness, and the position error after calibration can be significantly reduced. The proposed measuring mechanism and zero offset calibration method are also useful for the kinematic calibration of other planar or spatial parallel robots. It should be noted that since the spatial parallel

robots usually have cylindrical workspaces, if the measuring mechanism is used for the calibration of these parallel robots, its two revolute joints should be replaced by universal or spherical joints, so that the measurement positions can be more reasonably selected in those cylindrical workspaces.

9 ACKNOWLEDGEMENTS

This work is supported by the National Natural Science Foundation of China (Grant No. 51475320 and 51420105007), and the Key Technologies R & D Program of Tianjin (Grant No. 15ZXZNGX00220).

10 REFERENCES

- [1] Clavel, R. (1988). Delta, a fast robot with parallel geometry. *Proceedings of the 18th International Symposium on Industrial Robots*, p. 91-100.
- [2] Pierrot, F., Nabat, V., Company, O., Krut, S., Poignet, P. (2009). Optimal design of a 4-DOF parallel manipulator: From academia to industry. *IEEE Transactions on Robotics*, vol. 25, no. 2, p. 213-224, DOI:10.1109/TRO.2008.2011412.
- [3] Jin, Y., Chen, I.M., Yang, G.L. (2009). Kinematic design of a family of 6-DOF partially decoupled parallel manipulators. *Mechanism and Machine Theory*, vol. 44, no.5, p. 912-922, DOI:10.1016/j.mechmachtheory.2008.06.004.
- [4] Cheng, G., Xu, P., Yang, D.H., Li, H., Liu, H.G. (2013). Analysing kinematics of a novel 3CPS parallel manipulator based on rodriques parameters. *Strojniški vestnik - Journal of Mechanical Engineering*, vol. 59, no. 5, p. 291-300, DOI:10.5545/sv-jme.2012.727.
- [5] Hao, G.B., Yu, J.J. (2016). Design, modelling and analysis of a completely-decoupled XY compliant parallel manipulator. *Mechanisms and Machine Theory*, vol. 102, p. 179-195, DOI:10.1016/j.mechmachtheory.2016.04.006.
- [6] Hao, G.B., Kong, X.W. (2012). A novel large-range XY compliant parallel manipulator with enhanced out-of-plane stiffness. *Journal of Mechanical Design*, vol. 134, no. 6, p. 061009-1-061009-9, DOI:10.1115/1.4006653.
- [7] Huang, T., Liu, S.T., Mei, J.P., Chetwynd, D.G. (2013). Optimal design of a 2-DOF pick-and-place parallel robot using dynamic performance indices and angular constraints. *Mechanisms and Machine Theory*, vol. 70, p. 246-253, DOI:10.1016/j.mechmachtheory.2013.07.014.
- [8] Cammarata, A. (2015). Optimized design of a large-workspace 2-DOF parallel robot for solar tracking systems. *Mechanisms and Machine Theory*, vol. 83, p. 175-186, DOI:10.1016/j.mechmachtheory.2014.09.012.
- [9] Choi, Y., Cheong, J., Jin, H.K., Do, H.M. (2016). Zero-offset calibration using a screw theory. *International Conference on Ubiquitous Robots and Ambient Intelligence*, p. 526-528, DOI:10.1109/URAI.2016.7625770.
- [10] Sun, Y.H., Wang, L., Mei, J.P., Zhang, W.C., Liu, Y. (2013). Zero calibration of delta robot based on monocular vision. *Journal of Tianjin University*, vol. 46, no. 3, p. 239-243. (in Chinese)
- [11] Jáuregui, J.C., Hernández, E.E., Ceccarelli, M., López-Cajun, C., García, A. (2013). Kinematic calibration of precise 6-DOF Stewart platform-type positioning systems for radio telescope applications. *Frontiers of Mechanical Engineering*, vol. 8, no. 3, p. 252-260, DOI:10.1007/s11465-013-0249-7.
- [12] Jin, Y., Chen I.M. (2006). Effects of constraint errors on parallel manipulators with decoupled motion. *Mechanism and Machine Theory*, vol. 41, no. 8, p. 912-928, DOI:10.1016/j.mechmachtheory.2006.03.012.
- [13] Pan, B.Z., Song Y.M., Wang P.F., Dong, G., Sun, T. (2014). Laser tracker based rapid home position calibration of a hybrid robot. *Journal of Mechanical Engineering*, vol. 50, no. 1, p. 31-37, DOI:10.3901/JME.2014.01.031. (in Chinese)
- [14] Cheng, G., Gu, W., Li, J., Tang, Y.P. (2011). Overall structure calibration of 3-UCR parallel manipulator based on quaternion method. *Strojniški vestnik - Journal of Mechanical Engineering*, vol. 57, no. 10, p. 719-729, DOI:10.5545/sv-jme.2010.167.
- [15] Last, P., Budde, C., Hesselbach, J. (2005). Self-calibration of the HEXA-parallel-structure. *IEEE International Conference on Automation Science and Engineering*, p. 393-398, DOI:10.1109/COASE.2005.1506801.
- [16] Majarena, A.C., Santolaria, J., Samper, D., Aguilar, J.J. (2010). An overview of kinematic and calibration models using internal/external sensors or constraints to improve the behavior of spatial parallel mechanisms. *Sensors*, vol. 10, no. 11, p. 10256-10297, DOI:10.3390/s101110256.
- [17] Rauf, A., Pervez, A., Ryu, J. (2006). Experimental results on kinematic calibration of parallel manipulators using a partial pose measurement device. *IEEE Transactions on Robotics*, vol. 22, no. 2, p. 379-344, DOI:10.1109/TRO.2006.862493.
- [18] Kovac, I., Klein, A. (2002). Apparatus and a procedure to calibrate coordinate measuring arms. *Strojniški vestnik - Journal of Mechanical Engineering*, vol. 48, no. 1, p. 17-32.
- [19] Cedilnik, M., Sokovic, M., Jurkovic, J. (2006). Calibration and checking the geometrical accuracy of a CNC machine-tool. *Strojniški vestnik - Journal of Mechanical Engineering*, vol. 52, no. 11, p. 752-762.
- [20] Takeda, Y., Gang S., Funabashi, H. (2004). A DBB-based kinematic calibration method for in-parallel actuated mechanism using a Fourier series. *Journal of Mechanical Design*, vol. 126, no. 5, p. 856-865, DOI:10.1115/1.1767822.
- [21] Tian, W.J., Yin, F.W., Liu, H.T., Li, J.H., Li, Q., Huang, T., Chetwynd, D.G. (2016). Kinematic calibration of a 3-DOF spindle head using a double ball bar. *Mechanism and Machine Theory*, vol. 102, p. 167-178, DOI:10.1016/j.mechmachtheory.2016.04.008.
- [22] Hoerl, A.E., Kennard, R.W. (2000). Ridge regression: biased estimation for nonorthogonal problems. *Technometrics*, vol. 42, no. 1, p. 80-86, DOI:10.1080/00401706.2000.10485983.
- [23] Hansen, P.C., O'Leary, D.P. (1993). The use of the L-curve in the regularization of discrete ill-posed problems. *SIAM Journal on Scientific Computing*, vol. 14, no. 6, p. 1487-1503, DOI:10.1137/0914086.
- [24] Yang, Z.Y., Wu, J., Mei, J.P. (2007). Motor-mechanism dynamic model based neural network optimized computed torque control of a high speed parallel manipulator. *Mechatronics*, vol. 17, no. 7, p. 381-390, DOI:10.1016/j.mechatronics.2007.04.009.

A Novel Robotic Neuronavigation System: RONNA G3

Marko Švaco^{1,2,*} – Bojan Šekoranja^{1,2} – Filip Šuligoj^{1,2} – Josip Vidaković^{1,2} – Bojan Jerbić^{1,2} – Darko Chudy^{3,4}

¹ University of Zagreb, Faculty of Mechanical Engineering and Naval Architecture, Croatia

² University Hospital Dubrava, Associate at the Department of Neurosurgery, Croatia

³ University Hospital Dubrava, Department of Neurosurgery, Croatia

⁴ University of Zagreb, School of Medicine, Croatian Institute for Brain Research, Croatia

This paper presents a novel robotic neuronavigation system, RONNA G3, developed for frameless stereotactic navigation based on standard industrial robots. The basic version of the RONNA G3 system has three main components: a robotic arm on a universal mobile platform, a planning system, and a navigation system. We have developed a stereovision localization device (RONNAstereo) that can be attached to the robot end effector for accurate non-contact localization of the patient in the operating room. RONNAstereo has two infrared (IR) cameras with macro lenses aligned at a 55° angle in the same plane. We have evaluated the application accuracy of the RONNA G3 system in a phantom study with two different registration methods. The first registration method involves a rigid fiducial marker with four retroreflective spheres (spherical fiducials). The second method uses freely distributed individual spherical fiducials mounted on single bone screws. We have evaluated the RONNA G3 positioning error for superficial (< 50 mm) and deep (50 mm to 120 mm) targets. The mean target positioning error (TPE) of the RONNA G3 system for superficial and deep targets was 0.43 mm (interquartile range 0.22 mm to 0.60 mm) and 0.88 mm (interquartile range 0.66 mm to 1.10 mm), respectively. Given the positioning errors from the phantom trials, we have prepared the system for clinical trials, which are currently in progress.

Keywords: robotic neuronavigation, frameless stereotaxy, minimally invasive surgery, RONNA G3

Highlights

- An overview of standard industrial robots used for neuronavigation.
- A novel dual-arm robotic neuronavigation system, RONNA G3, based on standard industrial robots.
- A novel stereovision localization device developed for accurate non-contact localization of the patient in the operating room.
- RONNA G3 accuracy evaluation in a phantom study.

0 INTRODUCTION

Since its introduction into human neurosurgery by Spiegel and Wycis almost 70 years ago, the stereotactic frame has been used as a standard targeting method for functional intracranial procedures, biopsies, and deep brain stimulation [1]. With advances in image-guided neurosurgical procedures over the past 30 years, alternative methods of performing surgical interventions have become more widely used by neurosurgeons [2] to [5]. The first application of a robot in medicine was in the field of neurosurgery when an industrial robot, PUMA 200, was successfully used in a frame-based configuration for a brain biopsy procedure in 1985 [6]. There are a few reasons that the first application of robotic technology was in the field of neurosurgery. As noted in [7], the human brain is an organ which is uniquely suited for robotic applications. It is symmetrically confined within a rigid container (the skull), which offers the potential of accurate patient localization by a robotic or external localization system.

One of the greatest obstacles to the widespread robotization of neurosurgical procedures is the total cost of robotic systems, which remain very high [8].

One example is the Neuromate stereotactic robot (Renishaw, Gloucestershire, UK) [9]. The R&D costs are estimated at over 30 million US dollars [10]; this fact contributes to the higher price of this system. Another example is the Renaissance system (Mazor Robotics Ltd., Caesarea, Israel) which has a total system cost of 789,000 US dollars [11]. This cost includes the robot, an instrument tray, a dedicated workstation and a year of free technical support. Therefore, it is necessary for hospitals to ensure that the benefits brought by robotic surgery outweigh the costs.

In contrast, standard industrial robots come in a wide range of kinematic configurations (serial-link manipulators with six or seven revolute joints) and robot reach specifications that make them suitable for a wide variety of applications in neurosurgery.

Table 1 gives an overview of standard industrial robots that have been implemented as part of commercial or research neuronavigation robotic systems since the year 2000. One benefit of implementing industrial robots is that the research and development of the robotic arm have been done by the robot manufacturer, contributing to a lower overall system price. Regarding strict medical regulations and

*Corr. Author's Address: University of Zagreb, Faculty of Mechanical Engineering and Naval Architecture, Ivana Lučića 5, Zagreb, Croatia, marko.svaco@fsb.hr

standards, which are indicated in [12], one alternative to standard industrial robots is robot manipulators certified as medical devices. An example of that alternative is the newly developed Kuka LBR Med medical lightweight robot (KUKA, Augsburg, Germany). As presented by the KUKA Healthcare robotics division [13], the LBR Med lightweight robot will be tested in accordance with IEC 60601-1, the technical standards for the safety and effectiveness of medical electrical equipment. The robot will be distributed with a CE label for EMC (IEC 60601-1-2:2014), which will ensure an even easier integration into medical devices. Despite this fact, standard industrial robots that are incorporated in the AQRATE system (KB Medical SA, Lausanne, Switzerland) [14], the ROSA Spine (Medtech, Montpellier, France) [15], and the ROSA Brain (Medtech) [16] have obtained both the CE mark and the FDA approval. This fact confirms the medical applicability of standard industrial robots as part of medical devices (details are given in Table 1).

Since 2015, four innovative robotic neuronavigation systems have been developed based on standard industrial robots from KUKA [14], Stäubli [15] and Universal robots [18] to [20] (details are given in Table 1). These systems are not included in the current state-of-the-art literature survey and review papers [29] to [32]; this demonstrates the very rapid development of the field of robotized neuronavigation medical.

The development of a novel robotic neuronavigation system, RONNA G3, based on standard industrial robots. We have validated the

RONNA G3 system in an *in vitro* phantom trial which showed application accuracies suitable for the application in human clinical trials. At the end of the paper, we present a workflow for robotized stereotactic brain biopsy procedures that are currently being conducted as part of the clinical trials with the RONNA G3 system at the Department of Neurosurgery, University Hospital Dubrava, Croatia. We have received the approval of the Ethical Committee of the University Hospital Dubrava and the School of Medicine, University of Zagreb, and we have been given consent from each patient included in the clinical trials.

1 THE RONNA G3 SYSTEM

We have extensively upgraded the previously developed RONNA system [23]. That system was tested through rigorous preclinical trials which resulted in numerous improvements and in the development of the new RONNA G3 system.

RONNA G3 (Figs. 1 and 2) is designed and used for stereotactic neuronavigation procedures. The RONNA G3 system consists of a robotic arm mounted on a specially designed universal mobile platform, a global Optical Tracking System (OTS), and planning software. A localization feature (rigid fiducial marker or freely distributed bone mounted fiducials, shown in Fig. 3) is used for the patient registration, while a stereovision system (RONNAstereo) is used for the patient localization in the physical space. The robots are equipped with surgical tools (guides, grippers, drill, etc.). A specific characteristic of the RONNA

Table 1. Overview of industrial robots used for neuronavigation since the year 2000

System (project)	Selected papers	Robot Manufacturer	Model	Robot Repeatability [mm]	Payload [kg]
ROSA Spine	[15] Lefranc and Peltier [17] Chenin et al.	Stäubli	TX60L	±0.030	2
Aqrate	[14] Patel	KUKA	KR6 R700	±0.030	6
REMEBOT	[18] Liu Yu-peng et al.	Universal robots	UR5	±0.100	5
TIRobot	[19] Tian et al. [20] Tian	Universal robots	UR5	±0.100	5
not specified	[21] Faria et al.	Yaskawa Motoman	MH5	±0.020	5
Active project	[22] Beretta et al.	KUKA	LWR4+	±0.100	7
RONNA	[23] Jerbić et al.	KUKA	KR6R900	±0.030	6
ROSA Brain	[16] Lefranc et al. [3] González-Martínez et al.	Mitsubishi	RV3SB	±0.020	3
ROBOCAST	[24] Comparetti et al.	Adept	Viper s1300	±0.070	5
OrthoMIT	[25] Tovar-Arriaga et al.	KUKA/DLR	LWR3	±0.150	14
Pathfinder	[26] Deacon et al. [7] Eljamel	Adept	Viper s1300	±0.070	5
RobaCKa	[27] Eggers et al.	Stäubli	RX90	±0.025	6
CASPAR	[28] Burkart et al.	Stäubli	RX90	±0.025	6

G3 system with respect to the most current state-of-the-art robotic neurosurgical systems [29] to [32] is an additional mobile platform equipped with a compliant and sensitive robotic arm which makes it a dual-arm robot system (master and assistant robots). The robots are standard six degree-of-freedom (DOF) revolute robots. This enables full flexibility and reorientations around operative trajectories defined with five parameters (three translations and two rotations).

The system design and functional requirements in neurosurgical robotics are much more demanding than in conventional robotics, e.g. in industrial applications. First, the robotic system must be compact enough to fit in the Operating Room (OR) and should not interfere with the procedure of medical staff. On the other hand, the robotic system must meet complex requirements in terms of spatial working ability. Therefore, the robot system setup was designed using CAD software which enabled modelling and simulations [33] and [34]. Various trajectories and surgical instruments involved in neurosurgery were explored, as well as the requirements to be met regarding the location of the whole system in the operating room in relation to other equipment and medical staff.

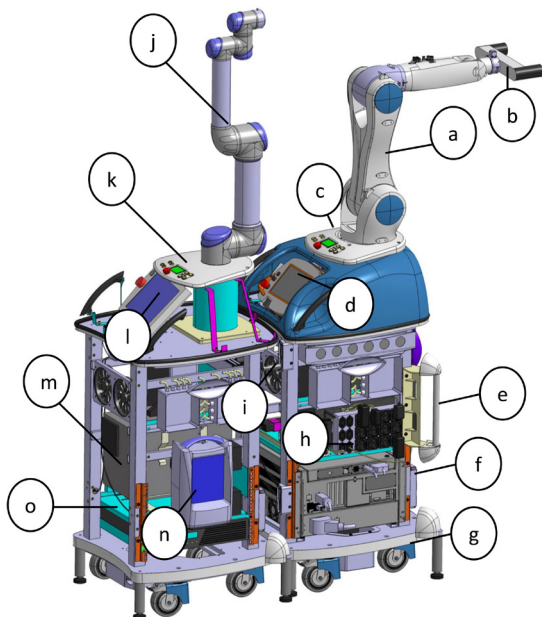


Fig. 1. The main components of the RONNA G3 robot platforms: (a) Master robot – Kuka KR6 R900, (b) RONNAstereo, (c) Control panel, (d) Master robot teach pendant, (e) mechanical link for the operating table, (f) Master robot controller, (g) hydraulic lifting system, (h) UPS (Uninterruptible Power Supply), (i) cooling system, (j) Assistant robot – Universal robotics UR5, (k) Control panel, (l) Assistant robot teach pendant, (m) Assistant robot controller, (n) High-speed medical drill control system, (o) UPS

Since the RONNA G3 provides a dual-arm configuration, a special algorithm is applied to control the movement of two robots. The control algorithm is used to calculate optimal joint configurations of both robots in mutual target operation points by assuring the high dexterity of each robot and preventing collision between them. The algorithm calculates the robot configurations in the joint space based on a multi-objective cost function (Q) composed of three criteria: the condition number (c), Joint Limit Avoidance (JLA), and collision avoiding criteria (d) based on utilizing the roll angle of the trajectory:

$$\min_{robot\ configurations \in joint\ space} Q(c, JLA, d). \quad (1)$$

Parameters c and JLA are concerned with the dexterity of the robots, while d assures the collision-free cooperation of robots. Robot configurations are input vectors containing angular displacements of joints for both robots. These input vectors are obtained by searching the entire range of possible joint states of the robots (joint space). Each operational target point requires the computation of optimal joint configurations based on Eq. (1).

RONNA G3 is designed to work in a single robot mode or in a dual-arm mode, depending on the type of surgery and the surgeon's choice. In both cases, the patient should be under anaesthesia with the head fixed in a head holder (Mayfield clamp). The master robot is used for accurate routing of surgical instruments (drill, needle, or any other instrument) to the planned position and in the desired orientation. Insertion of the instrument in the direction of the operation point can be done by the assistant robot or by the neurosurgeon. When the operation is performed only with the master robot, the robot is used only as a navigation instrument (guide).

The extended version of RONNA G3 which uses both robotic arms is intended for automated robotic bone drilling applications and manipulation of surgical instruments. The assistant robot inserts the operating instrument into the tool guide pointing toward the operation point. In addition, the assistant robot is intended for assisting the surgeon through intuitive human-robot collaboration [35].

For the global navigation in the OR, the OTS uses an infrared stereo camera (Polaris Spectra, NDI - Northern Digital Inc., Ontario, Canada) and two reference frames, one attached to the patient and the other to the robotic arm. The OTS is only used for coarse positioning of the robot with respect to the patient in the global localization phase of the procedure. In our previous study [36], we measured

the main accuracy categories of the robot system guided with an OTS. When using relative referencing and two reference frames (markers), the root-mean-square positioning error of the OTS was 0.398 mm and showed a strong growth tendency with larger distances between the two markers. We have developed a localization device (RONNAstereo) which eliminates any errors that may arise from the low resolution and a wide field of view of the global OTS [36]. The RONNAstereo is described in Section 1.1.2.

1.1 Patient Registration

Patient registration implies determining a spatial transformation between coordinate systems of the medical diagnostic images (CT scan) and the patient. In the patient registration process, the RONNA G3 can use two different marker types: a rigid fiducial marker with four standard medical retroreflective spheres (spherical fiducials) shown in Fig. 3a or freely distributed individual spherical fiducials mounted on individual bone screws (Figs. 3b and c).

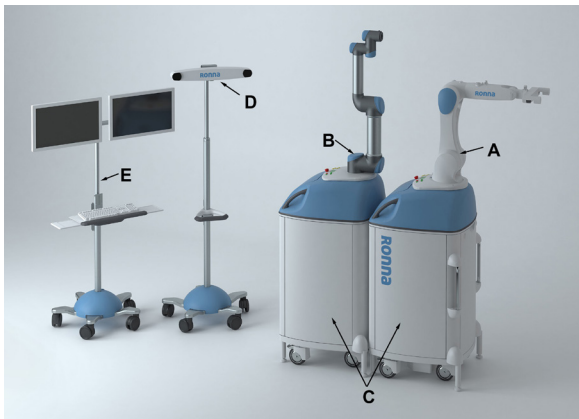


Fig. 2. The RONNA G3 system (render): (A) master robot, (B) assistant robot, (C) universal mobile platform, (D) optical tracking system, (E) control and planning software interface

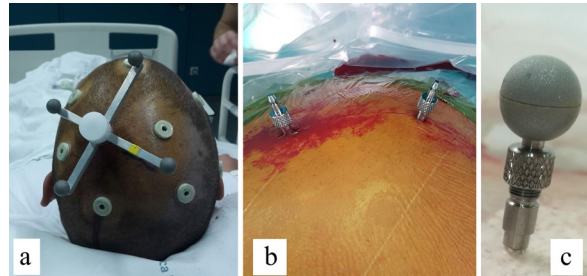


Fig. 3. RONNA registration methods: a) rigid fiducial marker, b) two freely distributed bone screws, and c) a bone screw with the spherical fiducial mounted on its top

In both cases, individual spherical fiducials need to be localized in the image space and the physical space with a minimum of three spherical fiducials that are positioned at the same distance from each other.

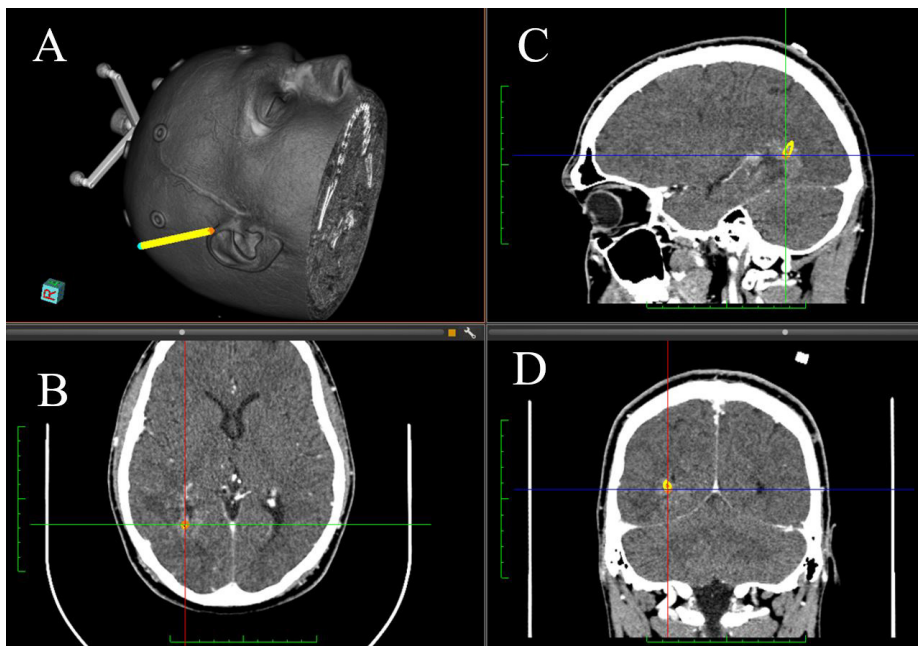


Fig. 4. RONNA planning software (RONNAplan) – the target point (orange sphere) is shown in the: b) axial plane, c) sagittal plane, and d) coronal plane; a) the entry point (blue sphere) and the trajectory (yellow) are shown in the 3D view

The transformation is defined by a 3×3 rotation matrix and a 3D position vector that describe the position and the orientation of the image space coordinate system with respect to the physical space coordinate system. RONNAstereo is used for patient localization in the physical space, while either the developed automatic localization algorithm or manual localization is used for the localization of spherical fiducials in the image space.

The RONNA G3 system incorporates software for operation planning (RONNAplan) based on computed tomography (CT) or magnetic resonance imaging (MRI). RONNAplan and its features are developed for satisfying the needs of neurosurgical applications based on the open source medical visualization software Medinria (Inria, France). This software allows the definition of trajectories through a visual, image-based user interface that enables the selection of entry and target points. Two- and three-dimensional visualization of the planned trajectories, as well as the editing and storing of the surgical plan, are supported by this software. The generated surgical plan can be automatically transferred to the robot control software after the planning phase has been completed. An example of a surgical plan is shown in Fig. 4.

1.1.1 Image Space Localization

In the RONNA G3 surgery procedure, image space localization is conducted after the patient with the attached fiducial marker has been subjected to a CT scan. If the localization is done manually, the operator visually determines the centre of every spherical fiducial using the RONNAplan software. Manual localization has drawbacks, such as insufficient localization accuracy, long duration, and the possibility of human error. To overcome these drawbacks, we have developed an automated algorithm for the accurate localization of spherical fiducials in the image space. This localization algorithm uses a combination of machine vision algorithms, biomedical image filtration methods, and mathematical estimation methods. A pre-processing step of the localization algorithm is the intensity-based filtration of voxels. The filter isolates the space around high Hounsfield values of the titanium pins used for mounting the spherical fiducials. Since the cross-section of a spherical fiducial is a circle, an algorithm based on the circle Hough transform [37] is used for finding all the potential circles in the filtered axial and sagittal image projections. Spheres are verified, and false positive detections are removed with Euclidean distance filters. Finally, to calculate

the spherical fiducial centre from the detected circles, we implemented an algorithm that matches a set of points to algebraic surfaces using the direct least square method. Based on the measurements conducted in clinical conditions on patients and on various test phantoms, the localization algorithm has shown a higher accuracy and speed in comparison with the manual localization carried out by human operators. The algorithm showed 100 per cent reliability with successful localizations of the fiducial marker in twenty test cases.

1.1.2 Physical Space Localization

Physical space localization is automated with an OTS. The OTS can detect spherical fiducials located on the robotic arm and the patient simultaneously, as shown in Fig. 5. When a relative spatial relation between the robot coordinate system and the patient coordinate system is established, the robot uses the stereovision localization device (RONNAstereo) for accurate localization. RONNAstereo consists of two infrared cameras (acA2000-50gmNIR, Basler, Ahrensburg, Germany) with macro lenses aligned at a 55° angle in the same plane. The RONNAstereo was considerably improved with respect to its initial version presented in [23]. By determining the position of a corresponding point in both images, a virtual tool centre point (TCP) is defined. The virtual TCP is calibrated so that it corresponds with the TCP of a calibrated surgical tool. The robot TCP coordinate system is aligned within 0.05 mm using the RONNAstereo TCP and the physical tip of the surgical tool. The stereovision images are processed using machine vision software running the least-squares circular edge fit algorithm [37] and contrast enhancement [38] that actively determine the position of a localized spherical fiducial with respect to the robot's TCP. The system allows the positioning of the robot's TCP within 0.03 mm off a detected spherical fiducial centre. To the best of our knowledge, the developed localization device (RONNAstereo), which is held by our robot during the patient localization, is a novelty in the field of robotic neuronavigation systems and their noncontact frameless localization techniques. The ROSA robot [16] (Medtech, Montpellier, France) in the frameless mode uses a laser measurement device for surface scanning of the patient, while the Neuromate robot [39] (Renishaw, Gloucestershire, UK) uses an ultrasound localizer (transmitter and receiver). The Pathfinder robot [40] (Prosurgics Ltd., High Wycombe, UK) used a single camera attached to the robot end effector for patient localization.

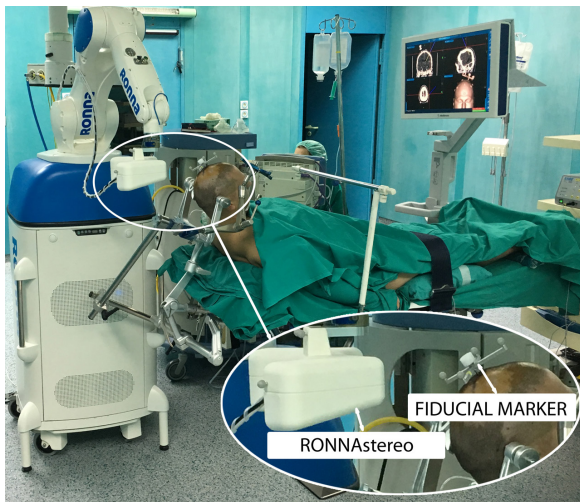


Fig. 5. Physical space patient localization

2 EXPERIMENTAL SETUP - PHANTOM TRIALS

In the *in vitro* accuracy evaluation, the positioning accuracy of RONNA G3 was measured on a test phantom (Fig. 6.). The test phantom consists of a polymer base with one central pillar, 16 randomly distributed spherical fiducials, and a rigid fiducial marker. The centre of each spherical fiducial can be used as a target point. Accuracy measurements based on phantoms with spherical targets are commonly used to assess *in vitro* positioning accuracy of robotic neurosurgical systems. An overview of phantom designs used for the testing of various robotic neuronavigation systems is given in Table 2. In our

previous research, we evaluated a number of different phantom target designs [41].

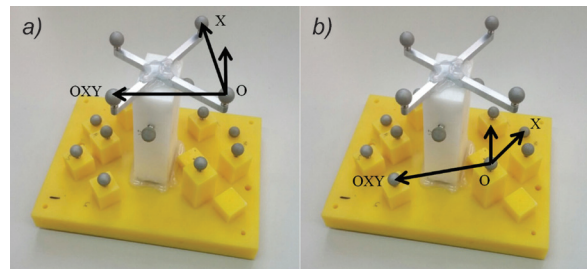


Fig. 6. The test phantom; a) a rigid fiducial marker attached to the phantom, b) three randomly distributed spherical fiducials mounted via individual bone screws, which define the phantom coordinate frame

We obtained three CT scans (Somatom Emotion®, Siemens, Erlangen, Germany) of our phantom. Each scan contained a different number of slices: CT1 - 283 slices, CT2 - 357 slices, and CT3 - 358 slices. Each scanning orientation was completely different in respect to the scanning plane. We used our standard head protocol: gantry rotation time 0.6 s, helical scanning, detector collimation 16 mm × 0.6 mm, slice width 0.75 mm, reconstruction increment 0.7 mm, image matrix 512 × 512 with a voxel size of 0.5 mm × 0.5 mm × 0.7 mm, no gantry.

We evaluated both registration methods by registering each CT scan from the image space in the physical space. In the first case, we used the rigid fiducial marker attached to the phantom (Fig. 6a) to define the phantom coordinate frame. In the second

Table 2. Phantom accuracy studies

Study	Year	Test system	Phantom features
Willems et al. [42]	2001	Mehrkoordinaten manipulator (MKM) robotic navigation system	<ul style="list-style-type: none"> A circular plate made of acrylic plastic with 19 orthogonally positioned acrylic plastic rods. Each target can be defined either as the centre of the sphere or the centre of the dimple in the rod tip for improving accuracy.
Morgan et al. [43]	2003	Pathfinder Neurosurgical robot	<ul style="list-style-type: none"> Re-locatable spherical targets and a removable cylindrical surface to simulate the skin. Perspex spheres on rods are attached to a base plate. simulates the range of target position throughout the adult brain.
Liu et al. [44]	2006	NeuroMaster	<ul style="list-style-type: none"> 26 pillars fixed on an aluminium plate similar in size to a human head. A plastic sphere is positioned on the top of each pillar. Among the 26 spheres, four are selected to simulate the markers positioned on the patient's head, and the others are the targets.
Chan et al. [45]	2009	Neuroscience Institute Surgical System	<ul style="list-style-type: none"> Perspex phantom with 12 alumina-oxide spheres on stalks of varying lengths as targets.
Schouten et al. [46]	2010	Novel robotic needle guide manipulator	<ul style="list-style-type: none"> Plastic spheres located in agar represented targets. All spheres were embedded in the agar at the same depth of 3 cm, with a distance of 2 cm to 3 cm between them.
Kajita et al. [47]	2015	NeuroMate™ robot system	<ul style="list-style-type: none"> A standard plastic phantom with metal target spheres

case, we used three randomly distributed spherical fiducials mounted via individual bone screws (Fig. 6b) to define the phantom coordinate frame. In clinical practice, the second method allows for a variation in the marker size and allows for the coordinate registration system to be closer to the target points.

Target positions in the image space of the spherical fiducials are obtained using the sphere extraction algorithm presented in the patient registration section in all three CT scans. The localized spherical fiducial centres and one planned trajectory are shown in Fig. 7 within the RONNAplan interface.

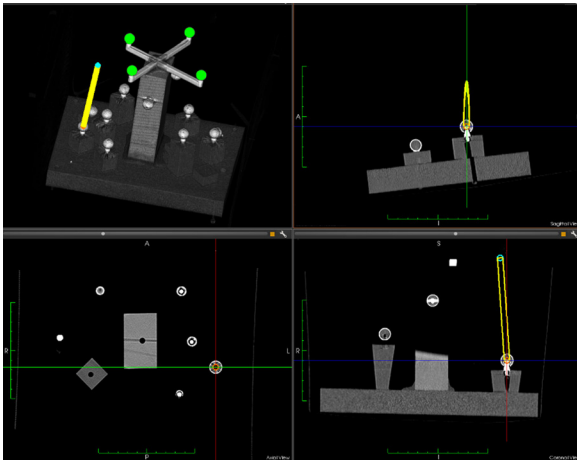


Fig. 7. RONNA planning software (RONNAplan); green spheres depict automatically localized spherical fiducials of the rigid marker; the planned trajectory is shown in yellow; the entry point is shown in blue, and the target position is shown in orange

For accurate measurement, the robot used RONNAstereo to position its virtual TCP within 0.03 mm off each spherical fiducial centre. As shown in Fig. 6, three spherical fiducials were used for determining the phantom coordinate system in the image space and the physical space. After the phantom is localized, the virtual TCP of the robot is positioned at the calculated coordinates of the spherical targets denoted as \mathbf{p}_i . The robot's position is corrected afterward to the exact centre \mathbf{p}_c of each spherical fiducial with the previously described circular edge detection algorithm. The robot positioning error is calculated as the Euclidian distance between the initial position \mathbf{p}_i and the corrected position \mathbf{p}_c of the virtual TCP of the robot.

$$\text{error} = \sqrt{(x_i - x_c)^2 + (y_i - y_c)^2 + (z_i - z_c)^2}, \quad (2)$$

where x_c , y_c and z_c are the corrected position coordinates in the x , y and z direction in the RONNAstereo coordinate frame.

We obtained target positioning errors (TPE) for 10 random phantom positions and orientations in the robot workspace. We repeated the measurement for each of the three CT scans. To obtain valid TPE data, the spherical fiducials that form the localization coordinate system were left out in both cases because they do not contain the full CT localization error. Also, three unreachable (not visible) target points were neglected. Finally, the experiment yielded 10 usable target points. In total, 300 position measurements were conducted.

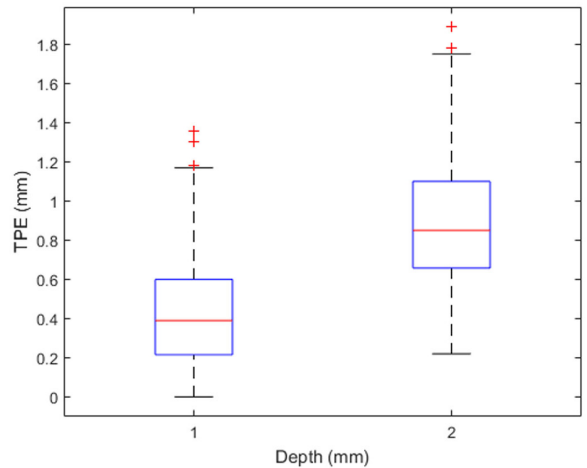


Fig. 8. Positioning error for superficial (1) and deep targets (2)

Table 3. Accuracy of the RONNA system

Target group	Depth [mm]	Mean error [mm]	Standard deviation [mm]	Maximum error [mm]
1	<50	0.43	0.27	1.36
2	50 to 120	0.88	0.37	1.89
1, 2	0 to 120	0.65	0.39	1.89

Furthermore, kinematic calibration of the robot was performed to determine its TCP [48]. It is carried out by targeting a point in the robot workspace in multiple different orientations. Using the joint configurations from the same spatial point, an optimization of the TCP coordinates is performed by minimizing the residuals of the end effector poses, as shown in [49]. Other kinematic parameters of the robot are not altered.

The absolute positioning accuracy of the RONNA G3 system is shown in Fig. 8 and in Table 3. Targeting errors are shown for two different target groups: superficial (1) and deep (2). This classification is related to the z -coordinate of the target in the coordinate system of the rigid fiducial marker or in the coordinate system of freely distributed individual

spherical fiducials. Significant differences between the superficial and the deep targets regarding the positioning accuracy can be observed both in the values of the mean (0.43 mm and 0.88 mm) and maximum errors (1.36 mm and 1.89 mm). Accuracies with errors of less than 0.5 mm, which satisfy the stereotactic procedure requirements, can be achieved if the target points are close to the marker coordinate system (<50 mm), i.e. with superficial target points.

It should be noted that the conducted phantom trial does not consider several factors influencing the overall accuracy occurring in *in vivo* applications [50]. These factors include inaccuracies of the surgical instruments (e.g. a slight curvature of the biopsy needle), the brain shifting during bone drilling, and other surgery-related specific effects. Furthermore, the phantom trial underestimates errors that can arise from the patient movement, the patient-dependent distortion of the image and the difficulties in identifying the position of the biological target rather than the fiducial target [39]. Thus, it can be expected that the absolute accuracy in future clinical trials will be degraded due to the above listed factors. This has already been confirmed by recent clinical case studies with the Neuromate [2] and ROSA [3], [16] robotic systems.

3 SURGICAL WORKFLOW ASSISTED WITH THE RONNA G3 SYSTEM

The RONNA G3 clinical procedure is divided into three phases: preoperative phase (I), preparation phase (II), and operation phase (III).

In the preoperative phase (I), either the bone attached marker or distributed bone screws are fixed to the patient's head under local anaesthesia. The day before the surgery, the patient is subjected to a CT scan. After that, the marker is removed from the bone screw to reduce the patient's discomfort. In the next step, the surgeon imports the medical diagnostic images into the RONNAplan software. The surgeon plans and defines all necessary operation points and trajectories (defined with accompanying entry points) while the spherical fiducials are localized automatically.

In the preparation phase (II), the patient is brought to the OR. The patient is given general anaesthesia, and his head is fixed in a head holder (Mayfield clamp). The marker is reattached to the bone screw, or the freely distributed individual spherical fiducials are attached to single bone screws. To obtain the initial patient position in the OR, the robot platform position is adjusted to the patient according to the planning

module algorithm (1) and the position is verified with the OTS. The robot platform is then fixed to the operating table to ensure stability and rigidity of the entire setup. The system proceeds to the accurate marker localization using RONNAstereo, as described in section 1.1.2. After localization and registration, RONNAstereo is removed from the robot end effector and replaced with a tool guide. The surgeon then verifies the localization procedure using the tool guide to point at anatomical landmarks on the patient's head.

In the operation phase (III), the operating field is washed by alcohol and a sterile cover is put on the patient and on the robot. A sterile set of end effector tools is used. Using RONNAplan, the surgeon selects the preoperatively planned trajectory and the robot positions the tool guide accordingly. In this phase of clinical trials, the system is used for brain tissue biopsies. The robot is equipped with a sterile tool holder for a twist drill (3.2 mm in diameter) and a biopsy needle (2.5 mm in diameter). Skin incision and drilling of the burr hole are performed by the neurosurgeon. After the dura has been opened and coagulation has been performed, a 2.5 mm diameter biopsy needle is advanced to the target and staged biopsy is performed. When the surgeon completes the biopsy at the target point, the robot can retract to its home position or reposition at another target.

4 CONCLUSIONS

There are numerous advantages of the application of robotic technology in neurosurgery. Endurance is the first benefit of robotics given that several studies have demonstrated that surgeons suffer from muscle fatigue during operations as a result of the procedure duration and the need to hold surgical instruments at specific angles [40]. By using a robotic arm to steady the surgical instrument, the problems of fatigue and tremor can be eliminated. Robots are also able to extend the visual and manual dexterity of neurosurgeons beyond their limits as pointed out by Eljamel [7] because they can work through very narrow and long surgical corridors most suited for brain surgery. Apart from the frameless approach, neurosurgical robotic systems can provide a number of advantages for the surgical procedure, such as the elimination of tremor, lower risk of error due to the surgeon's fatigue and faster completion of the operation.

RONNA G3 is a novel neuronavigation robotic system, intended to be used as a sophisticated tool by neurosurgeons for intraoperative planning and accurate frameless neuronavigation. Some of the advantages of the frameless over the frame-based

techniques are the ease of use, less patient discomfort, and more flexible pre-operative planning with the ability to separate the imaging from the surgical procedure, which provides ample time for a detailed image analysis and trajectory planning [39] and [51]. We have evaluated the application accuracy of the RONNA G3 system in a phantom study with two different registration methods. The first registration method involves a rigid fiducial marker with four spherical fiducials. The second method uses randomly distributed spherical fiducials mounted on individual bone screws. The mean positioning error for superficial targets (< 50 mm) was 0.43 mm (interquartile range 0.22 mm to 0.60 mm) and for deep targets (50 mm to 120 mm), it was 0.88 mm (interquartile range 0.66 mm to 1.10 mm). Given the positioning errors obtained from the phantom trials, we have prepared the system for clinical trials which are currently in progress. The RONNA G3 system has two key features that differentiate it from current robotic neuronavigation systems used for neurosurgical interventions. The first key feature of our system is a specially designed universal mobile platform that can be used for different robot types. The second feature is a new high precision non-contact localization system, RONNAstereo. Furthermore, RONNA G3 utilizes a novel automatic localizing algorithm [52] developed for improved preoperative spherical fiducial localization.

In future work, we plan to evaluate the clinical application accuracy of the RONNA G3 system for frameless stereotactic brain biopsy procedures. In the prospective clinical study using the RONNA G3 system, in addition to reporting the target point error and accuracy measurements, we plan to report other measuring metrics; these will include diagnostic yield, operating time, and intraoperative and postoperative complications. In addition, we are working on the development and testing of bone drilling procedures on animal bone specimens using a second robot, as well as on task planning algorithms for increasing the robot autonomy [53] and [54].

5 ACKNOWLEDGEMENTS

The authors would like to acknowledge the support of the Croatian Scientific Foundation through the research project ACRON - A new concept of Applied Cognitive Robotics in clinical Neuroscience. The authors would like to thank Domagoj Dlaka, Fadi Almahariq, and Dominik Romić from the University Hospital Dubrava for their support in the development and evaluation phases of the RONNA G3 system.

6 REFERENCES

- [1] Henderson, J.M., Holloway, K.L., Gaede, S. E., Rosenow, J.M. (2004). The Application accuracy of a skull-mounted trajectory guide system for image-guided functional neurosurgery. *Computer Aided Surgery*, vol. 9, no. 4, p. 155-160, DOI:10.3109/10929080500050249.
- [2] Cardinale, F., Cossu, M., Castana, L., Casaceli, G., Schiariti, M.P., Miserocchi, A., Fuschillo, D., Moscato, A., Caborni, C., Arnulfo, G., Lo Russo, G. (2013). Stereoelectroencephalography: surgical methodology, safety, and stereotactic application accuracy in 500 procedures. *Neurosurgery*, vol. 72, no. 3, p. 353-366, DOI:10.1227/NEU.0b013e31827d1161.
- [3] González-Martínez, J., Bulacio, J., Thompson, S., Gale, J., Smithason, S., Najm, I., Bingaman, W. (2016). Technique, Results, and complications related to robot-assisted stereoelectroencephalography. *Neurosurgery*, vol. 78, no. 2, p. 169-180, DOI:10.1227/NEU.0000000000001034.
- [4] Minchev, G., Kronreif, G., Martínez-Moreno, M., Dorfer, C., Micko, A., Mert, A., Kiesel, B., Widhalm, G., Knosp, E., Wolfsberger, S. (2017). A novel miniature robotic guidance device for stereotactic neurosurgical interventions: preliminary experience with the iSYS1 robot. *Journal of Neurosurgery*, vol. 126, no. 3, p. 985-996, DOI:10.3171/2016.1.JNS152005.
- [5] Lefranc, M., Le Gars, D. (2012). Robotic implantation of deep brain stimulation leads, assisted by intra-operative, flat-panel CT. *Acta Neurochirurgica*, vol. 154, no. 11, p. 2069-2074, DOI:10.1007/s00701-012-1445-7.
- [6] Kwok, Y.S., Hou, J., Jonckheere, E.A., Hayati, S. (1988). A Robot with improved absolute positioning accuracy for CT guided stereotactic brain surgery. *IEEE Transactions on Biomedical Engineering*, vol. 35, no. 2, p. 153-160, DOI:10.1109/10.1354.
- [7] Eljamel, M.S. (2007). Validation of the PathFinder™ neurosurgical robot using a phantom. *The International Journal of Medical Robotics and Computer Assisted Surgery*, vol. 3, no. 4, p. 372-377, DOI:10.1002/rcs.153.
- [8] Bertelsen, A., Melo, J., Sánchez, E., Borro, D. (2013). A review of surgical robots for spinal interventions. *The International Journal of Medical Robotics and Computer Assisted Surgery*, vol. 9, no. 4, p. 407-422, DOI:10.1002/rcs.1469.
- [9] von Langsdorff, D., Paquis, P., Fontaine, D. (2015). In vivo measurement of the frame-based application accuracy of the Neuromate neurosurgical robot. *Journal of Neurosurgery*, vol. 122, no. 1, p. 191-194, DOI:10.3171/2014.9.JNS14256.
- [10] Neuromate Key Features (2016). *Datasheet H-4149-0031-01*, Reinshaw, Gloucestershire.
- [11] Joskowicz, L., Shamir, R., Israel, Z., Shoshan, Y., Shoham, M. (2011). Renaissance robotic system for keyhole cranial neurosurgery: in-vitro accuracy study. *Proceedings of the Mexican Symposium on Computation and Robotics in Medicine*.
- [12] Haidegger, T., Rudas, I.J. (2015). From concept to market: surgical robot development. *Handbook of Research on Advancements in Robotics and Mechatronics*, IGI Global, Hershey, DOI:10.4018/978-1-4666-7387-8.ch010.
- [13] Cyrill von Tiesenhausen. (2016). *KUKA LBR Med Overview*, Kuka Roboter, Augsburg.

- [14] Spine Health Institute (2016). Dr. Patel Performs Groundbreaking Robotic Surgery in Switzerland, from: <http://www.thespinehealthinstitute.com/news-room/health-blog-news/dr-patel-performs-groundbreaking-robotic-surgery-in-switzerland>, accessed on 2017-06-03.
- [15] Lefranc, M., Peltier, J. (2016). Evaluation of the ROSATM spine robot for minimally invasive surgical procedures. *Expert Review of Medical Devices*, vol. 13, no. 10, p. 899-906, DOI:10.1080/17434440.2016.1236680.
- [16] Lefranc, M., Capel, C., Pruvot, A. S., Fichten, A., Desenclos, C., Toussaint, P., Le Gars, D., Peltier, J. (2014). The Impact of the reference imaging modality, registration method and intraoperative flat-panel computed tomography on the accuracy of the ROSA® stereotactic robot. *Stereotactic and Functional Neurosurgery*, vol. 92, no. 4, p. 242-250, DOI:10.1159/000362936.
- [17] Chenin, L., Peltier, J., Lefranc, M. (2016). Minimally invasive transforaminal lumbar interbody fusion with the ROSATM spine robot and intraoperative flat-panel CT guidance. *Acta Neurochirurgica*, vol. 158, no. 6, p. 1125-1128, DOI:10.1007/s00701-016-2799-z.
- [18] Liu, Y.P., Tian, Z.-M., Hui, R. (2016). Clinical application of Remebot stereotactic surgery system without frame. *Chinese Journal of Surgery*, vol. 54, no. 05, p. 389-390 DOI:10.3760/cma.j.issn.0529-5815.2016.05.015. (in Chinese)
- [19] Tian, W., Wang, H., Liu, Y. (2016). Robot-assisted anterior odontoid screw fixation: a case report: robot-assisted odontoid screw fixation. *Orthopaedic Surgery*, vol. 8, no. 3, p. 400-404, DOI:10.1111/os.12266.
- [20] Tian, W. (2016). Robot-assisted posterior C1-2 transarticular screw fixation for atlantoaxial instability: a case report. *SPINE*, vol. 41, suppl. 19B, p. B2-B5, DOI:10.1097/BRS.0000000000001674.
- [21] Faria, C., Vale, C., Rito, M., Erhagen, W., Bicho, E. (2017). A simple control approach for stereotactic neurosurgery using a robotic manipulator. in Garrido, P., Soares, F., Moreira, A. (eds.) *Lecture Notes in Electrical Engineering*, Springer, Cham, vol. 402, p. 397-408, DOI:10.1007/978-3-319-43671-5_34.
- [22] Beretta, E., De Momi, E., Rodriguez y Baena, F., Ferrigno, G. (2015). Adaptive hands-on control for reaching and targeting tasks in surgery. *International Journal of Advanced Robotic Systems*, vol. 12, no. 5, p. 1-9, DOI:10.5772/60130.
- [23] Jerbić, B., Nikolić, G., Chudy, D., Švaco, M., Šekoranja, B. (2015). Robotic application in neurosurgery using intelligent visual and haptic interaction. *International Journal of Simulation Modelling*, vol. 14, no. 1, p. 71-84, DOI:10.2507/IJSIMM14(1)7.290.
- [24] Comparetti, M.D., Vaccarella, A., Dyagilev, I., Shoham, M., Ferrigno, G., De Momi, E. (2012). Accurate multi-robot targeting for keyhole neurosurgery based on external sensor monitoring. *Proceedings of the Institution of Mechanical Engineers, Part H: Journal of Engineering in Medicine*, vol. 226, no. 5, p. 347-359, DOI:10.1177/0954411912442120.
- [25] Tovar-Arriaga, S., Tita, R., Pedraza-Ortega, J. C., Gorrostieta, E., Kalender, W. A. (2011). Development of a robotic FD-CT-guided navigation system for needle placement-preliminary accuracy tests. *The International Journal of Medical Robotics and Computer Assisted Surgery*, vol. 7, no. 2, p. 225-236, DOI:10.1002/rcs.393.
- [26] Deacon, G., Harwood, A., Holdback, J., Maiwand, D., Pearce, M., Reid, I., Street, M., Taylor, J. (2010). The pathfinder image-guided surgical robot. *Proceedings of the Institution of Mechanical Engineers, Part H: Journal of Engineering in Medicine*, vol. 224, no. 5, p. 691-713, DOI:10.1243/09544119JEM1617.
- [27] Eggers, G., Wirtz, C., Korb, W., Engel, D., Schorr, O., Kotrikova, B., Raczkowski, J., Wörn, H., Mühling, J., Hassfeld, S., Marmulla, R. (2005). Robot-assisted craniotomy. *Minimally Invasive Neurosurgery*, vol. 48, no. 3, p. 154-158, DOI:10.1055/s-2005-870908.
- [28] Burkart, A., Debski, R.E., McMahon, P.J., Rudy, T., Fu, F.H., Musahl, V., van Scyoc, A.; L.Y. Woo, S. (2001). Precision of ACL tunnel placement using traditional and robotic techniques. *Computer Aided Surgery*, vol. 6, no. 5, p. 270-278, DOI:10.1002/igs.10013.
- [29] Faria, C., Erhagen, W., Rito, M., De Momi, E., Ferrigno, G., Bicho, E. (2015). Review of robotic technology for stereotactic neurosurgery. *IEEE Reviews in Biomedical Engineering*, vol. 8, p. 125-137, DOI:10.1109/RBME.2015.2428305.
- [30] Smith, J.A., Jivraj, J., Wong, R., Yang, V. (2016). 30 years of neurosurgical robots: review and trends for manipulators and associated navigational systems. *Annals of Biomedical Engineering*, vol. 44, no. 4, 836-846, DOI:10.1007/s10439-015-1475-4.
- [31] Tan, A., Ashrafian, H., Scott, A.J., Mason, S.E., Harling, L., Athanasiou, T., Darzi, A. (2016). Robotic surgery: disruptive innovation or unfulfilled promise? A systematic review and meta-analysis of the first 30 years. *Surgical Endoscopy*, vol. 30, no. 10, p. 4330-4352, DOI:10.1007/s00464-016-4752-x.
- [32] Kantelhardt, S., Amr, N., Giese, A. (2014). Navigation and robot-aided surgery in the spine: historical review and state of the art. *Robotic Surgery: Research and Reviews*, vol. 2014, p. 19-26, DOI:10.2147/RSRR.S54390.
- [33] Vidaković, J., Jerbić, B., Šuligoj, F., Švaco, M., Šekoranja, B. (2016). Simulation for robotic stereotactic neurosurgery; 27th DAAAM International Symposium, on Intelligent Manufacturing and Automation, p. 562-568, DOI:10.2507/27th.daaam.proceedings.083.
- [34] Vajta, L. (2015). 3D Simulation in the advanced robotic design, test and control. *International Journal of Simulation Modelling*, vol. 4, no. 3, p. 105-117, DOI:10.2507/IJSIMM04(3)1.040.
- [35] Šekoranja, B., Jerbić, B., Šuligoj, F. (2015). Virtual surface for human-robot interaction. *Transactions of FAMENA*, vol. 39, no. 1, p. 53-64.
- [36] Šuligoj, F., Jerbic, B., Švaco, M., Sekoranja, B., Mihalinec, D., Vidakovic, J. (2015). Medical applicability of a low-cost industrial robot arm guided with an optical tracking system. *IEEE/RSJ International Conference on Intelligent Robots and Systems*, p 3785-3790, DOI:10.1109/IROS.2015.7353908.
- [37] Kobler, J.-P., Díaz Díaz, J., Fitzpatrick, J.M., Lexow, G.J., Majdani, O., Ortmaier, T. (2014). Localization accuracy of sphere fiducials in computed tomography images. *Proceedings SPIE 9036, Medical Imaging: Image-Guided Procedures, Robotic Interventions, and Modeling*, paper 90360Z, DOI:10.1117/12.2043472.

- [38] Micić, A.D., Đorđević, B.R., Lekić, P.N., Anđelković, B.R. (2013). Automatic determination of filter coefficients for local contrast enhancement. *Transactions of FAMENA*, vol. 37, no. 1, p. 63-76.
- [39] Varma, T.R.K., Eldridge, P. (2006). Use of the NeuroMate stereotactic robot in a frameless mode for functional neurosurgery. *The International Journal of Medical Robotics and Computer Assisted Surgery*, vol. 2, no. 2, p. 107-113, DOI:10.1002/rcs.88.
- [40] Brodie, J., Eljamel, S. (2011). Evaluation of a neurosurgical robotic system to make accurate burr holes. *The International Journal of Medical Robotics and Computer Assisted Surgery*, vol. 7, no. 1, p. 101-106, DOI:10.1002/rcs.376.
- [41] Švaco, M., Jerbić, B., Stiperski, I., Dlaka, D., Vidaković, J., Šekoranja, B., Šuligoj, F. (2016). T-phantom: A new phantom design for neurosurgical robotics. *27th DAAAM International Symposium on Intelligent Manufacturing and Automation*, p. 266-270, DOI:10.2507/27th.daaam.proceedings.039.
- [42] Willems, P.W., Noordmans, H.J., van der Sprenkel, J.W.B., Viergever, M.A., Tulleken, C.A. (2001). An MKM-mounted instrument holder for frameless point-stereotactic procedures: a phantom-based accuracy evaluation: Technical note. *Journal of Neurosurgery*, vol. 95, no. 6, p. 1067-1074, DOI:10.3171/jns.2001.95.6.1067.
- [43] Morgan, P.S., Carter, T., Davis, S., Sepehri, A., Punt, J., Byrne, P., Moody, A., Finlay, P. (2003). The application accuracy of the pathfinder neurosurgical robot. *International Congress Series*, vol. 1256, p. 561-567, DOI:10.1016/S0531-5131(03)00421-7.
- [44] Liu, J., Zhang, Y., Li, Z. (2006). The application accuracy of neuromaster: a robot system for stereotactic neurosurgery. *Proceedings of the 2nd IEEE/ASME International Conference on Mechatronic and Embedded Systems and Applications*, p. 1-5, DOI:10.1109/MESA.2006.296994.
- [45] Chan, F., Kassim, I., Lo, C., Ho, C.L., Low, D., Ang, B.T., Ng, I. (2009). Image-guided robotic neurosurgery—an in vitro and in vivo point accuracy evaluation experimental study. *Surgical Neurology*, vol. 71, no. 6, p. 640-647, DOI:10.1016/j.surneu.2008.06.008.
- [46] Schouten, M. G., Ansems, J., Renema, W.K.J., Bosboom, D., Scheenen, T.W.J., Fütterer, J. J. (2010). The accuracy and safety aspects of a novel robotic needle guide manipulator to perform transrectal prostate biopsies. *Medical Physics*, vol. 37, no. 9, p. 4744-4750, DOI:10.1118/1.3475945.
- [47] Kajita, Y., Nakatsubo, D., Kataoka, H., Nagai, T., Nakura, T., Wakabayashi, T. (2015). Installation of a Neuromate robot for stereotactic surgery: Efforts to conform to Japanese specifications and an approach for clinical use – Technical notes. *Neurologia Medico-Chirurgica*, vol. 55, no. 12, p. 907-914, DOI:10.2176/nmc.tn.2015-0043.
- [48] Ge, D.-Y., Yao, X.-F., Yao, Q.-H., Jin, H. (2014). Robot sensor calibration via neural network and particle swarm optimization enhanced with crossover and mutation. *Tehnički vjesnik - Technical Gazette*, vol. 21, no. 5, p. 1025-1033.
- [49] Švaco, M., Šekoranja, B., Šuligoj, F., Jerbić, B. (2014). Calibration of an industrial robot using a stereo vision system. *Procedia Engineering*, vol. 69, p. 459-463, DOI:10.1016/j.proeng.2014.03.012.
- [50] Finlay, P.A., Morgan, P. (2003). PathFinder image guided robot for neurosurgery. *Industrial Robot: An International Journal*, vol. 30, no. 1, p. 30-34, DOI:10.1108/01439910310457689.
- [51] Verburg, N., Baayen, J.C., Idema, S., Klitsie, M.A. J., Claus, S., de Jonge, C.S., Vandertop, W.P., de Witt Hamer, P.C. (2016). In vivo accuracy of a frameless stereotactic drilling technique for diagnostic biopsies and stereoelectroencephalography depth electrodes. *World Neurosurgery*, vol. 87, p. 392-398, DOI:10.1016/j.wneu.2015.11.041.
- [52] Šuligoj, F., Švaco, M., Jerbić, B., Šekoranja, B., Vidaković, J. (2017). Automated marker localization in the planning phase of robotic neurosurgery. *IEEE Access*, vol. 5, p. 12265-12274, DOI:10.1109/ACCESS.2017.2718621.
- [53] Švaco, M., Jerbić, B., Šuligoj, F. (2014). Autonomous robot learning model based on visual interpretation of spatial structures. *Transactions of FAMENA*, vol. 38, no. 4, p. 13-28.
- [54] Švaco, M., Jerbić, B., Šekoranja, B. (2017). Task planning based on the interpretation of spatial structures. *Tehnički vjesnik - Technical Gazette*, vol. 24, no. 2, p. 427-434, DOI:10.17559/TV-20160118150332.

A Novel Axial Modification and Simulation Analysis of Involute Spur Gear

Ningning Wang – Xueyi Li* – Kun Wang – Qingliang Zeng – Xiao Shen

Shandong University of Science and Technology College of Mechanical and Electronic Engineering, China

The transmission of spur gear mechanism may generate uneven load distribution because of machining error, assembly error, elastic deformation, and other factors, resulting in serious damage to the bearing capacity and service life of gears. To improve the contact condition of gear pairs and enhance the meshing performance and bearing capacity, this study proposed a novel axial modification method based on a composite modification curve with indefinite parameters and an evaluation method to evaluate modification effects. In addition to the surface equation of modified tooth was derived according to the composite modification curve, and the finite element model was built for gear pair. After conducting simulation analysis for the meshing process, the location and the shape of contact area as well as the other results can be acquired. In addition, the modification parameters can be optimized by performing orthogonal experiments for modified gear pairs; thus, the ideal modification effect is obtained at a specific operating condition. Moreover, comparison analysis was performed, and the results show that the phenomenon of uneven load distribution is dramatically improved when the gear pair was modified with optimized parameters, and the bearing capacity of the gear pair was increased. Finally, using the optimized parameters to trial-produce gears and conducting running-in tests, the effectiveness and the practicability of the method proposed in this study were verified.

Keywords: uneven load distribution, axial modification, simulated analysis, contact area, stress

Highlights

- A novel axial modification method based on composite modification curve is proposed for spur gears working in different conditions.
- Transient meshing analysis is conducted for modified gear pair.
- Modification parameters are optimized by conducting orthogonal experiment.
- Running-in tests are performed to verify the modification effects.

0 INTRODUCTION

As key components to bear load and transmit power, gear units are widely used in mechanisms, and the bearing capacity and service life significantly influence the performance of the equipment. However, the gear teeth and the shaft may generate deformation during the transmission, and there are machining errors and assembly errors. These factors may lead to the uneven load distribution along the tooth width direction, and may decrease the bearing capacity and service life, even resulting in the gear failure or production accidents. Axial modification, which can correct the shape and position of contact area by changing the structure of gear, is the most effective solution to solve the above issues. While Korotkin and Gazzaev [1] researched the gear transmission system with axial deviation, and they found that using the traditional method to calculate bearing capacity overestimated it in the gear units. Moreover, the shape of tooth surface changes with axial modification, which is different from the standard involute tooth surface. Thus, it is much more difficult to estimate the bearing capacity of gear systems with modification, and the design process is more complex. Therefore, investigating the modification theory and calculating

the strength as well as evaluating the performance of modified gears must be performed.

Since the theory of modification was proposed, numerous researchers have conducted studies on the problem from different aspects to improve the meshing performance of gear transmission. For example, Barbieri et al. [2] and [3] and Bonori et al. [4] explored the effects of profile modification using tooth contact analysis (TCA); furthermore, they used a genetic algorithm to optimize the method. An original method to calculate the transmission efficiency was proposed by Baglioni et al. [5], and the influence of tip relief was also discussed. Liu and Parker [6], Chenet al. [7], Wu et al. [8], Subramanian and Srinivasan [9] and Farshad et al. [10] all investigated the profile modification to reduce the vibration in gear transmissions. Moreover, in order to decrease the Hertzian stresses [11] and reduce the damage of thermal deformation [12], some researchers applied tooth width modification for gear pairs. Although these modification methods can improve the transmission performance for gear units, the uneven load distribution was not concerned in these studies.

Nejad et al. [13] conducted axial modification for the sun wheel in a planetary gear transmission system, and the analysis results indicated the effects

of axial modification. Furthermore, loaded tooth contact analysis (LTCA) was performed by Li [14] and [15] to research the influence of machining error and axial modification on surface contact stress and root bending stresses. Some researchers like Hotait and Kahraman [16] discussed the effect of shaft deviation and modification on the load distribution and stresses, and it was found that large deviations may increase the root bending stress and contact stress. Based on the gear geometry, Hsu and Su [17] and Kawalec and Wiktor [18] derived the cutter equations to machine-modified gears. All of these studies illustrate the importance of axial modification to improve the gear meshing, however, modification parameters were not optimized. Thus, Alessio et al. [19] viewed decreasing the contact stress and the fluctuation of transmission error as objective, and the modified gear was optimized by performing a load distribution program (LDP). However, it was not verified by conducting experiments in practice. In the aspects of modelling and simulation analysis, some people conducted static analysis for gear pair instead of transient meshing analysis, and the transient meshing performance cannot be obtained at all. Moreover, researchers, including Tesfahunegn et al. [20], established the model in Pro/E, while analysed in other simulation software. It may lead to the data loss, and the analysis may be failed.

To overcome the defects in the previous studies, a new method to obtain an ideal modification for gear pair was proposed in this study based on the composite modification curve to eliminate the uneven load distribution. Taking a pair of gears as an example, the implementation process of this method was introduced in detail. Specifically, the model of modified gear pair was precisely established based on cubic B-spline interpolation, and the modification parameters were optimized based on orthogonal experiments. Finally, according to the optimized parameters, the gear pair was trail-produced, and the method proposed in this study was verified by a performing running-in test.

The rest of this paper is organized as follows. Section 1 mainly introduces the theory of axial modification. Section 2 shows the method to analyse the meshing performance of a modified gear pair, including parametric modelling and analysing the meshing characteristic. The method of optimizing modification parameters based on an orthogonal experiment is briefly introduced in Section 3. Taking a pair of gears as an example in Section 4, the final design results were obtained based on the method proposed, and a series of comparative tests are conducted in this section. Section 5 indicates the

process and results of running-in test. At last, the conclusions are summarized in Section 6.

1 AXIAL MODIFICATION METHOD OF INVOLUTE SPUR GEAR

There is deviation along the tooth width direction because of machining error, assembly error, and elastic deformation. This may lead to uneven load distribution and the gear teeth may be broken, which is very harmful to the transmission. Hence, axial modification should be applied to the spur gear pair, also known as lead crowning modification. Thus, the contact area moves to the centre of the tooth width and the above issues are solved. Ordinarily the modification is only conducted to the smaller gear in order to decrease the machining cost.

The shape of single tooth with axial modification looks like the solid part in Fig. 1a, while the gear tooth without modification looks like the dotted portion in the figure. A pair of gear teeth meshing with each other is as shown in Fig. 1b, where c_c is the maximum amount, b is the width of the gear, b_c represents the distance from the centre of modification to the tooth end, C_m is the modification curve, b_{ci} and c_{ci} respectively represents the distance between the centre of modification to any point P_i and the modification amount at that point, $F_{\beta\gamma}$ is the value of axial deviation, and γ_d is the angle of deviation. It can be found that the shape of modified gear tooth depends on the distance b_c , the modification amount c_c and the modification curve C_m .

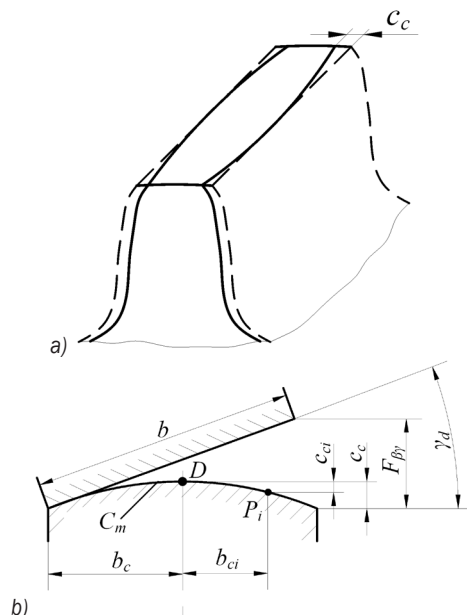


Fig. 1. Axial modification for gear; a) single gear tooth; and b) a pair of gear teeth

Most of current literature indicates that the modification centre coincides with the tooth width centre. However, it is not the best choice in practice. The position of the modification centre should be adjusted with working condition of gear transmission, which has been discussed in reference [21], and a reasonable equation to calculate the position of modification centre is presented as Eq. (1) according to the reference.

$$b_c = \sqrt{\frac{8F_m b}{C_\gamma F_{\beta\gamma}}} \quad (1)$$

In Eq. (1), F_m is peripheral force, and C_γ is meshing stiffness.

In addition, the maximum modification amount and the axial deviation can also be calculated, too. The detailed calculating methods are not presented here due to the limitations of space. The position of modification centre is shown in Fig. 2, b_c and R_c respectively represents the distance between the modification centre to the tooth end and the radius of modification when the modification centre coincides with the centre of tooth width, and b_c' as well as R_c' respectively represent the distance and the radius when the two centres do not coincide with each other.

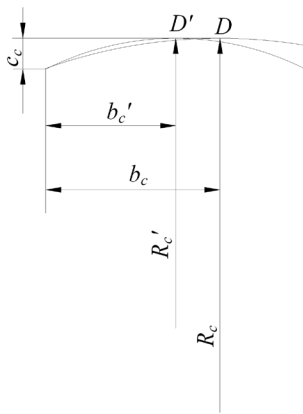


Fig. 2. Diagram of the modification centre

The modification curve has an important influence on the meshing performance of the gear. The circular curve is the most commonly used because it is easy to process; however the contact area of the gear pair may be a little small, and may decrease the bearing capacity. A composite power curve is proposed in this study, and the modification amount of any point P_i on the curve is as follows:

$$c_{ci} = \varepsilon c_c \cdot \left(\frac{b_{ci}}{b_c}\right)^\lambda + (1-\varepsilon)c_c \cdot \left(\frac{b_{ci}}{b_c}\right)^\phi \quad (2)$$

In Eq. (2), b_{ci} represents the distance from the point P_i to the modification centre, mm; ε is the superposition coefficient, $0 < \varepsilon < 1$; λ and ϕ are power of polynomial, $1 \leq \lambda \leq 3$, $1 \leq \phi \leq 3$. Any shape of modification curve can be obtained by adjusting ε , λ as well as ϕ . As for gear pairs working in different conditions, modification parameters should be different too, and the universal circular curve could not satisfy all the gear pairs. Thus, ideal modification ways can be obtained for different gear pairs based on the composite power curve.

2 MESHING PERFORMANCE ANALYSIS FOR MODIFIED GEAR PAIR

In order to assess the meshing performance and modification effects, the modified gear pair needs to be trail-produced abnormally, followed by observing the position of contact area, the shape of contact area, tooth deformation after conducting running-in tests. This kind of process is complex and wasteful. Therefore, finite element analysis is performed for modified gear pairs in this study, and the stresses as well as meshing performance can be read after simulation on computers.

2.1 Parametric Modelling for Modified Gear Pair

According to the bottom-up modelling ideas, the finite element model for modified gear pairs can be established using ANSYS parametric design language (APDL). Because the tooth surface with modification is a complex surface rather than straight surface along the axial direction, it is difficult to build the model precisely. In this study, the point matrix of the modified tooth surface can be established layer by layer along the modification curve, and then the method of cubic B-spline interpolation is used to build the tooth surface.

If the gear is conducted with axial modification, the coordinates of point P_i at any k -section are shown as Eq. (3):

$$\begin{cases} r_{ki} = \frac{r_b}{\cos \alpha_{ki}} \\ \theta_{ki} = \left(\tan \alpha_{ki} - \alpha_{ki} + \frac{c_{ci}}{r_a} \right) \cdot \frac{180}{\pi} \\ b_{ki} = b_{ci} \end{cases} \quad (3)$$

where r_b and r_a respectively represents the radius of the basic circle and addendum circle, and α_{ki} is the pressure angle of point P_i , which is as follows:

$$\alpha_{ki} = \frac{\alpha_a - (i-1) \cdot (\alpha_a - \alpha_f)}{n-1} \cdot \frac{\pi}{180}. \quad (4)$$

In the equation, n is the number of selected points on the profile curve, α_a and α_f respectively represent the pressure angle of tooth addendum and tooth root.

Calculating the coordinates of points on the tooth surface along the axial direction using the above equations, the point matrix can be established based on the coordinates. Then the modified tooth surface can be built by performing the method of cubic B-spline interpolation mentioned in literature [22]. Besides, the model of bigger gear without modification is built using universal method. According to the previous work [23] our research group done, the simplified meshing model of gear pair can also be built. Specially, in order to imitate the axial deviation between the gear pair, the driven gear should rotate based on the value of deviation, and the rotation angle is shown as Eq. (5):

$$\omega = \arctan\left(\frac{F_{\beta\gamma}}{B_2}\right) \cdot \frac{180}{\pi}, \quad (5)$$

where B_2 represents the tooth width of the driven gear.

Before the transient meshing analysis is performed for a modified gear pair, face-to-face contact should be conducted between the gear pair, and then build a rigid bond between the centre node and the inner surface for each gear in order to apply loads and constraint easily. Moreover, the rotate speed and torque should be applied respectively to the centre nodes. Thus, the finite element model of modified gear pair can be solved. The finite element model of modified gear pair looks like Fig. 3, and the detail process of modelling is shown in Fig. 4.

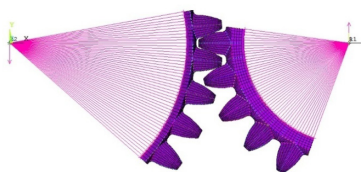


Fig. 3. Finite element model of modified gear pair

2.2 Meshing Performance Analysis of Modified Gear Pair

After conducting transient meshing analysis, many analysis results can be obtained. The variation of root bending stress and surface contact stress during the transmission can be drawn as a line chart (Fig. 5), and

the change law of stresses can be obtained from the chart. It can be found that the meshing state of the gear pair has experienced the transformation from single tooth meshing to double tooth meshing and then to single tooth meshing. Thus, the stresses are changed with the variation of meshing state.

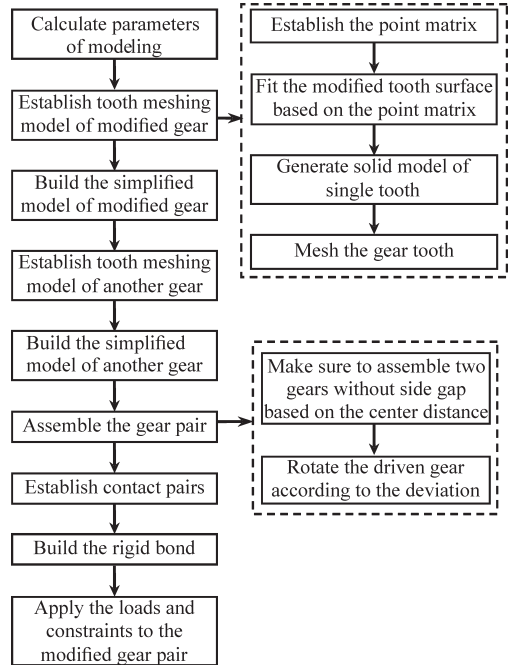


Fig. 4. Flow chart of modelling

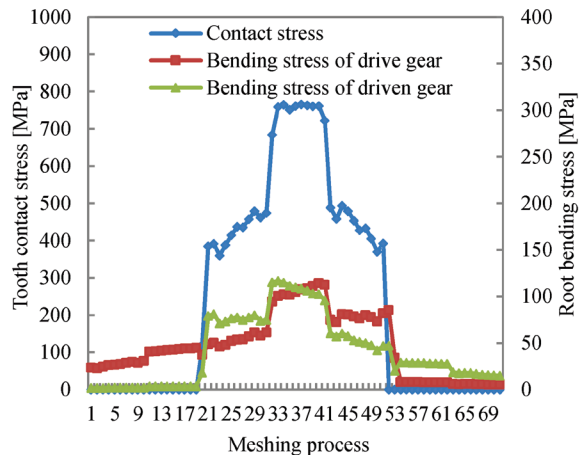


Fig. 5. Variation of stresses

Besides, the maximum of every stress and corresponding meshing position can be separately read from the line chart. Acquiring the meshing positions of maximum root-bending stresses of the drive gear and the driven gear, the static analyses are conducted respectively at these two positions. Thus, tooth deformation can be read after analysis, and the

bigger one is the maximum deformation during the transmission.

Moreover, the maximum of contact stress and corresponding worst meshing position can be found from the line chart. The distribution of contact stress can be obtained at the worst meshing position in detail. Moreover, the contour map of the contact stress can be read in this meshing position too. The shape and location of contact area can be observed from the contour map. Usually, the contour map of contact stress looks like Fig. 6. When comparing the location and the shape of contact area as well as the distribution of contact stress when the gear pair is without modification or with other modification method, the modification effects can be acquired.

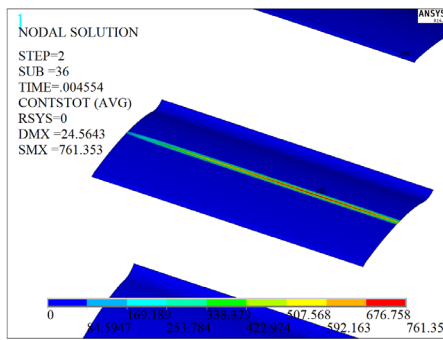


Fig. 6. Contour map of the contact stress

The above is a part of results can be read after conducting transient meshing analysis. These results reflect the meshing performance of modified gear pair; moreover, they also lay the foundation for the following orthogonal experiment as well as comparative analysis.

3 OPTIMIZATION OF MODIFICATION PARAMETERS BASED ON ORTHOGONAL EXPERIMENT

As mentioned above, modification parameters should be different for gear pairs working in different conditions. To obtain the ideal modification effect, modification parameters are optimized by conducting orthogonal experiment in this study based on the evaluation method for modified gear pair mentioned in the third section. As a kind of method to solve multi-level and multi-factor issues, the orthogonal method is easy to implement and can greatly decrease the number of tests. Thus, numerous researchers, such as Perce [24], arranged their experiments by using orthogonal tables. It can be found that there are three factors in this study, superposition coefficient ϵ , power λ as well as φ , and every factor can be divided into

many levels. If the division level is too much, the experiment efficiency will be reduced. Or if it is too small, the experiment effect couldn't be very well. These three factors are divided into five levels in this study, and the details are shown in Table 1.

Table 1. Factors and levels of orthogonal experiment

Levels	Factors		
	Coefficient ϵ	Power λ	Power φ
1	0.1	1	1
2	0.3	1.5	1.5
3	0.5	2	2
4	0.7	2.5	2.5
5	0.9	3	3

A suitable orthogonal table for this experiment can be chosen according to the number of factors and levels. Because there are three factors, and every factor is divided into five levels, orthogonal array $L_{25}(5^6)$ was used in this study, and the three columns at the back of the table were ignored. Twenty-five tests were conducted in total, and the details of each test are shown in Table 2.

Table 2. Scheme of orthogonal experiment

Test number	Factors		
	Coefficient ϵ	Power λ	Power φ
1	0.1	1	1
2	0.1	1.5	1.5
3	0.1	2	2
4	0.1	2.5	2.5
5	0.1	3	3
6	0.3	1	1.5
7	0.3	1.5	2
8	0.3	2	2.5
9	0.3	2.5	3
10	0.3	3	1
11	0.5	1	2
12	0.5	1.5	2.5
13	0.5	2	3
14	0.5	2.5	1
15	0.5	3	1.5
16	0.7	1	2.5
17	0.7	1.5	3
18	0.7	2	1
19	0.7	2.5	1.5
20	0.7	3	2
21	0.9	1	3
22	0.9	1.5	1
23	0.9	2	1.5
24	0.9	2.5	2
25	0.9	3	2.5

Transient meshing analyses were performed for a gear pair, which is modified using parameters according to Table 2. By observing the position and the shape of contact area as well as by comparing the stresses and tooth deformation in every test, modification parameters can be optimized and the ideal modification way for the gear pair is obtained.

4 SIMULATION AND COMPARATIVE ANALYSIS

Numerous spur gear pairs were performed to find suitable modification ways based on the method proposed in this study, and all results verified the validity of the method. A pair of gears used in an automobile transmission system is introduced as an example, and axial modification design is conducted on the gear pair. Furthermore, the meshing performance and modification effect are evaluated. The specific parameters of the gear pair are shown in Table 3.

Table 3. Parameters of the gear pair

Number of teeth	Drive gear	23
	Driven gear	34
Modification coefficient	Drive gear x_1	0.2322
	Driven gear x_2	0.0259
Tooth width [mm]	Drive gear B_1	20
	Driven gear B_2	20
Module m		4
Pressure angle α [°]		20
The rotate speed of drive gear [r/min]		1080
The torque of drive gear [Nm]		110
Load factor		1.557
Axial deviation [μm]		18.72

For this pair of gears, the allowable maximum contact stress is $[\sigma_H]=945$ MPa, the allowable root bending stress of the drive gear is $[\sigma_F]_1=376.43$ MPa, and the allowable root bending stress of driven gear is $[\sigma_F]_2=377.14$ MPa. Using the traditional method to calculate stresses of the gear pair, the contact stress is 844.05 MPa, the root bending stress of the drive gear is 136.24 MPa, and the root bending stress of the driven gear is 137.59 MPa. All stresses are less than the allowable stress respectively, which can meet strength requirement. However, the traditional design method mainly depends on the experience of researchers, and the design results need to be revised based on some correction factors. Sometimes, it could not precisely estimate the working condition, tooth deformation and so on. Thus, the design results might be unreasonable and could not be applied in practice.

Therefore, the transient meshing analysis was conducted on the gear pair without modification shown in Table 3, and axial deviation was considered in the modelling process to simulate the actual situation. Analysis results were read after simulation. It can be found that the contact stress of the gear pair is 1275.3 MPa, the root bending stress of the drive gear is 157.27 MPa, and the root bending stress of the driven gear is 163.17 MPa. Furthermore, the contour map of contact stress on the tooth surface is shown in Fig. 7. The figure indicates that there is severe uneven load distribution, and the contact stress exceeds the allowable value, which means the gear pair cannot meet the strength requirement. Hence, it is very important to conduct axial modification for the gear pair.

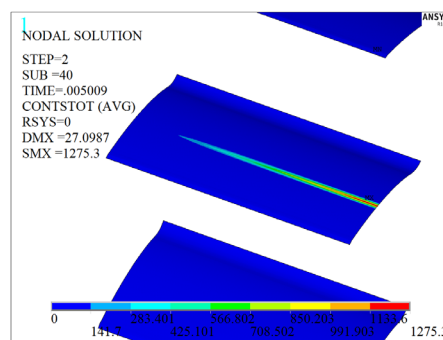


Fig. 7. Contour map of the contact stress

In order to obtain ideal modification parameters, an optimization experiment was conducted on the gear pair based on the orthogonal method, as mentioned above. The experiment's results are shown in Table 4.

Comparing the position and shape of contact area, stresses of modified gear pair as well as tooth deformation after completing all the orthogonal experiment, the modification parameters can be optimized, and the most suitable modification method is obtained. It can be found that there are six tests, test 3, 7, 12, 17, 19, and 23, the distances from the centre of contact area to the centre of tooth width are short in these tests, and the shape of contact area is narrow and long. Furthermore, the stress values indicate that the gear pair satisfies strength requirement in these tests, thus the parameters used in the test with the smallest tooth deformation are optimized parameters for the gear pair. Particularly, tooth deformation in Test 7 is the smallest. Therefore, the parameters in Test 7 are optimized, and the formula of the modification curve is as shown in Eq. (6):

$$c_{ci} = 0.3c_c \cdot \left(\frac{b_{ci}}{b_c}\right)^{1.5} + 0.7c_c \cdot \left(\frac{b_{ci}}{b_c}\right)^2. \quad (6)$$

Table 4. Experiment results

Test number	Factors			Experiment results				
	Coefficient ε	Power λ	Power φ	Contact stress [MPa]	Root bending stress of drive gear [MPa]	Root bending stress of driven gear [MPa]	Tooth deformation $\times 10^{-3}$ [mm]	Distance between contact pot to centre of tooth width [mm]
1	ε_1	λ_1	φ_1	826.74	118.33	120.81	14.806	9
2	ε_1	λ_2	φ_2	749.48	114.83	117.20	13.392	7
3	ε_1	λ_3	φ_3	779.20	114.11	116.0	13.468	4
4	ε_1	λ_4	φ_4	829.02	114.93	117.83	13.941	3
5	ε_1	λ_5	φ_5	875.54	116.23	119.29	14.412	4
6	ε_2	λ_1	φ_2	771.18	115.87	118.28	13.811	8
7	ε_2	λ_2	φ_3	761.27	114.33	116.88	13.371	4
8	ε_2	λ_3	φ_4	813.63	114.68	117.53	13.798	3
9	ε_2	λ_4	φ_5	861.32	115.84	118.85	14.271	4
10	ε_2	λ_5	φ_1	786.84	117.54	120.10	13.832	7
11	ε_3	λ_1	φ_3	766.64	116.20	118.67	13.602	7
12	ε_3	λ_2	φ_4	781.80	117.40	114.74	13.442	4
13	ε_3	λ_3	φ_5	827.39	115.16	118.07	13.937	4
14	ε_3	λ_4	φ_1	778.70	116.46	119.01	13.613	6
15	ε_3	λ_5	φ_2	805.52	115.30	118.14	13.747	4
16	ε_4	λ_1	φ_4	784.26	117.20	119.72	13.911	8
17	ε_4	λ_2	φ_5	776.45	115.82	118.37	13.512	5
18	ε_4	λ_3	φ_1	763.31	115.36	117.82	13.431	6
19	ε_4	λ_4	φ_2	800.33	114.75	117.58	13.675	4
20	ε_4	λ_5	φ_3	846.65	115.58	118.56	14.127	4
21	ε_5	λ_1	φ_5	810.52	118.07	120.57	14.461	8
22	ε_5	λ_2	φ_1	756.03	115.18	117.56	13.527	8
23	ε_5	λ_3	φ_2	774.83	114.18	116.85	13.433	4
24	ε_5	λ_4	φ_3	823.89	114.85	117.73	13.894	3
25	ε_5	λ_5	φ_4	870.81	116.10	119.15	14.365	4

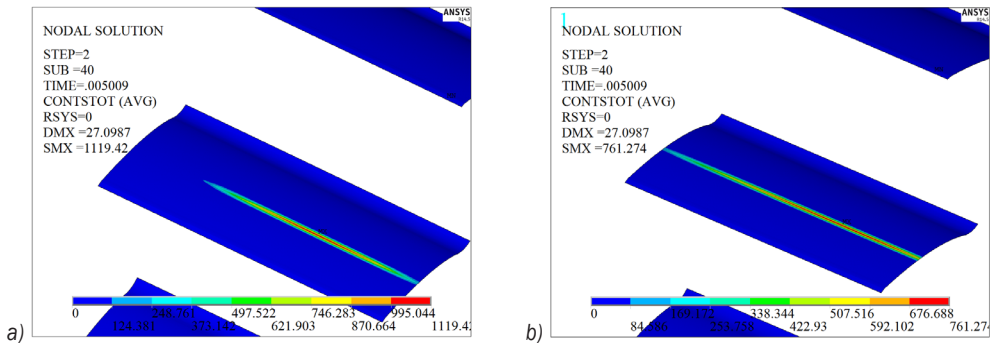


Fig. 8. Contour map of contact stress; a) universal modification method; and b) the optimized method

Moreover, transient meshing analysis was conducted for the gear pair with arc modification curve in order to expose the effects of different modification methods. The details of comparison are as follows.

If the gear pair is modified using universal modification method, the contour map of contact

area is shown as Fig. 8a. Comparing Fig. 8a with Fig. 7, the phenomenon of uneven load distribution is improved when the gear pair is modified, and the contact area closes to the centre of gear. However, the contact area is not long enough, and the contact stress is still higher than the allowable value. The universal modification method is not suitable for the gear pair

shown in Table 3. When the gear pair is modified using the method proposed in this study, the contour map of contact stress is shown as Fig. 8b. It can be found from the figure that uneven load distribution is dramatically improved, and the contact stress is lower than the allowable value. The gear pair satisfies the strength requirement.

In addition, the line chart of contact stress value along the tooth width is made, as in Fig. 9, in order to observe the effect of different modification methods on the distribution of contact stress more intuitively. The chart indicates that the distribution is more uniform when the gear pair is modified with the optimized parameters.

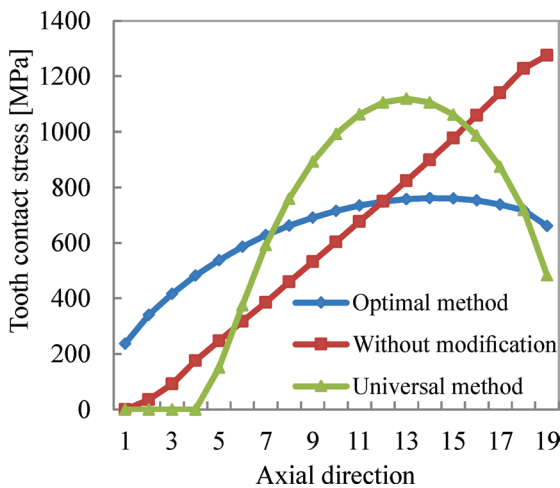


Fig. 9. Value of contact stress along the axial direction

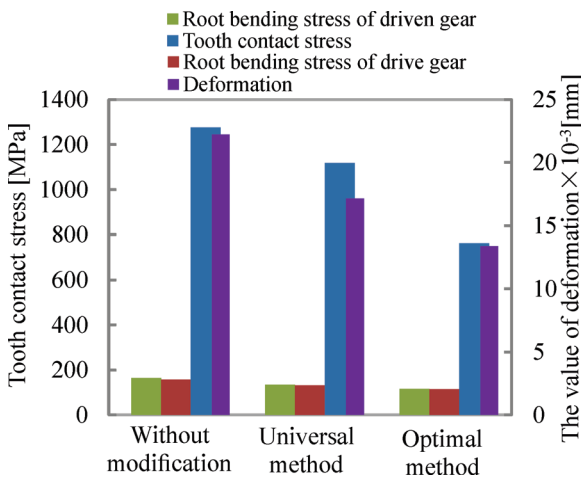


Fig. 10. Comparison of different methods

Moreover, the contact stress, the root bending stress of drive gear, the root bending stress of driven gear, and the tooth deformation are described as Fig. 10 when the gear pair is in the above three situations.

It is easily found that the stresses and the tooth deformation are dramatically decreased when the gear pair is modified with the method proposed in this study.

5 EXPERIMENT

For the purpose of verifying the validation of method proposed in this study, not only has the transient meshing analysis been performed, but it also has trail-produced the gear pair as shown in Table 3 and conducted running-in test. When the test finished, the actual conduct area of the gear pair without modification was shown as Fig. 11. It can be easily determined that there is severe uneven load distribution. In view of this situation, it is necessary to conduct axial modification for the gear pair.

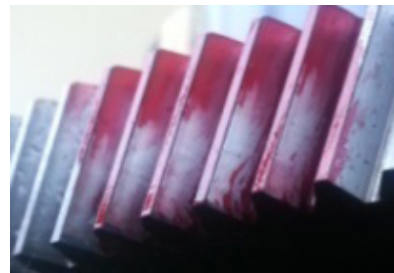


Fig. 11. Actual contact area of the gear without modification

Based on the method proposed in this study, the gear pair was modified with optimized modification parameters. A running-in test for the trail-produced modified gear pair and the actual contact area is shown as Fig. 12. The contact area locates approximately at the centre of the tooth width. And the phenomenon of uneven load distribution is obviously improved compared to the results in Fig. 11.



Fig. 12. Actual contact area of modified gear

6 CONCLUSIONS

An axial modification method is proposed based on the composite modification curve in this study, and the details of the process were introduced in

this study. The comparison analysis verified the advantages of this method. In addition, the running-in tests were conducted after trail-producing gear pairs, and the results indicate the operability of the method. Moreover, the following conclusions can be drawn:

1. Conducting axial modification to the spur gear pairs with involute profile can improve the phenomenon of uneven load distribution and decrease the stresses of gears, thus the bearing capacity of a gear pair can be increased.
2. The modification effect is obtained by reading contact stress, root-bending stress of gears as well as tooth deformation and observing the situation of the contact area; modification parameters strongly influence the modification effect.
3. The modification method proposed in this study has stronger adaptability than the universal method.

In summary, it is meaningful to present a novel modification method and the assessment method to evaluate the modification effect to find suitable modification parameters for different gear pairs. However, the method proposed is only used in the transmission of spur gears at present. It will be applied to the bevel gears and the fatigue analysis will be considered in future study.

7 ACKNOWLEDGEMENTS

This work was supported by the National Natural Science Foundation of China (Grant No. 51674155), the Science and Technology Development Program of Shandong Province (Grant No. 2017GGX30127), the Special Funds for Cultivation of Taishan Scholars, the Shandong Provincial Natural Science Foundation of China (Grant No. ZR2016EEQ24), and the Innovation Foundation for Graduate Students of Shandong University of Science and Technology (Grant No. SDKDYC170330).

8 REFERENCES

[1] Korotkin, V.I., Gazzaev, D.A. (2011). Axial error of gears and the tooth stress state in involute gear systems. *Russian Engineering Research*, vol. 31, no. 9, p. 834-837, DOI:10.3103/S1068798X11090140.

[2] Barbieri, M., Zippo, A., Pellicano, F. (2014). Adaptive grid-size finite element modeling of helical gear pairs. *Mechanism and Machine Theory*, vol. 82, p. 17-32, DOI:10.1016/j.mechmachtheory.2014.07.009.

[3] Barbieri, M., Bonori, G., Pellicano, F. (2012). Corrigendum to: Optimum profile modifications of spur gears by means of genetic algorithms. *Journal of Sound and Vibration*, vol. 331, no. 21, p. 4825-4829, DOI:10.1016/j.jsv.2012.05.028.

[4] Bonori, G., Barbieri, M., Pellicano, F. (2008). Optimum profile modifications of spur gears by means of genetic algorithms. *Journal of Sound and Vibration*, vol. 313, no. 3-5, p. 603-616, DOI:10.1016/j.jsv.2007.12.013.

[5] Baglioni, S., Cianetti, F., Landi, L. (2012). Influence of the addendum modification on spur gear efficiency. *Mechanism and Machine Theory*, vol. 49, p. 216-233, DOI:10.1016/j.mechmachtheory.2011.10.007.

[6] Liu, G., Parker, R.G. (2008). Dynamic modeling and analysis of tooth profile modification for multimesh gear vibration. *Journal of Mechanical Design*, vol. 130, no. 12, p. 121402-121414, DOI:10.1115/1.2976803.

[7] Chen, S.Y., Tang, J.Y., Chen, W.T., Hu, Z.H., Cao, M.P. (2014). Nonlinear dynamic characteristic of a face gear drive with effect of modification. *Meccanica*, vol. 49, no. 5, p. 1023-1037, DOI:10.1007/s11012-013-9814-8.

[8] Wu, Y.J., Wang, J.J., Han, Q.K. (2012). Static/dynamic contact FEA and experimental study for tooth profile modification of helical gears. *Journal of Mechanical Science and Technology*, vol. 26, no. 5, p. 1409-1417, DOI:10.1007/s12206-011-1028-1.

[9] Subramanian, R.B., Srinivasan, K. (2014). Vibration analysis of an influence of groove in the bottom land of a spur gear. *Journal of Vibration and Control*, vol. 20, no. 6, p. 847-858, DOI:10.1177/1077546312471363.

[10] Ahakeri Aski, F., Mirparizi, M., Sheykh Samani, F., Hajabasi, M.A. (2014). Vibration behavior optimization of planetary gear sets. *Propulsion and Power Research*, vol. 3, no. 4, p. 196-206, DOI:10.1016/j.jprr.2014.11.002.

[11] İmrek, H. (2009). Width modification for gears with low contact ratio. *Meccanica*, vol. 44, no. 5, p. 613-621, DOI:10.1007/s11012-009-9220-4.

[12] Düzcükoglu, H. (2009). PA 66 spur gear durability improvement with tooth width modification. *Materials & Design*, vol. 30, no. 4, p. 1060-1067, DOI:10.1016/j.matdes.2008.06.037.

[13] Nejad, A.R., Xing, Y.H., Guo, Y., Keller, J., Gao, Z., Moan, T. (2015). Effects of floating sun gear in a wind turbine's planetary gearbox with geometrical imperfections. *Wind Energy*, vol. 18, no. 12, p. 2105-2120, DOI:10.1002/we.1808.

[14] Li, S.T. (2007). Effects of machining errors, assembly errors and tooth modifications on loading capacity, load-sharing ratio and transmission error of a pair of spur gears. *Mechanism and Machine Theory*, vol. 42, no. 6, p. 698-726, DOI:10.1016/j.mechmachtheory.2006.06.002.

[15] Li, S.T. (2015). Effects of misalignment error, tooth modifications and transmitted torque on tooth engagements of a pair of spur gears. *Mechanism and Machine Theory*, vol. 83, p. 125-136, DOI:10.1016/j.mechmachtheory.2014.09.011.

[16] Hotait, M., Kahraman, A. (2008). Experiments on root stresses of helical gears with lead crown and misalignments. *Journal of Mechanical Design*, vol. 130, no. 7, p. 074502-074506, DOI:10.1115/1.2931127.

[17] Hsu, R.H., Su, H.H. (2014). Tooth contact analysis for helical gear pairs generated by a modified hob with variable tooth thickness. *Mechanism and Machine Theory*, vol. 71, p. 40-51, DOI:10.1016/j.mechmachtheory.2013.09.001.

[18] Kawalec, A., Wiktor, J. (2008). Simulation of generation and tooth contact analysis of helical gears with crowned flanks.

Proceedings of the Institution of Mechanical Engineers. Part B: Engineering Manufacture, vol. 222, no. 9, p. 1147-1160, DOI:10.1243/09544054JEM1104.

- [19] Artoni, A., Guiggiani, M., Kahraman, A., Harianto, J. (2013). Robust optimization of cylindrical gear tooth surface modifications within ranges of torque and misalignments. *Journal of Mechanical Design*, vol. 135, no. 12, p. 121005, DOI:10.1115/1.4025196.
- [20] Tesfahunegn, Y.A., Rosa, F., Gorla, C. (2010). The effects of the shape of tooth profile modifications on the transmission error, bending, and contact stress of spur gears. *Proceedings of the Institution of Mechanical Engineers, Part C: Journal of Mechanical Engineering Science*, vol. 224, no. 8, p. 1749-1758, DOI:10.1243/09544062JMES1844.
- [21] Song, L.M. (1987). *Tooth Profile and Gear Strength*. National Defense Press, Beijing.
- [22] Piegl, L., Tiller, W. (2012). *The NURBS Book*. Springer Science & Business Media, Berlin.
- [23] Zeng, Q.L., Wang, K., Wan, L.R., Zhang, X. (2017). Accurate modeling and transient meshing analysis of involute spur gear based on the principle of gear shaping. *International Journal of Simulation Modelling*, vol. 16, no. 2, p. 322-333, DOI: 10.2507/IJSIMM16(2)C07.
- [24] Perec, A. (2016). Abrasive suspension water jet cutting optimization using orthogonal array design. *Procedia Engineering*, vol. 149, p. 366-373, DOI:10.1016/j.proeng.2016.06.680.

An Analysis of Continuous Sandwich Panels with Profiled Faces

Metod Čuk¹ – Franc Kosel¹ – Nenad Zrnić² – Boris Jerman^{1,*}

¹ University of Ljubljana, Faculty of Mechanical Engineering, Slovenia

² University of Belgrade, Faculty of Mechanical Engineering, Serbia

Structural sandwich panels made of two thin steel facings that are bonded to a thick mineral wool core are often used as roofing material. This paper explores an application of numerical simulations in the investigation of structural behaviour of long span, continuous roof sandwich panels with profiled faces. Because of the required higher load-bearing capacity and strict deflection limitations, roof sandwich panels usually have one of the cover faces strongly profiled. A finite element analysis and an experimental study of a long span sandwich panel (with an inner strongly profiled and a flat outer face) in two-span configuration with transverse loading were conducted with a special attention given to the failure modes and bearing capacity prediction. The results obtained from the experiment confirmed the finite element analysis results.

Keywords: testing, finite element method, structural analysis, sandwich structures, strongly profiled faces, mineral wool, failure mode

Highlights

- A structural analysis of a long span continuous sandwich panel consisting of a thick mineral wool core and two thin steel sheet faces (with one strongly profiled and one flat face) is presented.
- An experimental bending test rig and a finite element method are used in the analysis of the ultimate limit state of the sandwich panel in two span configuration with transverse loading.
- The first failure mode of the sandwich panel is wrinkling failure at intermediate support.
- The results of numerical analysis correspond to the physical behaviour of the tested structure.

0 INTRODUCTION

Structural sandwich panels are composites consisting of two relatively thin facings enclosing a relatively thick core. The properties required for the faces are high stiffness (giving high flexural rigidity), high tensile and compressive strength, impact and wear resistance, environmental resistance (UV, heat, etc.), and surface finish. The properties of primary interest for the core are low density, shear modulus, shear strength, stiffness perpendicular to the faces, and (thermal and sound) insulation [1] and [2].

Sandwich panels used for claddings in the construction of industrial, commercial, and residential buildings that are usually mineral wool or polyurethane foam cored with steel sheet faces must as structural elements not only provide a function of the building enclosure, but also an important load-bearing function. While the wall sandwich panels mainly support variable loads such as the wind pressure, the sandwich panels used for roof claddings must also support some permanent loads: mainly their own weight and also the weight of possible solar panels or photovoltaic cells etc., and some variable loads like snow and wind loads, thermal loads, etc. These higher load-bearing requirements and strict deflection limitations are the reason why roof sandwich panels usually have one of the cover faces strongly profiled.

For the structural behaviour of sandwich panels, it is necessary to consider all of the potential failure

modes: tensile failure of the faces (due to tensile stress), local buckling (wrinkling) of the faces (due to compressive stress), and shear failure of the core or the adhesion between the core and face. In sandwich panels with thin strongly profiled faces, two additional failure modes are introduced: shear strength of the webs in a profiled face and the support reaction capacity of a profiled face [1]. The first failure mode of long and medium span length continuous multi-span panels is usually the buckling failure at intermediate support due to the interaction between the bending moment and support reaction [3] and [4].

The European standard EN 14509 [5], or European Recommendations published by the European Convention for Constructional Steelwork (ECCS) and the International Building Council (CIB) do not provide detailed design methods for sandwiches with strongly profiled faces. Determination of the load bearing capacity required for the design of sandwich panels is to a large degree based on test results [6].

Hassinen [7], and later Misiak and Hassinen [6] concluded that a calculation procedure based on the design principles developed for trapezoidal sheeting (Eurocode 3 [8] and [9]) was possible by taking into account the effect of the elastic foundation provided by the core layer. The basic principles of the design model backed by finite element calculations and test results were introduced for sandwich panels with an outer strongly profiled face and a flat inner face. A similar approach was also used by Pokharel and

Mahendran [10] and [11] for flat and lightly profiled sandwich panels. The investigation of structural behaviour and failure analysis of composite structures through the use of finite element analyses were also shown in [12] and [13].

The objective of this paper is to present a study of the structural behaviour of a continuous roof sandwich panel with flat outer and strongly profiled inner steel faces and a mineral wool core (as shown in Fig. 1) with transverse loading in a two span configuration (studied testing setup is shown in Fig. 3). The studied example was specified by the provider of building envelope solutions (including manufacturing of sandwich panels).

As previously mentioned, the first failure mode of such a long span panel is the buckling failure at intermediate support due to the interaction between the bending moment and positive support reaction. An analytical approach using “Engineer’s Theory of Bending” in this case is quite futile. For statically indeterminate panels (panels continuous over two or more spans), to determine the deflections and stresses in panels with profiled faces (when one or both faces of the panel are profiled), a more general analysis is required which takes into account the bending stiffness of the faces [1], as well as the support pressure distribution between the support and the sandwich panel [3] and [4]. In reality, it is relatively difficult to evaluate this interaction. The chances of being able to assess such a multiplicity of factors with sufficient accuracy by theoretical analysis would appear to be very small. The need for tests to analyse the failure criteria is indisputable [1].

To overcome the need for tests, an analysis of the ultimate limit state of the presented sandwich panel was conducted by numerical simulation. The results of the simulation and a comparison to the experimental results are presented.

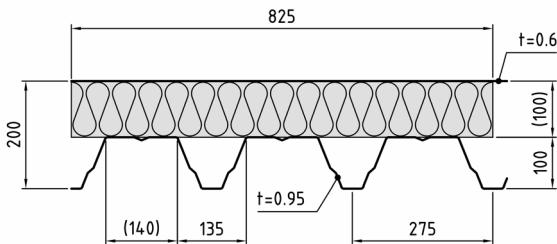


Fig. 1. Transverse (cross sectional) view of roof sandwich panel with a mineral wool core and a strongly profiled inner and a flat outer steel face

1 FINITE ELEMENT ANALYSIS

The structural behaviour of sandwich panels in a two span configuration with the inner of the two steel faces strongly profiled was investigated using the ANSYS® simulation software package.

Based on a series of preliminary finite element analyses simulating the experimental setup (see Chapter 2 and Fig. 3), a one-twelfth symmetry finite element model was built, as shown in Fig. 2.

A three-dimensional finite element model of the analysed sandwich panel consists of two different types of finite elements: solid (brick) elements (SOLID185) with large deflection and large strain capabilities were used for the core, and shell elements (SHELL181) that are well suited for large strain nonlinear applications were used to model the outer flat and the inner strongly profiled face. The element formulation is based on logarithmic strain and true stress measures [14]. The combination of brick and shell elements can be used if adequate compatibility conditions are implemented at element interfaces [12] and [15] to [17]. Adhesive layers between the mineral wool core and both steel faces were modelled by using couplings so that the displacement degrees of freedom in all three directions (UX, UY, and UZ) of coincident interface nodes of the elements of the faces and the core were coupled which is common approach in the modelling of bonded layers of different materials (non-metallic or metallic) [18] and [19].

An orthotropic elastic material model was employed to solid elements of the mineral wool core, and a bilinear isotropic hardening material model was applied to steel face shell elements. Mechanical properties and densities of steel faces and mineral wool core based on data provided by the sandwich panel manufacturer are shown in Tables 1 and 2, respectively.

Table 1. Material properties of steel faces

Density [kg/m ³]	Elastic modulus [GPa]	Yield strength [MPa]	Poisson ratio [-]	Tangent modulus [MPa]
7850	210	355	0.3	100

Table 2. Material properties of mineral wool core

Density [kg/m ³]	Elastic modulus [MPa]			Poisson ratio [-]			Shear modulus [MPa]		
ρ	E_x	E_y	E_z	n_{xy}	n_{yz}	n_{xz}	G_{xy}	G_{yz}	G_{xz}
100	0.50	7.0	3.0	0	0	0	0.40	2.0	0.40

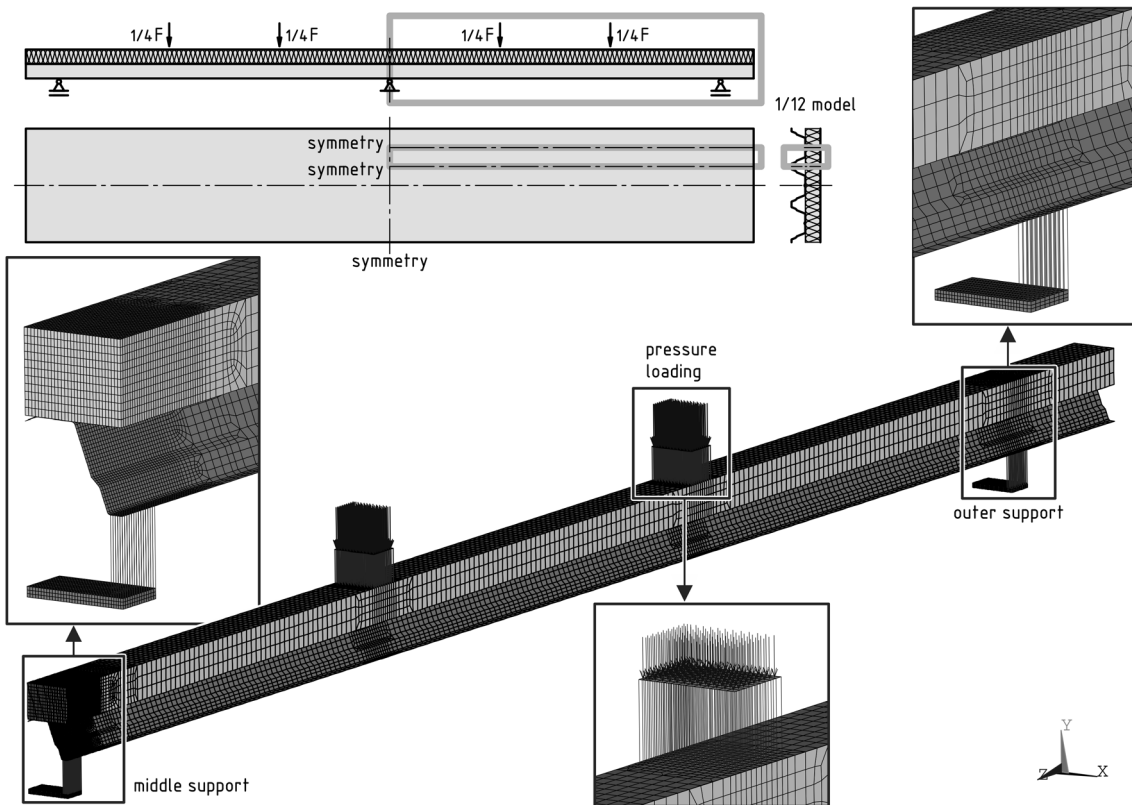


Fig. 2. The one-twelfth symmetry finite element model of sandwich panel in double span configuration with applied loads (symmetry and other boundary conditions not shown)

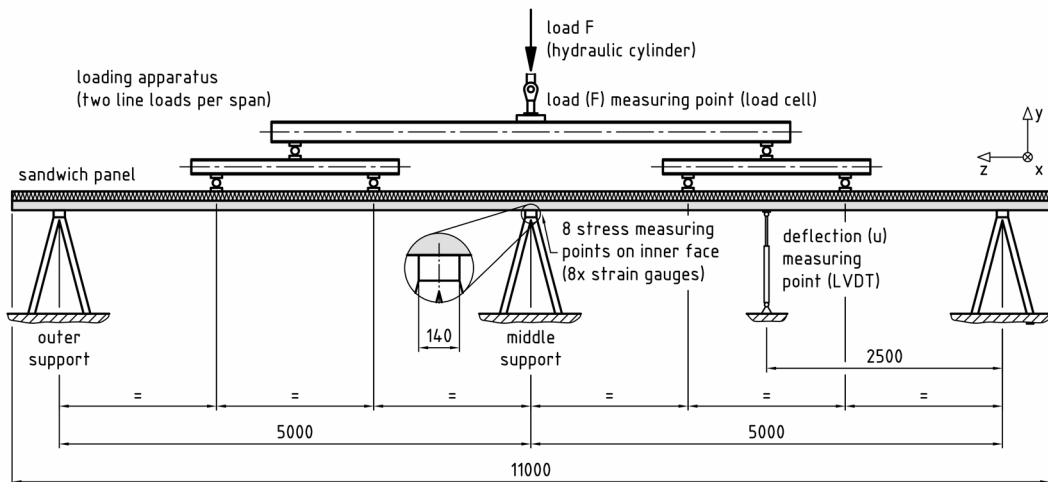


Fig. 3. Experimental setup: sandwich panel in double span configuration with load apparatus

It has to be noted that the coordinate directions used in Table 2 are consistent with the coordinates used in both the finite element and the experimental analyses (see Figs. 2 and 3): the X axis defines a direction parallel to the width of the panel, the Y axis defines a direction parallel to the panel thickness, and

the Z axis defines a direction parallel to the length of the sandwich panel.

In addition to the structural solid and shell elements, 3-D spar compression-only elements were used to emulate the simple supports of the bottom flange of the strongly profiled face of the sandwich

8x strain gauge measuring points:

- $P_{1,T} \dots P_{4,T}$ – top
- $P_{1,B} \dots P_{4,B}$ – bottom

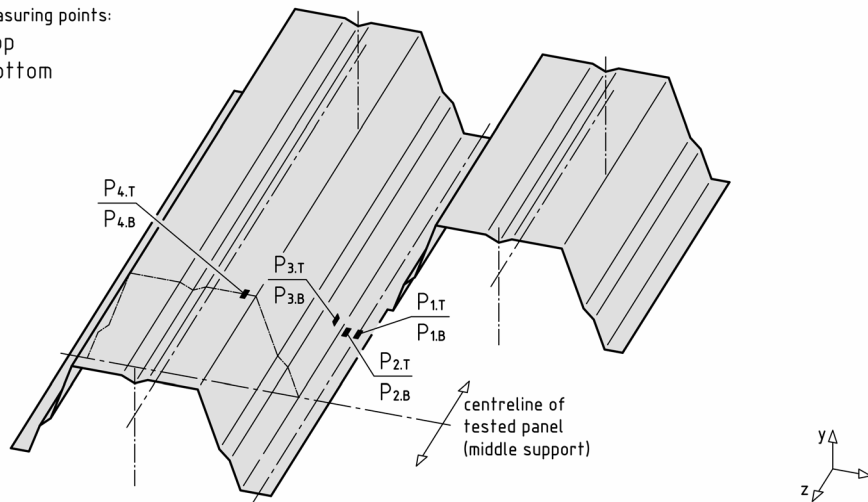


Fig. 4. Position of strain gauge measuring points on strongly profiled inner face of the tested sandwich panel above the middle support – two strain gauges are attached at each of four locations: one at the top surface ($P_{1,T} \dots P_{4,T}$) and one at the bottom surface ($P_{1,B} \dots P_{4,B}$)

panel. 3-D spar elements were also used to apply pressure loading at two loading areas on the flat face, and thus emulate a load apparatus from the experimental setup. A dead load of the load apparatus (a mass of 550 kg) was applied to the model by additional constant pressure load, while a dead load of the sandwich panel was applied by specified gravitational acceleration of 9.81 m/s^2 in the Y direction.

Due to the double symmetry of the tested sandwich panel across two perpendicular planes (parallel to XY and YZ planes) use of one-quarter symmetry model (with width of 412.5 mm, see Fig. 1) would be absolutely correct model. Based on the results from the preliminary analyses that had shown no significant difference in results between “one-quarter” model and the “one-twelfth” model (a sandwich panel model with infinite width i.e. dimension parallel to the X axis, see Fig. 2) the letter model was selected to shorten simulation times. Symmetric boundary conditions were applied at all three vertical “symmetry” planes (marked and labelled “symmetry” on Fig. 2, top left).

The model was solved numerically including large deformation effects.

2 EXPERIMENTAL INVESTIGATIONS

In order to verify the results of numerical analysis, an experimental investigation was conducted at the laboratory of the sandwich panel manufacturer. An experimental setup based on a modified bending

test rig used for a single span panel bending test (A.5 in [5]) with added middle support was used as shown in Fig. 3. An 11-m long single sandwich panel (transverse cross-sectional view is shown in Fig. 1) is placed horizontally on three equally spaced (by a distance of 5 m) simple supports in effectively a two span configuration since the overhangs on both sides were not additionally loaded (dead load only). Transverse loading of the tested panel was accomplished by a hydraulic cylinder. The load from the hydraulic cylinder was applied to the tested panel through a loading apparatus (two equidistant line loads per span).

The total applied transverse load F was measured using a load cell linked between the hydraulic cylinder and the loading apparatus while the midspan deflection u of the inner face was recorded using a linear variable differential transformer (LVDT) (see Fig. 3).

For the measurement of axial bending stresses σ_z at eight different measuring points ($P_{1,T} \dots P_{4,T}$ and $P_{1,B} \dots P_{4,B}$, see Fig. 4) strain gauges (in a quarter Wheatstone bridge configuration) were used. Two strain gauges were attached at each of the four different locations at both the top and the bottom surface of the inner (strongly profiled) steel face in the region above the middle support as shown.

The relevant positions of the stress measuring points on the profiled face of the tested sandwich panel were determined by preliminary finite element analyses. Pairs of measuring points $P_{1,T}$ and $P_{1,B}$, and $P_{2,T}$ and $P_{2,B}$ were located on the bottom, flange while the pair of points $P_{3,T}$ and $P_{3,B}$ was placed on

the web near the bottom flange, and the position of the measuring point pair $P_{4,T}$ and $P_{4,B}$ was selected on the top flange.

3 RESULTS

The results of both numerical and experimental analysis of the investigated long span length sandwich panel show an expected ultimate failure mode in the form of the wrinkling failure of a profiled face at the middle support due to the interaction between the bending moment and support reaction, as shown in Fig. 5.

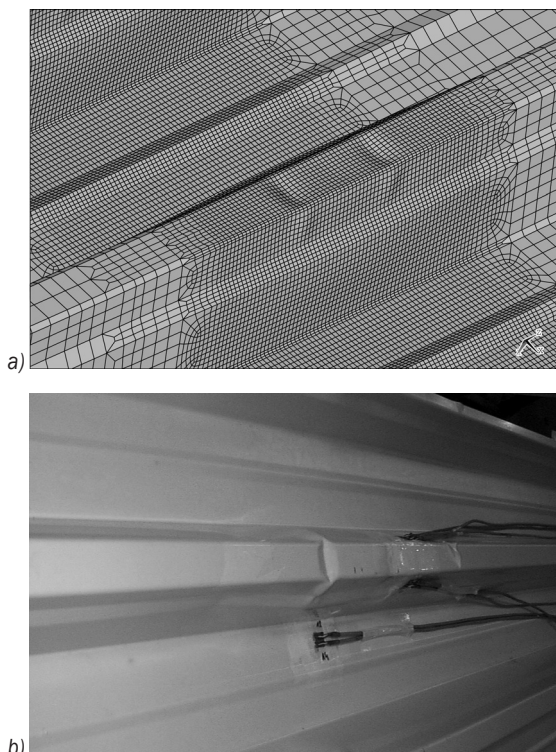


Fig. 5. Failure mode of analysed sandwich panel: support reaction capacity of a profiled face at medium support; (view from below) a) finite element calculation; b) tested specimen

In Fig. 6, calculated results of normal stress distribution σ_y in a mineral wool core above the middle support are shown. A compressed area of the core extends over 800 mm on each side of a centreline of the support in the longitudinal (Z) direction above the plane part of the top flange of the inner face. In the transverse (X) direction, the stress concentrations in the core above the bend of the top flange can be observed while gradually decreasing in the negative X direction toward a flange stiffener. All shown compressive stress values (up to 0.045 MPa) are

below the adequate proportional stress limit of the mineral wool (which is 0.1 MPa; from data provided by the sandwich panel manufacturer).

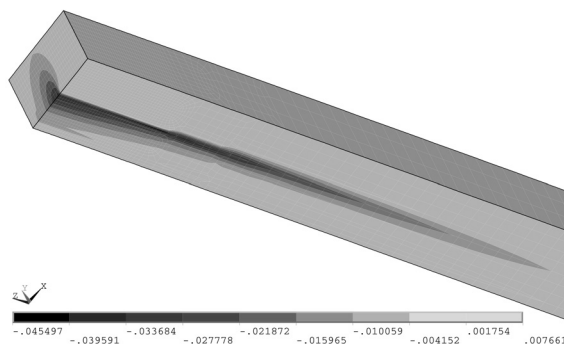


Fig. 6. Calculated normal stress σ_y [MPa] distribution in mineral wool core above middle support (bottom side, view from below) ($F = 30$ kN)

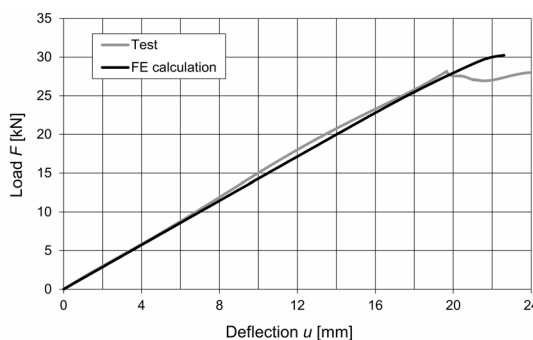


Fig. 7. Comparison of experimental and calculated relation load F vs. deflection u of the tested two-span roof sandwich panel

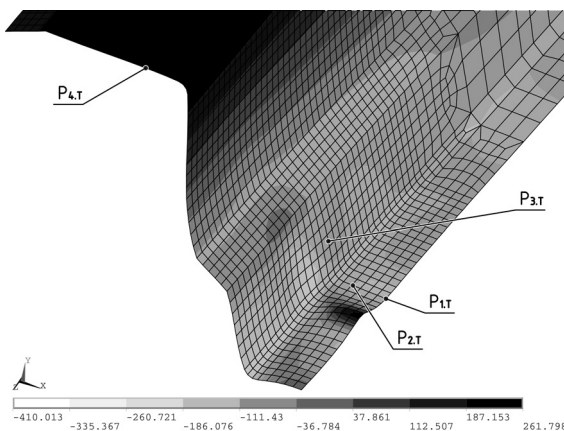


Fig. 8. Calculated axial bending stresses σ_z [MPa] at top surface of strongly profiled steel face above the middle support; measuring points $P_{1,T}$... $P_{4,T}$ are marked and labelled (top side, view from top) ($F = 30$ kN)

It is the characteristics of sandwich panels with strongly profiled faces at a support subject to a positive support reaction that the face distributes

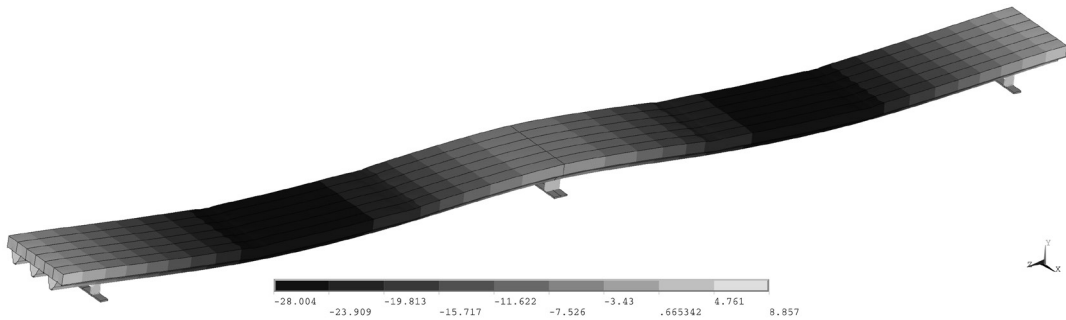


Fig. 9. Calculated deflections of the tested two-span roof sandwich panel (display created using symmetry expansion) ($F = 30$ kN)

(because of its high bending stiffness) the support reaction over the large area. Therefore, the checks of compression strength of the core on the support are no longer required [1]. In Fig. 7, a comparison of the applied load F vs. the deflection u obtained from calculated and experimental results (dead load deflections, of both sandwich panel and load apparatus are included and used as zero reference points) is shown. A good agreement is observed between the results in the pre-failure range (the maximum relative difference is 5 %). The value of the ultimate load obtained from experimental results is 28.1 kN and the value of the ultimate load based on calculated results is approximately 30 kN (a relative difference of 7 %).

Fig. 9 shows the calculated total deflection distribution (deflections due to the dead load of sandwich panel and load apparatus included) along the investigated sandwich panel in a double span configuration at calculated ultimate load ($F = 30$ kN).

Fig. 8 shows the calculated distribution of axial bending stresses σ_z [MPa] on the top surface (view from the top) of the inner steel face above the middle support (at a calculated ultimate load $F = 30$ kN). Wrinkles in the bottom flange and in the web (near bottom flange) of the profiled face due to the compression stresses can be noticed. The measuring points ($P_{1,T} \dots P_{4,T}$) where the axial bending stresses σ_z at the top surface were measured in the experiment are also marked and labelled.

In Fig. 10, the calculated and experimental axial bending stresses σ_z on the top surface (at measuring points $P_{1,T} \dots P_{4,T}$) and the bottom surface (at measuring points $P_{1,B} \dots P_{4,B}$) of the inner steel face above the middle support compared to applied load F are presented. The compressive axial stress values can be observed in points below the neutral axis of the face, i.e. points $P_{1,T} \dots P_{3,T}$ and $P_{1,B} \dots P_{3,B}$; and tensile stress values in points $P_{4,T}$ and $P_{4,B}$ that are above the neutral axis of the face as expected. A reasonably good agreement between the results can

be noticed in the pre-buckling load range. The relative differences at a load value of 20 kN (at $\frac{2}{3}$ value of ultimate load $F = 30$ kN) are between 28 % (at points $P_{2,B}$ and $P_{3,T}$) and 33 % (at point $P_{4,T}$). However, it has to be noted that a bad quality bonding of the strain gauge at the measuring point $P_{4,T}$ was observed in the post-test inspection. But, what is more important is the thorough agreement in a size relation between the stresses on the top and bottom surfaces of the steel face at each of the four measuring locations, i.e. a positive difference between the stresses at measuring points $P_{1,T}$ and $P_{1,B}$, and $P_{2,T}$ and $P_{2,B}$, respectively, and a negative difference between the stresses at measuring points $P_{3,T}$ and $P_{3,B}$, and $P_{4,T}$ and $P_{4,B}$, respectively. The established differences in the axial bending stresses are consistent with the deformed shape of the profiled steel face at corresponding points, as shown in Fig. 8 (and consequently also in Fig. 5).

5 CONCLUSIONS

Numerical simulations were used to study the structural behaviour of sandwich panels with a flat outer and strongly profiled inner face used in the roof claddings. Finite element analyses of a bending test of a continuous long span sandwich panel (in double span configuration and four transverse loads) were conducted. A “support reaction capacity of the profile” failure mode was established and the ultimate transverse load of the investigated configuration was determined. The results from the numerical simulations finite elements model were successfully validated using measured deflection and stress results from the experiment. Good agreement was found between the experimental and calculated relation of applied load F vs. deflection u (the maximum relative difference in pre-buckling load range is 5 %) and between the experimental and calculated ultimate load (relative difference of 7 %).

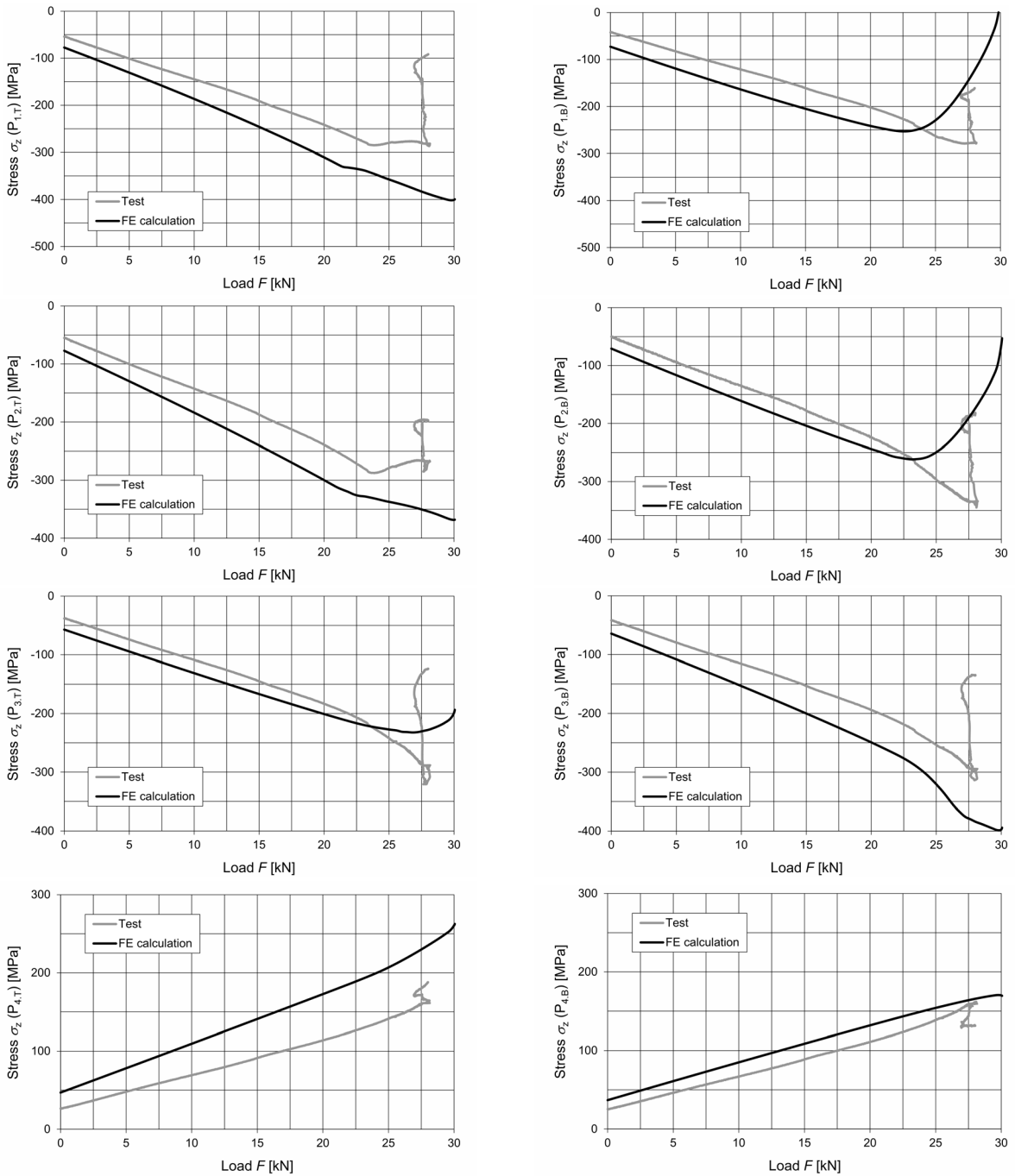


Fig. 10. Comparison of experimental and calculated axial bending stresses σ_z [MPa] in relation to applied load F [kN] at the top and the bottom surface of inner strongly profiled steel face at measurement points ($P_{1,T} \dots P_{4,T}$ and $P_{1,B} \dots P_{4,B}$) of the tested two-span roof sandwich panel

6 REFERENCES

[1] Davies, J.M. (2001). *Lightweight Sandwich Construction*. Blackwell Science, Oxford, DOI:10.1002/9780470690253.
 [2] Zenkert, D. (1997). *The Handbook of Sandwich Construction*. Chameleon Press, London.

[3] Hassinen, P., Martikainen, L. (1994). Analysis and Design of Continuous Sandwich Beams. *12th International Specialty Conference on Cold-Formed Steel Structures*, p. 523-538.
 [4] Hassinen, P., Martikainen, L. (1996). Design Models of Continuous Sandwich Panels. *13th International Specialty Conference on Cold-Formed Steel Structures*, p. 293-307.

- [5] EN 14509:2013. *Self-Supporting Double Skin Metal Faced Insulating Panels - Factory Made Products - Specifications*. European Committee for Standardization, Brussels.
- [6] Misiek, T., Hassinen, P. (2010). Unified Approach for the Local Buckling Of Sandwich Panels and Trapezoidal Sheeting. *Proceedings: W056 – Special Track 18th CIB World Building Congress*, Salford, p. 14-26.
- [7] Hassinen, P. (1997). Evaluation of the compression strength of profiled metal sheet faces of sandwich panels. *Thin-Walled Structures*, vol. 27, no. 1, p. 31-41, DOI:10.1016/0263-8231(96)00022-5.
- [8] EN 1993-1-3:2006. *Eurocode 3: Design of Steel Structures – Part 1-3: General Rules – Supplementary Rules for Cold Formed Members and Sheeting*. European Committee for Standardization, Brussels.
- [9] EN 1993-1-5:2006. *Eurocode 3: Design of Steel Structures – Part 1-5: Plated Structural Elements*. European Committee for Standardization, Brussels.
- [10] Pokharel, N., Mahendran M. (2004). Finite element analysis and design of sandwich panels subject to local buckling effects. *Thin-Walled Structures*, vol. 42, no. 4., p. 589-611, DOI:10.1016/j.tws.2003.08.002.
- [11] Pokharel, N., Mahendran M. (2005). An investigation of lightly profiled sandwich panels subject to local buckling and flexural wrinkling effects. *Journal of Constructional Steel Research*, vol. 61, no. 7, p. 984-1006, DOI:10.1016/j.jcsr.2004.12.008.
- [12] Rädcl, F., Lange, J. (2011). Tragfähigkeit von Sandwichelementen mit profilierten Deckschichten und Öffnungen. *Stahlbau*, vol. 80, no. 9, p. 656-661, DOI:10.1002/stab.201101469.
- [13] Ilić, I., Petrovic, Z., Maksimović, M., Stupar, S., Stamenković, D. (2012). Computation method in failure analysis of mechanically fastened joints at layered composites. *Strojniški vestnik – Journal of Mechanical Engineering*, vol. 58, no. 9, p. 553-559, DOI:10.5545/sv-jme.2011.157.
- [14] N/A (2012). *Elements Reference. Release 14.5 Documentation for ANSYS*. Ansys Inc., Canonsburg.
- [15] Kovačević, D., Budak, I., Antić, A., Kosec, B. (2011). Special finite elements: Theoretical background and application. *Tehnički vjesnik - Technical Gazette*, vol. 18, no. 4, p. 649-655.
- [16] Crococo, D., De Agostinis, M., Vincenzi, N. (2011). structural analysis of an articulated urban bus chassis via FEM: a methodology applied to a case study. *Strojniški Vestnik – Journal of Mechanical Engineering*, vol. 57, no. 11, p. 799-809, DOI:10.5545/sv-jme.2011.077.
- [17] Čuk, M., Štih, S., Jerman, B. (2013). Finite element analysis of sandwich panels with longitudinal joints and large openings. *Tehnički vjesnik - Technical Gazette*, vol. 20, no. 2, p. 275-284.
- [18] Djemana M., Hrairi M. (2016). Modelling and simulation of impedance-based damage monitoring of structures. *International Journal of Simulation Modelling*, vol. 15, no. 3, p. 295-408, DOI:10.2507/IJSIMM15(3)1.338.
- [19] Wang Y., Lu Y. J., Si C. D., Sung P. (2016). Tire-pavement coupling dynamic simulation under tire high-speed-rolling condition. *International Journal of Simulation Modelling*, vol. 15, no. 2, p. 236-248, DOI:10.2507/IJSIMM15(2)4.332.

Vsebina

Strojniški vestnik - Journal of Mechanical Engineering

letnik 63, (2017), številka 12
Ljubljana, december 2017
ISSN 0039-2480

Izhaja mesečno

Razširjeni povzetki (extended abstracts)

Tomaž Finkšt, Jurij Franc Tasič, Marjeta Zorman Terčelj, Marko Meža: Razvrščanje sumljivih področij na avtofluorescenčnih bronhoskopskih slikah v maligne/nemaligne	SI 103
Vytautas Ostaševičius, Vytautas Jūrėnas, Andrius Vilkauskas, Gytautas Balevičius, Andrius Senkus, Eglė Jotautienė: Nov pristop k vzbujanju pri ultrazvočno podprtem obodnem brušenju	SI 104
Damian Janicki: Izdelava plasti visokolegirane bele kromove jeklene litine na substratu nodularne litine z laserskim površinskim legiranjem	SI 105
Jiangping Mei, Jiawei Zang, Yabin Ding, Shenglong Xie, Xu Zhang: Hitro in samodejno umerjanje pogreška ničelne točke pri paralelnem robotu z dvema prostostnima stopnjama na podlagi novega merilnega mehanizma	SI 106
Marko Švaco, Bojan Šekoranja, Filip Šuligoj, Josip Vidaković, Bojan Jerbić, Darko Chudy: RONNA G3: nov robotski nevronavigacijski sistem	SI 107
Ningning Wang, Xueyi Li, Kun Wang, Qingliang Zeng, Xiao Shen: Nova aksialna modifikacija in simulacijska analiza čelnega evolventnega zobnika	SI 108
Metod Čuk, Franc Kosel, Nenad Zrnić, Boris Jerman: Analiza kontinuirnih sendvič plošč s profiliranim plaščem	SI 109

Razvrščanje sumljivih področij na avtofluorescenčnih bronhoskopskih slikah v maligne/nemaligne

Tomaž Finkšt¹ – Jurij Franc Tasič² – Marjeta Zorman Terčelj³ – Marko Meža^{2,*}

¹ Univerza v Ljubljani, Fakulteta za strojništvo, Slovenija

² Univerza v Ljubljani, Fakulteta za elektrotehniko, Slovenija

³ Univerzitetni klinični center Ljubljana, Klinični oddelek za pljučne bolezni in alergijo, Slovenija

Namen študije je bil razvoj postopka za razvrščanje sumljivih področij na bronhoskopskih slikah, ki predstavljajo maligna/nemaligna področja. Ustrezno izobražen specialist pulmologije s tehniko bronhoskopskega slikanja bronhialnih cevi identificira področja tkiva, na katerih opazi za maligno tkivo sumljiva področja. Bronhoskopsko preiskavo izvaja z uporabo slikanja in opazovanja slike z uporabo bele svetlobe, na kateri opazi spremembe v površini sluznice ter z uporabo ozko-valovne modre svetlobe ter opazovanja autofluorescenčnega odziva tkiva v področju rdečih in zelenih valovnih dolžin. Maligno tkivo namreč za razliko od nemalignega izseva več svetlobe v področju rdečih valovnih dolžin kot v področju zelenih valovnih dolžin.

V okviru raziskave smo analizirali delovanje razvitega algoritma v smislu natančnosti razvrščanja sumljivih vzorcev tkiva. Na voljo smo imeli s strani specialista bronhoskopije sumljiva področja določena kot maligno tkivo. Za omenjena področja smo imeli na voljo bronhoskopske slike zajete z belo svetlobo ter z autofluorescenčno svetlobo. Za področja smo imeli na voljo »ground truth« o razvrščanju tkiv v maligna/benigna na podlagi biopsije tkiva iz sumljivega področja, ki so bila patološko pregledana. V študijo smo vključili 44 sumljivih vzorcev, od katerih je bilo 22 malignih in 22 nemalignih.

Omenjene slike smo najprej obdelali, da smo na njih poiskali sumljiva področja. Sumljiva področja smo določili z metodo upravljanja razmerja rdečega in zelenega kanala avtofluorescenčne slike. Na sliki smo z algoritmi za iskanje robov in morfološkim zapiranjem področij določili sumljiva področja ter rezultate primerjali s področji, ki so jih na istih slikah ročno označili specialisti bronhoskopije.

V nadaljevanju smo za sumljiva področja izračunali nabor značilnk, ki so služile kot neodvisne spremenljivke v drugem koraku – razvrščanju vzorcev. Pripravili smo dva nabora značilnk. Za prvi nabor smo ponovili postopek, ki je že bil opisan v literaturi Bountris in sod. in je zajemal izračun 725 teksturnih značilnk, ter redukcijo njihove dimenzije z uporabo metode analize osnovnih komponent (PCA). Za drugi nabor smo izračunali naš predlog značilnk, ki je bil sestavljen iz parametrov dveh Gaussovih funkcij, s katerima smo aproksimirali potek histograma rdečega in zelenega kanala avtofluorescenčne slike. Omenjena nabora značilnk in pripadajočo »ground truth« klasifikacijo vzorcev smo uporabili za učenje različnih razvrščevalnikov.

Prvi korak v obdelavi slik: določanje sumljivih področij je dajal v primerjavi s področji, ki so jih določili specialisti, zadovoljive rezultate: kot narobe pozitivne (ang. False Positive) smo označili od 8,7 % do 11,1 % slikovnih elementov in kot narobe negativne (ang. False Negative) smo označili od 8,4 % do 11,0 % slikovnih elementov.

V naši raziskavi smo uspešno ponovili metodo razvrščanja vzorcev, ki so jo predlagali avtorji Bountris in sod. Ko smo v omenjeni raziskavi objavljene rezultate primerjali z rezultati, ki smo jih dobili z uporabo našega nabora značilnk smo ugotovili, da se na našem naboru vzorcev naša metoda obnaša bolje. Z različnimi algoritmi za grajenje razvrščevalnikov smo na Bountris-ovem in sod. naboru značilnk dosegli natančnost med 90,4 % in 92,1 %, na našem naboru značilnk pa natančnost od 90,9 % do 95,8 %.

Omenjeno raziskavo bi veljalo ponoviti na večjem vzorcu podatkov, da bi lahko identificirali vse morebitne težave, ki nastanejo pri vzorcih, ki precej odstopajo od vzorcev, ki smo jih imeli na voljo. Še vedno gre za metodo, ki lahko služi za razvoj podpornega orodja, ki bi omogočilo lažje delo specialistu bronhoskopije. Slabost omenjenega pristopa je tudi v tem, da je prilagojen za specifično napravo in bi zahteval prilagoditev na sorodne naprave.

Glavni prispevek omenjene metode je izboljšanje objavljene metodologije Bountris in sod. v smislu natančnosti in zmanjšanja kompleksnosti določanja značilnk.

Ključne besede: segmentacija slik, zaznavanje robov, autofluorescenčna bronhoskopija, razvrščanje, strojno učenje

Nov pristop k vzburjanju pri ultrazvočno podprtem obodnem brušenju

Vytautas Ostaševičius¹ – Vytautas Jūrėnas¹ – Andrius Vilkauskas¹ – Gytutas Balevičius^{1,*}
– Andrius Senkus² – Eglė Jotautienė²

¹ Tehniška univerza v Kaunasu, Inštitut za mehatroniko, Litva

² Univerza Aleksandrasa Stulginskisa, Inštitut za kmetijsko tehniko in varnost, Litva

Z naraščajočo uporabo trdih in krhkih materialov v industriji se povečuje tudi potreba po novih in učinkovitejših obdelovalnih postopkih, ki bi omogočali visoko stopnjo odvzema materiala v duktilnem režimu obdelave. Na tem področju vse bolj pridobiva na pomenu obdelava s podporo vibracij in zato obstaja potreba po razvoju in ustvarjanju novih, fleksibilnejših metod za prenos vibracij. Problem pri uvajanju teh metod je zahtevnost, saj so pri rotacijskih delih potrebna dodatna komutacijska vozlišča za napajanje pretvornikov v rotacijskem vmesniku.

Članek obravnava razvoj nove metode za prenos vibracij, ki jo je mogoče enostavno uporabiti pri rotacijskih delih v procesih kot so struženje, rezkanje, vrtanje in brušenje brez komutacijskih vozlišč, s čimer se zmanjša kompleksnost celotnega procesa. Predlagana konstrukcija se preprosto namesti na podporo rotacijskega vretena in naprava tako deluje zunaj rotacijskega stika.

V predlagani metodi je uporabljeno vzburjanje statične podpore rotacijskega dela namesto vzburjanja samega dela. Z analizo po metodi končnih elementov je bil razvit prototip in preizkušen na procesu obodnega brušenja. Eksperimentalna analiza je obsegala meritve s kontaktnim pospeškometerom na mirujočem obdelovancu in meritve profila površine po obdelavi.

Rezultat analize po metodi končnih elementov je bil pretvornik moči 400 W s profilom eksponentnega roga, ki lahko vzbuja obdelovanec z amplitudo 1,5 μm . Meritve s kontaktnim pospeškometerom so pokazale, da se vibracije prenašajo v skladu z rezultati modela za primer, ko se obdelovanec ne vrti. Dokazane so bile tudi opazne razlike v hrapavosti površine, obdelane s podporo vibracij in s konvencionalnim brušenjem. Iz tega sledi domneva, da se vibracije prenašajo tudi med procesom brušenja.

Predlagana metoda bi lahko pomembno prispevala k razširitvi metod obdelave s podporo vibracij v industriji. Zaradi občutnega zmanjšanja kompleksnosti procesa ter posledično večje prilagodljivosti in lažjega uvajanja bodo proizvajalci lažje nadgradili obstoječe proizvodne prakse s podporo vibracij ter si tako ustvarili prihranke pri rabi virov in povečali kakovost proizvodnje.

Predstavljena analiza je bila osredotočena zgolj na splošni prenos vibracij in manj na vpliv različnih konfiguracij parametrov vibracij na kakovost obdelave. Prihodnje raziskave bodo zato usmerjene v obravnavo teh odvisnosti in identifikacijo vpliva različnih vrst, amplitud in frekvence vibracij, hitrosti obdelave in konfiguracije orodij na površinsko hrapavost. S podrobno analizo teh odvisnosti bi bilo mogoče izkoristiti vse pozitivne vplive podpore vibracij pri konvencionalnih obdelovalnih procesih.

Ključne besede: podpora vibracij, brušenje, obdelava, prehod med krhkim in duktilnim stanjem, analiza po metodi končnih elementov, meritve profila površine

Izdelava plasti visokolegirane bele kromove jeklene litine na substratu nodularne litine z laserskim površinskim legiranjem

Damian Janicki*

Šlezijaska tehniška univerza, Fakulteta za strojništvo, Poljska

Nodularna litina je material, ki se pogosto uporablja v proizvodnji strojnih elementov v različnih panogah, kot so avtomobilska industrija, energetika, rudarstvo, obrambna industrija in kmetijska mehanizacija. V nekaterih primerih obstaja potreba po izboljšanju vzdržljivosti oz. obstojnosti strojnih elementov proti abrazivni in erozivni obrabi. Obetaven pristop k izboljševanju protiobrabnih lastnosti nodularne litine predstavljajo postopki laserske modifikacije površin, še posebej pa postopek laserskega površinskega legiranja (LSA). Postopek LSA omogoča natančno uravnavanje kemične sestave talilne kopeli in s tem prilagajanje površinskih lastnosti nodularne litine, npr. s formiranjem površinskih plasti visokolegirane bele kromove jeklene litine (HWSL). Znano je, da imajo visokolegirane bele kromove jeklene litine odlične protiobrabne lastnosti zaradi velikega volumskega deleža trdih primarnih in/ali evtektičnih karbidov M_7C_3 ter žilave matice. Več raziskovalcev je poročalo o oblikovanju tovrstnih kompozitnih struktur s površinskim legiranjem različnih vrst železove litine, malo pa je raziskav, ki bi preučevale formiranje HWSL na nodularni litini s sistemi za lasersko legiranje, ki uporabljajo laserski izvor z enakomernim intenzivnim profilom žarka in neposredno vbrizgavanje legirnega prahu v talilno kopele.

V predstavljeni študiji so bile na substratu nodularne litine EN-GJS-700-2 izdelane plasti HWSL po postopku površinskega legiranja z diodnim laserjem in neposrednim vbrizgavanjem čistega kromovega prahu v talilno kapele. Diodni laser je oddajal snop pravokotnega preseka $1,5 \text{ mm} \times 6,6 \text{ mm}$ s konstantno porazdelitvijo intenzitete (profil v obliki cilindra). Glavni cilj študije je bil preučiti vpliv parametrov laserskega legiranja na oblikovanje mikrostrukture v plasteh HWSL. Mikrostruktura HWSL je bila analizirana po postopku vrstične elektronske mikroskopije (SEM) z energijsko disperzivno spektroskopijo (EDS) in rentgensko difrakcijo (XRD).

Rezultati so pokazali, da je v sestavi enakomerno legiranih plasti HWSL do 14,4 ut. % Cr. Debelina plasti HWSL je znašala do 1,1 mm, mikrostruktura visokolegirane bele kromove jeklene litine pa je bila podevtektična in evtektična. Podevtektična mikrostruktura HWSL vsebuje dendrite primarnega avstenita (γ_p) in evtektična območja, sestavljena iz evtektičnih karbidov (M_3C ali M_7C_3 , odvisno od vsebnosti kroma) in evtektične faze avstenita (γ_e). Neravnotežni pogoji ohlajanja talilne kopeli in dodatek kroma v splošnem ovirajo martenzitno premeno. Na vrsto in morfologijo evtektičnih karbidov vplivajo koncentracija kroma v talilni kopeli in pogoji strjevanja. Z naraščanjem vsebnosti kroma se povečuje delež evtektičnih območij v podevtektičnih plasteh HWSL in evtektični karbidi se postopoma zmanjšujejo. Ko je bila celotna vsebnost kroma v HWSL večja od 10 ut. %, so bila evtektična območja sestavljena praktično samo iz $\gamma_e + M_7C_3$. Vsebnost kroma nad 12 ut. % zagotavlja oblikovanje evtektične mikrostrukture ($\gamma_e + M_7C_3$) po celotni legirani plasti. V evtektičnih plasteh HWSL karbidi evtektičnega tipa M_7C_3 rastejo kot kolonije evtektika. Premer kolonij evtektika je bil v razponu $4 \mu\text{m}$ do $10 \mu\text{m}$. Karbidi M_7C_3 v kolonijah so bili fine paličaste (vlaknene) oblike v središču kolonij ter nekoliko bolj grobi in lamelarne oblike ob robu. Povprečni premer paličic karbida v središču kolonij je bil pribl. 180 nm , volumski delež karbidov v kolonijah pa je bil ocenjen na pribl. $52 \pm 4,5 \%$. Na povprečno trdoto HWSL je vplivala predvsem oblika karbidnih izločkov, znašala pa je 675 HV v podevtektičnih oz. 650 HV v evtektičnih območjih.

Ključne besede: visokolegirana bela kromova jeklena litina, nodularna litina, lasersko legiranje površine, diodni laser, mikrostruktura, evtektični karbidi

Hitro in samodejno umerjanje pogreška ničelne točke pri paralelnem robotu z dvema prostostnima stopnjama na podlagi novega merilnega mehanizma

Jiangping Mei – Jiawei Zang – Yabin Ding* – Shenglong Xie – Xu Zhang

Univerza v Tianjinu, Državni laboratorij za teorijo mehanizmov in konstruiranje, Kitajska

Pogreški ničelnih točk predstavljajo veliko grožnjo za natančnost pozicioniranja paralelnih robotov, v praksi pa so lahko posledica napak v krmiljenju, trkov ali zrahljanih zgibov. Za točnost pozicioniranja je torej treba odpraviti pogreške ničelnih točk takrat, ko se pojavijo. Umerjanje pogreška ničelnih točk je praktičen in ekonomičen način za odpravo vpliva pogreška na natančnost pozicioniranja in ga je na splošno mogoče opraviti v štirih zaporednih korakih: modeliranje napak, meritve, identifikacija in kompenzacija. Pristopi k umerjanju se delijo na tiste na osnovi koordinat in tiste na osnovi razdalje. Prednost slednjega je v tem, da je invarianten na izbrani referenčni koordinatni sistem.

Omeniti je treba, da se merilni proces običajno izvaja z velikimi merilnimi napravami, ki so drage in neprikladne za uporabo, proces identifikacije pa običajno poteka po metodi najmanjših kvadratov. Če se pogreški ničelnih točk identificirajo skupaj s preveč geometrijskimi napakami, lahko strmo naraste število pogojev identifikacijske matrike in pojavi se nelinearen problem slabe pogojenosti modela identifikacije. Za razrešitev tega problema sta v članku predlagana nov merilni mehanizem in model za identifikacijo pogreška ničelne točke.

Merilni mehanizem je sestavljen iz dveh tečajev, dveh vodilnih palic, nosilne palice in linearne skale. S premikom platforme v več merilnih položajev je mogoče samodejno izmeriti spremembe razdalje med tečajema merilnega mehanizma in jih nato prenesti v model za hitro umerjanje pogreška ničelne točke v krmilniku robota. Merilni mehanizem uporablja model za identifikacijo pogreška ničelne točke na osnovi razdalje. Identifikacijski model je bil za razrešitev nelinearnega problema slabe pogojenosti identifikacijske matrike odrezan po metodi odrezanega singularnega razcepa (TSVD) na podlagi rezultatov analize občutljivosti virov napak. Model je bil nato za zagotovitev točnosti po rezanju še prilagojen za napake v izdelavi in montaži merilnega mehanizma (MAEMM).

Merilni mehanizem je v primerjavi z velikimi merilnimi napravami prikladnejši za uporabo ter omogoča pravočasne in stroškovno ugodne meritve. Metoda TSVD razrešuje problem slabe pogojenosti identifikacijskega modela, sam model, prilagojen s predhodnimi rezultati identifikacije MAEMM, pa izboljšuje možnost identifikacije pogreškov ničelnih točk. Optimizacijski pristop k izbiri merilnih položajev omogoča največjo učinkovitost meritev in dodatno izboljšanje identifikabilnosti. Rezultati simulacij in eksperimentalne analize umerjanja kažejo, da ima identifikacijski model dobro identifikabilnost in robustnost, napaka pozicioniranja po umerjanju pa je bistveno manjša. Predlagani merilni mehanizem in metoda za umerjanje pogreška ničelne točke sta uporabna tudi za umerjanje drugih ravninskih ali prostorskih paralelnih robotov.

Delovni prostor prostorskih paralelnih robotov je običajno cilindrične oblike. Če bo predlagani merilni mehanizem v prihodnje uporabljen za umerjanje paralelnih robotov, bi bilo tečaja bolje zamenjati s homokinetičnimi ali kroglastimi zgibi, ki omogočajo ustrežnejšo izbiro merilnih položajev.

Ključne besede: paralelni robot, umerjanje, pogrešek ničelne točke, merilni mehanizem, metoda odrezanega singularnega razcepa, optimalen merilni položaj

RONNA G3: nov robotski nevronavigacijski sistem

Marko Švaco^{1,2,*} – Bojan Šekoranja^{1,2} – Filip Šuligoj^{1,2} – Josip Vidaković^{1,2} – Bojan Jerbić^{1,2} – Darko Chudy^{3,4}

¹ Univerza v Zagrebu, Fakulteta za strojništvo in ladjedelništvo, Hrvaška

² Sodelavec Zavoda za nevrokirurgijo, Klinična bolnišnica Dubrava, Hrvaška

³ Zavod za nevrokirurgijo, Klinična bolnišnica Dubrava, Hrvaška

⁴ Hrvaški inštitut za raziskave možganov, Univerza v Zagrebu, Medicinska fakulteta, Hrvaška

V članku je predstavljen nov robotski nevronavigacijski sistem RONNA G3, ki je izdelan na osnovi standardnih industrijskih robotov in razvit za stereotaktično navigacijo brez okvirja. Sistem RONNA G3 je sestavljen iz dveh robotskih rok, nameščenih na posebnih univerzalnih mobilnih platformah, globalnega optičnega sledilnega sistema (OTS) in programske opreme za načrtovanje. Za registracijo pacienta so uporabljeni označevalci (toga referenčna oznaka ali poljubno razporejene referenčne oznake na kosti), za lokalizacijo pacienta v fizičnem prostoru pa je uporabljen stereovizijski sistem (RONNAstereo). RONNAstereo ima dve infrardeči (IR) kameri z makroobjektivom, poravnani pod kotom 55° v isti ravnini. Robota sta opremljena s kirurškimi inštrumenti (vodila, prijemala, sveder itd.). Lastnost, po kateri se sistem RONNA G3 razlikuje od večine drugih sodobnih robotskih nevrokirurških sistemov, je dodatna mobilna platforma, opremljena s podajno in občutljivo robotsko roko. RONNA G3 je tako dvoročni robotski sistem.

Natančnost delovanja sistema RONNA G3 je bila ovrednotena v študiji na fantomu z dvema različnima metodama registracije. Pri vrednotenju natančnosti in vitro je bila natančnost pozicioniranja sistema RONNA G3 izmerjena na posebnem testnem fantomu. Ta je sestavljen iz polimernega podnožja z enim osrednjim stebrom, 16 naključno porazdeljenih sferičnih referenčnih oznak in ene toge referenčne oznake. Metodi registracije (s togo oznako in poljubno razporejenimi referenčnimi oznakami) sta bili ovrednoteni z registracijo vsake slike CT iz slikovnega v fizični prostor. V prvem primeru je bila za opredelitev koordinatnega sistema fantoma uporabljena toga referenčna oznaka na fantomu, v drugem primeru pa tri naključno razporejene sferične referenčne oznake, pritrjene s kostnimi vijaki. Druga metoda omogoča v klinični praksi spreminjanje velikosti oznak in približevanje registriranega koordinatnega sistema tarčam. Ugotovljene so bile napake pozicioniranja tarč (TPE) za 10 poljubnih položajev in orientacij fantoma v delovnem prostoru robota. Meritev je bila ponovljena za vsako od treh slik CT.

Absolutna natančnost pozicioniranja sistema RONNA G3 oz. napaka pozicioniranja je bila ovrednotena za dve različni skupini tarč: površinske (< 50 mm) in globoke (> 50 mm). Delitev se nanaša na koordinato z tarče v koordinatnem sistemu toge referenčne oznake oz. poljubno razporejenih sferičnih referenčnih oznak. Tako pri površinskih kot pri globokih tarčah je bila ugotovljena signifikantna razlika v natančnosti pozicioniranja, tako pri srednji (0,43 mm in 0,88 mm) kot pri največji napaki (1,36 mm in 1,89 mm). Natančnost z napako pod 0,5 mm, ki zadošča zahtevam za stereotaktične posege, je dosegljiva, če se tarče nahajajo v bližini koordinatnega sistema označevalca (< 50 mm). Sistem je bil na osnovi napak pozicioniranja v preizkusih s fantomom pripravljen za klinične preiskave, ki trenutno še potekajo.

RONNA G3 je nov nevronavigacijski robotski sistem, ki bo uporaben kot dovršeno orodje za nevrokirurge pri intraoperacijskem načrtovanju in natančni nevronavigaciji brez okvirja. Nevrokirurški robotski sistem RONNA G3 zagotavlja vrsto prednosti v kirurških posegih, kot so odprava tresljajev, manjše tveganje napak zaradi kirurgove utrujenosti in hitrejši potek operacije. Sistem RONNA G3 se razlikuje od sodobnih robotskih nevronavigacijskih sistemov za nevrokirurške posege po dveh pglavitnih lastnostih. Prva je, da gre za namensko univerzalno mobilno platformo, ki lahko sprejme različne vrste robotov, druga pglavitna lastnost pa je novi visokonatančni brezkontaktni sistem za lokalizacijo RONNAstereo. RONNA G3 poleg tega uporablja nov samodejni algoritem, ki je bil razvit za izboljšanje lokalizacije sferičnih referenčnih oznak pred operacijo.

Ključne besede: robotska nevronavigacija, stereotaksija brez okvirja, minimalno invazivna kirurgija, RONNA G3, natančnost, fantom

Nova aksialna modifikacija in simulacijska analiza čelnega evolventnega zobnika

Ningning Wang – Xueyi Li* – Kun Wang – Qingliang Zeng – Xiao Shen

Znanstveno-tehniška univerza v Shandongu, Kolidž za strojništvo in elektroniko, Kitajska

Pri čelnih zobniških prenosih lahko nastopi neenakomerna porazdelitev obremenitev zaradi napak v obdelavi in montaži, elastičnih deformacij in drugih dejavnikov, posledično pa se močno zmanjša obremenljivost in skrajša življenjska doba zobnikov. Najučinkovitejša rešitev za omenjene težave je aksialna modifikacija, kjer se s spremembo površine zoba popravi oblika in položaj kontaktne površine.

Različne modifikacije se razlikujejo po učinkovitosti in zato je zelo pomembna izbira optimalne metode modifikacije zobniških dvojic. Poleg tega se oblika površine zoba z aksialno modifikacijo razlikuje od površine standardnega evolventnega zoba in zato je težko natančno oceniti vpliv modifikacije na zobniško dvojico. Sledi sklep, da je treba preučiti teorijo modifikacij, poiskati nov pristop in ovrednotiti zmogljivost modificiranega zobnika. Za razrešitev naštetih problemov ter izboljšanje kontaktnih pogojev, učinkovitosti ubiranja in obremenljivosti zobniških dvojic je predlagana nova metoda aksialne modifikacije na podlagi sestavljene modifikacijske krivulje. Iz modifikacijske krivulje je bila izpeljana enačba, ki določa obliko površine modificiranega zoba.

Za ovrednotenje zmogljivosti modificirane zobniške dvojice je bil izdelan natančen model dvojice po metodi končnih elementov na podlagi interpolacije s kubičnim B-zlepkom. Sledila je simulacijska analiza, v kateri je bil določen učinek modifikacije s pomočjo vrednosti kontaktnih napetosti, upogibnih napetosti in deformacij zob ter z opazovanjem stanja kontaktne površine. Modifikacijski parametri so bili optimizirani z ortogonalnimi eksperimenti za modificirano zobniško dvojico in tako je bil določen optimalen učinek modifikacije v izbranih delovnih pogojih. Za validacijo metode je bila uporabljena zobniška dvojica iz avtomobilskega menjalnika, ki je bila modificirana po predlagani metodi. Rezultati analize kažejo občutno izboljšanje problema neenakomerne porazdelitve obremenitev po modifikaciji zobniške dvojice z optimiziranimi parametri, kakor tudi izboljšanje obremenljivosti zobniške dvojice. Opravljena je bila tudi primerjava zobniških dvojic, modificiranih po univerzalni in optimizirani metodi.

Rezultati primerjave kažejo, da je predlagana metoda modifikacije bolj prilagodljiva od univerzalne metode. Končno je bila preverjena še učinkovitost in praktičnost predlagane metode s testi na zobniških dvojicah, ki so bile izdelane v ta namen. Predstavljeno delo odpravlja določene pomanjkljivosti obstoječih študij z novo metodo modifikacije in vrednotenjem njenega učinka. Parametri modifikacije so bili optimizirani z izvedbo ortogonalnega eksperimenta, v katerem so bili določeni primerni parametri za različne zobniške dvojice.

Predlagana metoda je uporabna za konstruiranje in optimizacijo zobnikov za učinkovitejši prenos in zmanjšanje stroškov. Metoda je trenutno primerna le za čelne zobniške prenose, v prihodnje pa bo razširjena še na zobnike s poševnim ozobjem in na analizo utrujanja.

Ključne besede: neenakomerna porazdelitev obremenitev, aksialna modifikacija, simulacijska analiza, kontaktna površina, učinek modifikacije, optimizacija

Analiza kontinuirnih sendvič plošč s profiliranim plaščem

Metod Čuk¹ – Franc Kosel¹ – Nenad Zrnić² – Boris Jerman^{1,*}

¹ Fakulteta za strojništvo, Univerza v Ljubljani, Slovenija

² Univerza v Beogradu, Fakulteta za strojništvo, Srbija

Uporaba numeričnih simulacij pri obravnavi strukturnega obnašanja strešnih kontinuirnih sendvič plošč (s profiliranim plaščem) pri prečni obtežbi in velikih razponih še vedno predstavlja izziv. Ob velikih dimenzijah konstrukcije in glede na obravnavano konfiguracijo (vrsta podpiranja, način obtežbe) so opazovani pojavi navadno zelo lokalni in zahtevajo zelo detajlno izdelan model.

Obravnavane lahke sendvič plošče so navadno sestavljene iz treh medsebojno zlepljenih plasti: dve zunanji tanki plasti sestavljata plašč iz jeklene pločevine; debela srednja plast toplotno izolativnega polnila iz mineralne volne pa tvori lahko jedro. Takšen lahek sovprežni element ima relativno visoko nosilnost in upogibno togost, varuje pred okoljskimi vplivi (veter, dež, itd.) ter zagotavlja toplotno in zvočno izolativnost. Pri uporabi za strešno kritino, kjer je pri večjih razponih zahtevana višja upogibna nosilnost in togost, pa je ena od krovnih pločevin globoko profilirana.

Cilj raziskave je bilo ugotoviti oz. potrditi ustreznost numerične simulacije pri obravnavi dejanskih konstrukcijskih primerov iz prakse. Za obravnavan primer strešne sendvič plošče z notranjo globoko trapezno profilirano krovno pločevino in gladko zunanjo krovno pločevino v obravnavani konfiguraciji – dvopoljna izvedba velikega razpona s prečno obtežbo – primarni način odpovedi nastopi v obliki gubanja (notranje) krovne pločevine neposredno nad srednjo (tlačno) podporo. V literaturi navedeni načini obravnave tega statično nedoločene problema temeljijo na izkustvenih enačbah, analitičen pristop z uporabo teorije linijskih upogibnih elementov namreč ni uspešen – upoštevati je potrebno tudi upogibno togost plašča ter tlačno porazdelitev med sendvič ploščo in vmesno podporo. Verjetnost, da bi bilo mogoče v okviru teoretične obravnave zajeti vse vplive z zadostno natančnostjo, je zelo majhna, zato je nujnost eksperimentalne obravnave nesporna.

V praksi je eksperimentalna obravnava posameznih primerov zahtevna (laboratorij, merilna oprema, osebje, priprava preizkusa, meritev, analiza, itd.), zato je uporaba numeričnih simulacij dobrodošla. Za obravnavan primer strešnega panela je bila izdelana testna konfiguracija in izvedene meritve na prirejenem preizkuševališču za izvajanje standardnega upogibnega preizkusa sendvič plošč. Prečna obtežba je bila izvedena z uporabo hidravličnega valja (preko razdelilnega mehanizma). Nameščena sta bila senzorja za spremljanje velikosti obtežbe in povesa. Z namenom spremljanja napetostnega stanja so bili na kritičnem mestu sendvič plošče nad srednjo podporo na ustreznih mestih (na spodnjo in zgornjo površino) notranje krovne pločevine nameščeni merilni lističi. Izdelan je bil numerični model testne konfiguracije z uporabo metode končnih elementov. V okviru modela so bili uporabljeni prostorski in ploskovni elementi (jedro in plašč) z ustreznimi materialnimi lastnostmi (podanimi s strani proizvajalca sendvič plošč) ter robnimi pogoji.

Rezultati simulacije se dobro ujemajo z rezultati preskusov; v območju pred odpovedjo relativna razlika pri povesu znaša do 5 %, razlika med izmerjeno in izračunano nosilnostjo pa ne presega 7 %. Zadovoljivo je tudi ujemanje med izračunanimi in izmerjenimi rezultati upogibnih napetostih v notranji krovni pločevini.

Opisano ujemanje potrjuje ustreznost uporabe numeričnih simulacij pri praktični analizi strukturnega obnašanja nosilnih elementov sovprežnih konstrukcij in podpira uporabo numerične simulacije za analizo mejnih stanj v podobnih primerih, še posebej tam, kjer uporaba analitičnih metod ni mogoča in alternativo predstavlja le eksperimentalna obravnava, ki je navadno (finančno in časovno) potratnejša.

Ključne besede: testiranje, metoda končnih elementov, analiza konstrukcije, sendvič konstrukcija, globoko profiliran plašč, mineralna volna, način odpovedi

DOKTORSKE DISERTACIJE

Na Fakulteti za strojništvo Univerze v Ljubljani sta obranila svojo doktorsko disertacijo:

- dne 8. novembra 2017 **Luka SKRINJAR** z naslovom: »Metoda absolutnih vozliščnih koordinat v dinamiki sistema togih teles z vključitvijo kontaktnih razmer« (mentor: izr. prof. dr. Janko Slavič);

Raziskava predstavlja pristop k reševanju dinamskih sistemov, ki so sestavljeni iz togih in prožnih teles ter povezani z ustreznimi kinematičnimi povezavami. Za določitev dinamskega odziva je razvita in numerično ter eksperimentalno ovrednotena kinematična povezava čepa v vodilu z zračnostjo, ki je nato uporabljena pri izdelavi dinamskega sestava, sestavljenega iz togih in prožnih teles. Obravnavani dinamski model, ki temelji na realni inženirski aplikaciji, je uporabljen v procesu analize vpliva prednapetja na dinamski odziv;

- dne 22. novembra 2017 **Luka KNEZ** z naslovom: »Dinamska karakterizacija sistema dlan-roka ter njegova vibroizolacijska zaščita« (mentor: prof. dr. Miha Boltežar, somentor: izr. prof. dr. Janko Slavič);

Raziskava predstavi pregled potrebne teorije in standardov za raziskovanje biodinamičnega odziva telesa ter njegove vibroizolacijske zaščite. V prvem delu sta razviti dve različni biodinamični merilni napravi. Prva je zasnovana kot ročaj in ločeno ter sočasno zajema odzive dlani in prstov na vibracijsko vzbujanje. Naprava omogoča izvajanje meritev v vseh treh smereh prostora, lahko se jo tudi uporablja za preverjanje učinkovitosti antivibracijskih rokavic. Druga naprava pa je bila razvita z namenom izvajanja meritev biodinamičnega odziva posameznih prstov in delov prstov. Na podlagi pomejenih rezultatov je nato razvit in tudi validiran dinamski model kazalca. Model prsta je zasnovan kot sistem togih teles, materialni podatki modela pa so bili identificirani na osnovi eksperimentalnih podatkov. Razviti model služi kot simulator odziva prsta na vzbujanje in ob dodatnih vibroizolacijskih elementih omogoča razvoj in testiranje antivibracijske zaščite človeških rok. Na koncu so s pomočjo nadgrajenega modela prsta raziskani še različni vibroizolacijski materiali in podani predlogi antivibracijske zaščite.

Na Fakulteti za strojništvo Univerze v Mariboru je obranil svojo doktorsko disertacijo:

- dne 20. novembra 2017 **Darko JAGARINEC** z naslovom: »Vpliv zaostalih napetosti na rast utrujenostne razpoke v upognjenem delu podnice tlačne posode« (mentor: prof. dr. Nenad Gubelj);

Postopek izdelave podnice ustvarja kompleksno deformacijsko-napetostno stanje, ki ga ni možno enostavno prenesti v laboratorijske pogoje testiranja. V nalogi smo pokazali, da s predhodnim upogibanjem in nato nateznim obremenjevanjem ustvarimo sestavljeno napetostno stanje, ki ga je možno analizirati le v eni kritični točki na notranji strani upognjenca. Z numeričnim modeliranjem napetostnega stanja smo se približali eksperimentalno določenim razmeram med utrujanjem s kombiniranim obremenjevanjem pred-deformiranih vzorcev. Na osnovi opravljenih numeričnih analiz, ki so bile podprte z eksperimentalnim testiranjem, kako v procesu upogibanja s tremi različnimi stopnjami pred deformacije tako tudi v procesu cikličnega natezno-upogibnega obremenjevanja z različnimi amplitudami sil in ob upoštevanju spremembe amplitude in napetostnega razmerja, smo dobili vrednosti dinamične trdnosti skladne s S-N Wohlerjevim diagramom. S tem smo potrdili, da je v doktorski disertaciji predstavljen postopek in model pravilen za določitev dejanskih napetostnih razmer v pred-deformiranih upognjenih vzorcih. V doktorski nalogi je pokazano, da zaostale napetosti v metastabilnem avstenitu AISI 316L, ki so posledice deformacije in fazne transformacije v martenzitno mikrostrukturo, vplivajo na iniciacijo in širjenje utrujenostnih razpok, pri čemer se napetostno razmerje v materialu razlikuje od razmerja sil R utrujanja zaradi teh zaostalih napetosti R_s . To smo pokazali na osnovi določitve napetostnega stanja z numeričnim modeliranjem in z eksperimentalno dobljenimi vrednostmi na S-N Wöhlerjevi krivulji, ki se ujemajo z rezultati upogibnega utrujanja ploščatih preizkušancev s polkrožnim utorom.



V spomin prof. dr. Ivanu Prebilu

V torek, 31. oktobra 2017, se je za vedno poslovil naš dolgoletni sodelavec in predstojnik Katedre za modeliranje v tehniki in medicini, spoštovani učitelj, mentor, vzornik in prijatelj prof. dr. Ivan Prebil.

Profesor Ivan Prebil se je rodil 7. oktobra 1952 v Šmarju pri Jelšah. Po zaključku osnovne in srednje šole je šolanje nadaljeval na Fakulteti za strojništvo v Ljubljani, kjer je leta 1985 doktoriral pod mentorstvom prof. dr. Radislava Pavletiča na področju motorjev z notranjim zgorevanjem. Po izvolitvi v naziv docent leta 1988 je bil leta 1996 izvoljen še v naziv izredni profesor za Konstruiranje delovnih strojev in Toplotne batne stroje, leta 2003 pa je postal redni profesor za področje Konstruiranje strojev. Vse od leta 1994 je bil vodja Laboratorija za modeliranje elementov in konstrukcij, ki ga je sam ustanovil. Leta 2005 je na Fakulteti ustanovil še Katedro za modeliranje v tehniki in medicini in istoimensko Programsko skupino pri Agenciji za raziskovalno dejavnost Slovenije ter jo uspešno vodil 12 let vse do njegovega prezgodnjega odhoda. V želji po še tesnejšem sodelovanju s slovenskimi podjetji je ustanovil in vodil tudi Tehnološki center za modeliranje elementov in konstrukcij – CEMEK.

Prof. dr. Ivan Prebil je bil raziskovalno aktiven najprej na področju motorjev z notranjim izgorevanjem in potem dolga leta na področju konstruiranja ter na področju prometne varnosti. V slovenski prostor je med prvimi uvajal računalniške metode avtomatiziranega vodenja konstrukcijskih oziroma razvojnih procesov, npr. na področju velikih nosilnih vrtljivih zvez ter avtomatizirane izdelave in vodenja tehnične dokumentacije v številnih projektih v sodelovanju s slovensko in tudi tujo industrijo. Aktivno je sodeloval pri prehodu Slovenije na ISO-standardizacijo na tem področju. Kasneje je uvajal najnovejše računalniške metode analiz prometnih nezgod in na tem področju izvajal tudi sistematično izobraževanje slovenskih izvedencev za prometne nezgode ter drugih udeležencev pri teh nalogah. Na podlagi njegovih prizadevanj za izboljšanje sodnega izvedenstva v Sloveniji in velikih dosežkov je bil izbran tudi za predsednika Združenja sodnih izvedencev za raziskavo prometnih nezgod. Bil je pobudnik tesnejšega povezovanja tehniške in medicinske stroke na področju trčne biomehanike. V slovenskem prostoru je pionirsko opravljal raziskave dinamike in obremenitev človeškega telesa v pogojih trka ter se pri tem uspešno vključil v mednarodne tokove.

Objavil je več kot 90 znanstvenih člankov v najuglednejših znanstvenih revijah, prek 170 prispevkov na mednarodnih konferencah in dva univerzitetna učbenika. Odmevnost objavljenih del je dosegla preko 600 citatov, Hirschev indeks pa je 13. Nova raziskovalna spoznanja je vseskozi uspešno prenašal v domačo in tujo industrijo. Sodeloval je tudi z več univerzami in inštituti doma in v tujini. Uspešno je deloval kot član predsedstva Evropskega združenja za raziskavo in analizo prometnih nezgod EVU in pripomogel k njegovi vseevropski širitvi in uveljavitvi. Bil je tudi član svetovnega združenja avtomobilske industrije FISITA in član predsedstva evropske skupine AREC za eksperimentalne raziskave prometnih nezgod.

Prof. dr. Ivan Prebil je bil utemeljitelj študijskega programa »Sistemi prometne varnosti« na Fakulteti za strojništvo, organizator in soorganizator desetih mednarodnih konferenc v okviru EVU in šestih zahtevnih testiranj preskusnih trkov v okviru skupine AREC, nosilec nacionalnih projektov ARRS in Ministrstva za gospodarstvo ter soavtor patenta.

Profesor Ivan Prebil je bil cenjen kolega med ožjimi in širšimi sodelavci na Fakulteti za strojništvo in širše v Sloveniji kot tudi v tujini. Sodelavci Katedre za modeliranje v tehniki in medicini smo imeli čast spremljati njegovo strokovno pot, se pri njem učiti in z njim uspešno sodelovati. Bil je potrpežljiv vodja, učitelj in mentor, katerega bomo ohranili v najlepšem spominu.

Sodelavci Katedre za modeliranje v tehniki in medicini
Fakulteta za strojništvo Univerze v Ljubljani

Information for Authors

All manuscripts must be in English. Pages should be numbered sequentially. The manuscript should be composed in accordance with the Article Template given above. The maximum length of contributions is 10 pages. Longer contributions will only be accepted if authors provide justification in a cover letter. For full instructions see the Information for Authors section on the journal's website: <http://cn.sv-jme.eu>.

SUBMISSION:

Submission to SV-JME is made with the implicit understanding that neither the manuscript nor the essence of its content has been published previously either in whole or in part and that it is not being considered for publication elsewhere. All the listed authors should have agreed on the content and the corresponding (submitting) author is responsible for having ensured that this agreement has been reached. The acceptance of an article is based entirely on its scientific merit, as judged by peer review. Scientific articles comprising simulations only will not be accepted for publication; simulations must be accompanied by experimental results carried out to confirm or deny the accuracy of the simulation. Every manuscript submitted to the SV-JME undergoes a peer-review process.

The authors are kindly invited to submit the paper through our web site: <http://ojs.sv-jme.eu>. The Author is able to track the submission through the editorial process - as well as participate in the copyediting and proofreading of submissions accepted for publication - by logging in, and using the username and password provided.

SUBMISSION CONTENT:

The typical submission material consists of:

- A **manuscript** (A PDF file, with title, all authors with affiliations, abstract, keywords, highlights, inserted figures and tables and references),
- Supplementary files:
 - a **manuscript** in a WORD file format
 - a **cover letter** (please see instructions for composing the cover letter)
 - a ZIP file containing **figures** in high resolution in one of the graphical formats (please see instructions for preparing the figure files)
 - possible **appendices** (optional), cover materials, video materials, etc.

Incomplete or improperly prepared submissions will be rejected with explanatory comments provided. In this case we will kindly ask the authors to carefully read the Information for Authors and to resubmit their manuscripts taking into consideration our comments.

COVER LETTER INSTRUCTIONS:

Please add a **cover letter** stating the following information about the submitted paper:

1. **Paper title**, list of **authors** and their **affiliations**.
2. **Type of paper**: original scientific paper (1.01), review scientific paper (1.02) or short scientific paper (1.03).
3. A **declaration** that neither the manuscript nor the essence of its content has been published in whole or in part previously and that it is not being considered for publication elsewhere.
4. State the **value of the paper** or its practical, theoretical and scientific implications. What is new in the paper with respect to the state-of-the-art in the published papers? Do not repeat the content of your abstract for this purpose.
5. We kindly ask you to suggest at least two **reviewers** for your paper and give us their names, their full affiliation and contact information, and their scientific research interest. The suggested reviewers should have at least two relevant references (with an impact factor) to the scientific field concerned; they should not be from the same country as the authors and should have no close connection with the authors.

FORMAT OF THE MANUSCRIPT:

The manuscript should be composed in accordance with the Article Template. The manuscript should be written in the following format:

- A **Title** that adequately describes the content of the manuscript.
- A list of **Authors** and their **affiliations**.
- An **Abstract** that should not exceed 250 words. The Abstract should state the principal objectives and the scope of the investigation, as well as the methodology employed. It should summarize the results and state the principal conclusions.
- 4 to 6 significant **key words** should follow the abstract to aid indexing.
- 4 to 6 **highlights**: a short collection of bullet points that convey the core findings and provide readers with a quick textual overview of the article. These four to six bullet points should describe the essence of the research (e.g. results or conclusions) and highlight what is distinctive about it.
- An **Introduction** that should provide a review of recent literature and sufficient background information to allow the results of the article to be understood and evaluated.
- A **Methods** section detailing the theoretical or experimental methods used.
- An **Experimental section** that should provide details of the experimental set-up and the methods used to obtain the results.
- A **Results** section that should clearly and concisely present the data, using figures and tables where appropriate.
- A **Discussion** section that should describe the relationships and generalizations shown by the results and discuss the significance of the results, making comparisons with previously published work. (It may be appropriate to combine the Results and Discussion sections into a single section to improve clarity.)
- A **Conclusions** section that should present one or more conclusions drawn from the results and subsequent discussion and should not duplicate the Abstract.
- **Acknowledgement** (optional) of collaboration or preparation assistance may be included. Please note the source of funding for the research.
- **Nomenclature** (optional). Papers with many symbols should have a nomenclature that defines all symbols with units, inserted above the references. If one is used, it must contain all the symbols used in the manuscript and the definitions should not be repeated in the text. In all cases, identify the symbols used if they are not widely recognized in the profession. Define acronyms in the text, not in the nomenclature.
- **References** must be cited consecutively in the text using square brackets [1] and collected together in a reference list at the end of the manuscript.
- **Appendix(-ices)** if any.

SPECIAL NOTES

Units: The SI system of units for nomenclature, symbols and abbreviations should be followed closely. Symbols for physical quantities in the text should be written in italics (e.g. v , T , n , etc.). Symbols for units that consist of letters should be in plain text (e.g. ms^{-1} , K , min , mm , etc.). Please also see: <http://physics.nist.gov/cuu/pdf/sp811.pdf>.

Abbreviations should be spelt out in full on first appearance followed by the abbreviation in parentheses, e.g. variable time geometry (VTG). The meaning of symbols and units belonging to symbols should be explained in each case or cited in a **nomenclature** section at the end of the manuscript before the References.

Figures (figures, graphs, illustrations digital images, photographs) must be cited in consecutive numerical order in the text and referred to in both the text and the captions as Fig. 1, Fig. 2, etc. Figures should be prepared without borders and on white grounding and should be sent separately in their original formats. If a figure is composed of several parts, please mark each part with a), b), c), etc. and provide an explanation for each part in Figure caption. The caption should be self-explanatory. Letters and numbers should be readable (Arial or Times New Roman, min 6 pt with equal sizes and fonts in all figures). Graphics (submitted as supplementary files) may be exported in resolution good enough for printing (min. 300 dpi) in any common format, e.g. TIFF, BMP or JPG, PDF and should be named Fig1.jpg, Fig2.tif, etc. However, graphs and line drawings should be prepared as vector images, e.g. CDR, AI. Multi-curve graphs should have individual curves marked with a symbol or otherwise provide distinguishing differences using, for example, different thicknesses or dashing.

Tables should carry separate titles and must be numbered in consecutive numerical order in the text and referred to in both the text and the captions as Table 1, Table 2, etc. In addition to the physical quantities, such as t (in italics), the units [s] (normal text) should be added in square brackets. Tables should not duplicate data found elsewhere in the manuscript. Tables should be prepared using a table editor and not inserted as a graphic.

REFERENCES:

A reference list must be included using the following information as a guide. Only cited text references are to be included. Each reference is to be referred to in the text by a number enclosed in a square bracket (i.e. [3] or [2] to [4] for more references; do not combine more than 3 references, explain each). No reference to the author is necessary.

References must be numbered and ordered according to where they are first mentioned in the paper, not alphabetically. All references must be complete and accurate. Please add DOI code when available. Examples follow.

Journal Papers:

Surname 1, Initials, Surname 2, Initials (year). Title. Journal, volume, number, pages, DOI code.

- [1] Hackenschmidt, R., Alber-Laukant, B., Rieg, F. (2010). Simulating nonlinear materials under centrifugal forces by using intelligent cross-linked simulations. *Strojniški vestnik - Journal of Mechanical Engineering*, vol. 57, no. 7-8, p. 531-538, DOI:10.5545/sv-jme.2011.013.

Journal titles should not be abbreviated. Note that journal title is set in italics.

Books:

Surname 1, Initials, Surname 2, Initials (year). Title. Publisher, place of publication.

- [2] Groover, M.P. (2007). *Fundamentals of Modern Manufacturing*. John Wiley & Sons, Hoboken.

Note that the title of the book is italicized.

Chapters in Books:

Surname 1, Initials, Surname 2, Initials (year). Chapter title. Editor(s) of book, book title. Publisher, place of publication, pages.

- [3] Carbone, G., Ceccarelli, M. (2005). Legged robotic systems. Kordić, V., Lazinica, A., Merdan, M. (Eds.), *Cutting Edge Robotics*. Pro literatur Verlag, Mammendorf, p. 553-576.

Proceedings Papers:

Surname 1, Initials, Surname 2, Initials (year). Paper title. Proceedings title, pages.

- [4] Štefanič, N., Martinčević-Mikić, S., Tošanović, N. (2009). Applied lean system in process industry. *MOTSP Conference Proceedings*, p. 422-427.

Standards:

Standard-Code (year). Title. Organisation. Place.

- [5] ISO/DIS 16000-6.2:2002. *Indoor Air - Part 6: Determination of Volatile Organic Compounds in Indoor and Chamber Air by Active Sampling on TENAX TA Sorbent, Thermal Desorption and Gas Chromatography using MSD/FID*. International Organization for Standardization. Geneva.

WWW pages:

Surname, Initials or Company name. Title, from <http://address>, date of access.

- [6] Rockwell Automation. Arena, from <http://www.arenasimulation.com>, accessed on 2009-09-07.

EXTENDED ABSTRACT:

When the paper is accepted for publishing, the authors will be requested to send an **extended abstract** (approx. one A4 page or 3500 to 4000 characters). The instruction for composing the extended abstract are published on-line: <http://www.sv-jme.eu/information-for-authors/>.

COPYRIGHT:

Authors submitting a manuscript do so on the understanding that the work has not been published before, is not being considered for publication elsewhere and has been read and approved by all authors. The submission of the manuscript by the authors means that the authors automatically agree to transfer copyright to SV-JME when the manuscript is accepted for publication. All accepted manuscripts must be accompanied by a Copyright Transfer Agreement, which should be sent to the editor. The work should be original work by the authors and not be published elsewhere in any language without the written consent of the publisher. The proof will be sent to the author showing the final layout of the article. Proof correction must be minimal and executed quickly. Thus it is essential that manuscripts are accurate when submitted. Authors can track the status of their accepted articles on <http://cn.sv-jme.eu>.

PUBLICATION FEE:

Authors will be asked to pay a publication fee for each article prior to the article appearing in the journal. However, this fee only needs to be paid after the article has been accepted for publishing. The fee is 240.00 EUR (for articles with maximum of 6 pages), 300.00 EUR (for articles with maximum of 10 pages), plus 30.00 EUR for each additional page. The additional cost for a color page is 90.00 EUR. These fees do not include tax.

Strojniški vestnik - Journal of Mechanical Engineering
Aškerčeva 6, 1000 Ljubljana, Slovenia,
e-mail: info@sv-jme.eu



<http://www.sv-jme.eu>

Contents

Papers

- 685 Tomaž Finkšt, Jurij Franc Tasič, Marjeta Zorman Terčelj, Marko Meža:
A Classification of Malignancy in Suspicious Lesions Using Autofluorescence Bronchoscopy
- 696 Vytautas Ostaševičius, Vytautas Jūrėnas, Andrius Vilkauskas, Gytautas Balevičius, Andrius Senkus, Eglė Jotautienė:
A Novel Excitation Approach to Ultrasonically-Assisted Cylindrical Grinding
- 705 Damian Janicki:
Fabrication of High Chromium White Iron Surface Layers on Ductile Cast Iron Substrate by Laser Surface Alloying
- 715 Jiangping Mei, Jiawei Zang, Yabin Ding, Shenglong Xie, Xu Zhang:
Rapid and Automatic Zero-Offset Calibration of a 2-DOF Parallel Robot Based on a New Measuring Mechanism
- 725 Marko Švaco, Bojan Šekoranja, Filip Šuligoj, Josip Vidaković, Bojan Jerbić, Darko Chudy:
A Novel Robotic Neuronavigation System: RONNA G3
- 736 Ningning Wang, Xueyi Li, Kun Wang, Qingliang Zeng, Xiao Shen:
A Novel Axial Modification and Simulation Analysis of Involute Spur Gear
- 746 Metod Čuk, Franc Kosel, Nenad Zrnić, Boris Jerman:
Analysis of Continuous Sandwich Panels with Profiled Faces